Report Date: October 1, 2003

Semi-Annual Technical Progress Report

INVESTIGATION OF EFFICIENCY IMPROVEMENTS DURING CO_2 INJECTION IN HYDRAULICALLY AND NATURALLY FRACTURED RESERVOIRS

DOE Contract No.: DE-FC26-01BC15361

Harold Vance Department of Petroleum Engineering
Texas A& M University
3116 TAMU
College Station, TX 77843-3116
(979) 845-2241

Contract Date:	September 28, 2001
Anticipated Completion Date:	September 27, 2004

Principal Investigator:	David S. Schechter Harold Vance Department of Petroleum Engineering
Contracting Officer's Representative:	Dan Ferguson National Petroleum Technology Office
Report Period:	April 1, 2003- October 1, 2003

US/DOE Patent Clearance is not required prior to the publication of this document.

DISCLAIMER

This report was prepared as an account of work sponsored by an agency of the United States Government. Neither the United States Government nor any agency thereof, nor any their employees, makes any warranty, express or implied, or assumes any legal liability or responsibility for the accuracy, completeness, or usefulness of any information, apparatus, product, or process disclosed, or represents that its use would not infringe privately owned rights. Reference herein to any specific commercial product, process, or service by trade name, trademark, manufacturer, or otherwise does not necessarily constitute or imply its endorsement, recommendation, or favoring by the United States Government or any agency thereof. The views and opinions of authors expressed herein do not necessarily state or reflect those of the United States Government or any agency thereof.

ABSTRACT

This report describes the work performed during the second year of the project, "Investigating of Efficiency Improvements during CO_2 Injection in Hydraulically and Naturally Fractured Reservoirs." The objective of this project is to perform unique laboratory experiments with artificial fractured cores (AFCs) and X-ray CT to examine the physical mechanisms of bypassing in HFR and NFR that eventually result in less efficient CO_2 flooding in heterogeneous or fracture-dominated reservoirs. To achieve this objective, in this period we concentrated our effort on modeling the fluid flow in fracture surface, examining the fluid transfer mechanisms and describing the fracture aperture distribution under different overburden pressure using X-ray CT scanner.

Modeling Fluid Flow through a Single Fracture using Experimental, Stochastic, and Simulation Approaches

In this report, sensitivity of fracture modeling, error involved in the experiments and saturation match of fracture imbibition experiments using X-ray CT Scanner are established.

A fracture is usually assumed as a set of smooth parallel plates separated by a constant width. However, the flow characteristics of an actual fracture surface are quite different, affected by tortuosity and the impact of surface roughness. Though several researchers have discussed the effect of friction on flow reduction, their efforts lack corroboration from experimental data and have not converged to form a unified methodology for studying flow on a rough fracture surface. The goal of this research is to examine the effect of surface roughness for flow through fractures and to effectively incorporate them into simulations with the aid of geostatistics.

In this study, we have shown an integrated methodology, involving experiments, stochastics and numerical simulations that incorporate the fracture roughness and the friction factor, to describe flow on a rough fracture surface. Laboratory experiments were performed to support the study in quantifying the flow contributions from the matrix and the fracture under varying confining pressures. The results were used to modify the cubic law through reservoir simulations. Observations suggest that the fracture apertures need to be distributed to accurately model the experimental results.

The methodology successfully modeled fractured core experiments, which were earlier not possible through parallel plate approach. A gravity drainage experiment using an X-ray CT scan of a fractured core has also validated the methodology.

Simulation of Naturally Fractured Reservoirs using Empirical Derived Transfer Function

This research utilizes the imbibition experiments and X-Ray Tomography results for modeling fluid flow in naturally fractured reservoirs. Conventional dual porosity simulation requires large number of runs to quantify transfer function parameters for history matching purposes. In this study empirical transfer functions (ETF) are derived from imbibition experiments and this allows reduction in the uncertainty in modeling of transfer of fluids from the matrix to the fracture.

The application of ETF approach is applied in two phases. In the first phase, imbibition experiments are numerically solved using the diffusivity equation with different boundary

conditions. Usually only the oil recovery in imbibition experiments is matched, however, with the advent of X-Ray CT the spatial variation of the saturation can also be computed. The matching of this variation can lead to accurate reservoir characterization. In the second phase, the imbibition derived empirical transfer functions are used in developing a dual porosity reservoir simulator. The results from this study are compared with published results. The study reveals the impact of uncertainty in the transfer function parameters on the flow performance and reduces the computations to obtain transfer function required for dual porosity simulation.

Fracture Aperture Calibration

This study addresses the use of an X-Ray CT scanner to image fracture aperture distribution. By applying variable overburden on fractured media, the change in fracture aperture has been observed. The general distribution of fracture apertures is quite heterogeneous. In the past, lognormal function has been used to describe fracture aperture distribution. This study shows how to generate the fracture aperture calibration that be used later on to describe and confirm aperture distribution under different overburden conditions.

Fracture Aperture Distribution

The fracture aperture and fracture permeability are usually considered to remain the same during the producing life of a naturally fractured reservoir, regardless of degree of depletion, but reservoirs experience different stress state conditions, therefore understanding the fracture behavior becomes more complex.

This research analyzes the effect of fracture aperture and fracture permeability on the fluid flow under different overburden pressure. This paper investigates the fracture apertures under different stress-state conditions. The equations to quantify the flow through the matrix and the fracture at different overburden pressures are provided. The X-ray CT scanner was used to obtain fracture aperture distributions at various overburden pressures to verify the applicability of lognormal distribution, for fracture aperture. This has been commonly used for distributing fracture apertures in the past but never verified experimentally. In addition, reservoir simulations are performed to duplicate the experimental results and to provide a valid model for future stress-sensitive reservoirs.

Our experimental results show that the fracture aperture and fracture permeability have significant pressure-dependent changes in response to applying variable injection rates and overburden pressures. The laboratory results show that the change in overburden pressure significantly affects the reservoir properties. The change in matrix permeability with different injection rates under variable overburden pressures is not significant in contrast with that effect on fracture aperture and fracture permeability. Calibration curve was obtained to determine fracture aperture from the X-ray CT scanner results. This experimental research will increase the understanding of fluid flow behavior in fractured reservoirs.

TABLE OF CONTENTS

DISCLAIMER ii
ABSTRACT iii
TABLE OF CONTENTS v
LIST OF TABLES vii
LIST OF FIGURES viii
ACKNOWLEDGMENTS xii
EXECUTIVE SUMMARY xiii
I. X-Ray Tomography Results Validate Numerical Modeling of Flow in Fractures 1
1.1 Introduction 1
1.2 Error analysis 2
1.3 X-ray CT scanner results 3
1.4 Simulation of X-ray CT scanner experiments 3
1.5 Sensitivity studies 4
1.5.1 Effect of variance of aperture distribution on fracture flow rate 4
1.5.2 Determination of critical aperture size 5
1.5.3 Effect of matrix permeability 5
1.5.4 Effect of matrix heterogeneity 6
1.5.5 Simulator testing 7
1.6 Conclusions and future work 8
1.7 References 24
II. Simulation of Naturally Fractured Reservoirs Using Empirically Derived Transfer Function 25
2.1 Introduction 25
2.2 Literature Review and Present Status 26
2.3 Transfer Functions 29
2.3.1 Empirical Transfer Functions 29
2.3.2 Scaling Transfer Functions 31
2.3.3 Transfer Function Using Darcy Law 33
2.3.4 Diffusivity Transfer Functions 34
2.3.5 Comparison of the Transfer Functions 34

2.3.6 Flow Visualization using X-Ray Tomography 35
2.4 Methodology-Procedure of Study 35
2.4.1 Simulator to Model the Imbibition Experiments 35
2.4.2 Dual Porosity Simulator 36
2.4.2.1 Fracture Flow Equations. 36
2.4.2.2 Matrix Flow Equations 39
2.4.2.3 Empirical Transfer Function 40
2.4.2.4 Discretization of the Equations 41
2.5 Discussions 49
2.6 Conclusions 52
2.7 References 53
III. Fracture Aperture Calibration 71
3.1 Introduction 71
3.2 Experimental Procedure 72
3.3 Results and Discussions 73
3.4 Conclusions 74
3.5 References 79
IV. Fracture Aperture Distribution 81
4.1 Introduction 81
4.2 Methodology 84
4.2.1 Experimental Procedure 84
4.2.2 Image Transfer 84
4.2.3 Data Preparation 84
4.2.4 Data Distribution 84
4.3 Discussion 85
4.4 Conclusions 86
4.5 References 98

APPENDIX-A 100

LIST OF TABLES

Table 1.1—Experimental error analysis 10
Table 1.2—Fracture properties obtained from pressure drop match 10
Table 1.3—Comparison of fracture properties from simulation and experimental results 10
Table 2.1—Shape Factors as reported by Penula-Pineda 58
Table 2.2—Modeled Garg et al core properties.....58
Table 2.3—Parameters for match of imbibition response (Garg et al).....59
Table 2.4—Properties of the core for numerical simulation (Vivek et al) 59
Table 2.5—Capillary pressure obtained from the match. 60
Table 2.6—Relative permeability obtained for the match. 60
Table 4.1—Dataset showing range and frequency for various overburden pressure conditions. 87
Table 4.2—Statistical Parameters for different overburden conditions.....87

LIST OF FIGURES

Figure 1.1 — Water saturation change in matrix and fracture at transient flow condition. 11
Figure 1.2 — Simulation results of flow rates and pressure drop injected at 5 cc/min and overburden pressure of 500 psi. 11
Figure 1.3 — Average flow rate comparison between laboratory and simulation results at 5 cc/min and each different overburden pressure. 12
Figure 1.4 — Average pressure drop comparison between laboratory and simulation results at 5 cc/min and each different overburden pressure. 12
Figure 1.5 — Average pressure drop match between observed and simulation results for the fractured core experiment for 5 cc/min injection rate. 13
Figure 1.6 — Average flow rates observed for the corresponding average pressure drop match across the core at 5 cc/min injection rate 13
Figure 1.7 — X-ray CT scans (perpendicular to the fracture) of single-phase gravity drainage experiment through a fractured core 14
Figure 1.8 — Fluid movement through a core with smooth fracture 15
Figure 1.9 — Fluid front movement through a core with distributed fracture surface. 16
Figure 1.10 — Average water saturation match between simulation and X-ray CT scan. 17
Figure 1.11 — Log-normal distribution for constant aperture width at different variances. 17
Figure 1.12 — Comparative plots of hydraulic aperture reduction as a result of increased roughness (variance). 18
Figure 1.13 — Log-normal distribution for constant variance at different aperture widths. 18
Figure 1.14 — Comparison between parallel plate (smooth) and distributed aperture flow (rough) for different apertures. 19
Figure 1.15 — Effect of matrix permeability on pressure drop across the core. 19
Figure 1.16 — Effect of matrix permeability on fracture flow rate. 20
Figure 1.17 — Comparison of fracture flow rates between smooth and rough fractures for different matrix permeabilities. 20
Figure 1.18 — Difference in pressure drop across the core between smooth and rough fractures at different matrix permeabilities. 21
Figure 1.19 — Distribution of matrix permeability layer (case 2). 21

Figure 1.20 — Distribution of fracture permeability layer (cases 1 and 2). 22
Figure 1.21 — One-dimensional model employed in simulation testing.....22
Figure 1.22 — Comparative plot of pressure drops observed from simulation and through Darcy's law. 23
Figure 2.1 — (a) Actual Reservoir (b) Idealized Reservoir. 61
Figure 2.2 — Conservation of mass in a control volume.....61
Figure 2.3 — Flow Chart for Newton-Raphson's method of solution.....62
Figure 2.4 — Effect of Gravity on Imbibition Response 63
Figure 2.5 — Gravity and capillary forces as a function of time during imbibition.....63
Figure 2.6 — Effect of Relative Permeability exponent on Imbibition Recovery.....64
Figure 2.7 — Effect of end point capillary pressure on imbibition response. 64
Figure 2.8 — Match of experimental recovery with simulated recovery. 65
Figure 2.9 — Match of experimental and simulated saturations. 65
Figure 2.10 — Match of experimental and simulated recovery.....66
Figure 2.11 — One dimensional low production rate pressure and water saturation profiles. 66
Figure 2.12 — One-dimensional, high production, pressure and water saturation profiles.....67
Figure 2.13 — Pressure Profile along a line parallel to Y-axis.....67
Figure 2.14 — Pressure profile along a line parallel to X-axis.....68
Figure 2.15 — Material Balance error for the empirical model, two dimensional case. 68
Figure 2.16 — Empirical transfer function as a function of time 69
Figure 2.17 — Imbibition Simulator Response.....69
Figure 2.18 — Representation of the matrix block surrounded by water. 70
Figure 2.19 — Comparison of Empirical transfer function with sub-domain method and dual porosity methods. 70
Figure 3.1 — CAT scan for 51 microns fracture size and corresponding CT number plot. 75
Figure 3.2 — CAT scan for 64 microns fracture size and corresponding CT number plot. 75
Figure 3.3 — CAT scan for 76 microns fracture size and corresponding CT number plot. 76
Figure 3.4 — CAT scan for 127 microns fracture size and corresponding CT number plot. 76
Figure 3.5 — Average CT number plot. 77

Figure 3.6 — Plot with shaded area representing fracture. 77
Figure 3.7 — Integrated CT signal determination. 78
Figure 3.8 — CT number decreases with increase in fracture size. 78
Figure 3.9 — Final calibration curve obtained after area integration. 79
Figure 4.1 — Berea core with fractured in the central plane. 88
Figure 4.2 — Distribution of CT number along the row showing a dip for the fracture. 88
Figure 4.3 — Distribution of CT number along the column showing the heterogeneity.....88
Figure 4.4 — Sample scans taken along the length of the core without overburden pressure. 89
Figure 4.5 — Sample scans taken along the length of the core with 500 psi overburden pressure. 90
Figure 4.6 — Sample scans taken along the length of the core with 1000 psi overburden pressure. 91
Figure 4.7 — Sample scans taken along the length of the core with 1500 psi overburden pressure. 92
Figure 4.8 — Probability distribution of fracture apertures without overburden pressure. 93
Figure 4.9 — Probability distribution of fracture apertures at 500 psi overburden pressure. 93
Figure 4.10 — Probability distribution of fracture apertures at 1000 psi overburden pressure. 94
Figure 4.11 — Probability distribution of fracture apertures at 1500 psi overburden pressure. 94
Figure 4.12 — Comparative study of fracture aperture distribution under various overburden pressures. 95
Figure 4.13 — Comparison of Observed and Lognormal distribution of fracture apertures without overburden pressure. 95
Figure 4.14 — Comparison of Observed and Lognormal distributions of fracture apertures at 500 psi overburden pressure. 96
Figure 4.15 — Comparison of Observed and Lognormal distributions of fracture apertures at 1000 psi overburden pressure. 96
Figure 4.16 — Comparison of Observed and Lognormal distributions of fracture

apertures at 1500 psi overburden pressure. 97
Figure 4.17 — Comparison of Lognormal distributions at different overburden pressures. 97

ACKNOWLEDGMENTS

Financial support for this work is provided by the United States Department of Energy (NPTO/National Petroleum Technology Office). This support is gratefully acknowledged.
Our thanks to CMG, which donated software used in reservoir modeling. I greatly appreciate diligent efforts from the following individuals who contributed to this project: Erwinsyah Putra helped with the technical part of this research, Dicman Alfred conducted the modeling and experimental work with help from Vivek Muralidharan and is described in Chapter 1, Prasanna K Tellapaneni conducted the modeling of fluid transfer mechanisms described in Chapter 2, Vivek Muralidharan and Deepak Chakravarthy performed the experimental work on the X-Ray CT scanner described in Chapters 3 and 4, respectively.

EXECUTIVE SUMMARY

This report describes the work performed during the second year of the project, "Investigating of Efficiency Improvements during CO_2 Injection in Hydraulically and Naturally Fractured Reservoirs." The objective of this project is to perform unique laboratory experiments with artificial fractured cores (AFCs) and X-ray CT to examine the physical mechanisms of bypassing in HFR and NFR that eventually result in less efficient CO_2 flooding in heterogeneous or fracture-dominated reservoirs.

This report provides results of the fourth semi-annual technical progress report that consists of modeling fluid flow through a single fracture using experimental, stochastic, and simulation approaches; simulation of naturally fractured reservoirs using empirical derived transfer function; fracture aperture calibration; and fracture aperture distribution. Within the project objective, the specific goals for this period are to (1) establish the fundamental mechanisms of transfer in fracture systems, (2) examine the effect of surface roughness for flow through fractures, and (3) determine the fracture distribution under different overburden pressures.

We are on the verge of an important step in the global understanding of the connection between fracture characterization and fundamentals of fluid flow in fractured systems. The combination of X-Ray CT scanning and basic fluid flow experiments in tandem with numerical simulation has allowed us to take the first steps in making the connection between field observations, simulation and small-scale experiments commonly performed in laboratories. The applications of this research are wide ranging and include the use of X-Ray CT scanning, open hole logs, well test analysis and simulation in order to input realistic fracture networks into reservoir simulators. The profound impact this research has on future engineering applications in naturally and hydraulically fractured reservoirs is immense. Until now, there has been a large disconnect between field performance, interpretation of data collected to characterize fracture networks and the techniques used to simulate and predict fluid flow in fractured systems. We believe this research will eventually provide basic tools that will allow the long-missing connection between laboratory work and theory and actual field performance.

In this report we present the following work that has been performed to achieve the aforementioned goals. We are researching basic fluid flow in single, rough fractures and investigating differing levels of stress on fluid flow behavior in the fracture. We have become adept at performing numerical simulations on this type of experiment and closely matching the observed results. An important point is we are no longer relying simply on pressure matches but also saturation distributions in the rock as determined by X-Ray CT scanning and matched with reservoir simulators. This important advancement has provided a plethora of methodologies that will eventually provide the connection between the abundant theoretical work and the numerous observations of fluid flow in naturally and hydraulically fractured reservoirs. The following headings and subsequent findings outline the work that appears in this report.

Modeling Fluid Flow through a Single Fracture using Experimental, Stochastic, and Simulation Approaches

In previous work, we have shown an integrated methodology, involving experiments, stochastics and numerical simulations that incorporate the fracture roughness and the friction factor, to describe flow on a rough fracture surface. Important conclusions can be drawn from the work include:

1. The fracture aperture needs to be distributed to accurately model the experimental results.
2. The effect of friction factor due to surface roughness should be considered in modeling flow on a rough fracture surface.
3. There is an increased flow through fractures when the variance of the aperture distribution is increased. This reiterates the fact that tortuosity in fluid flow is a significant factor.

In this report, sensitivity of fracture modeling, error involved in the experiments and saturation match of fracture imbibition experiment using X-ray CT Scanner are established.

Important findings from this study - X-ray CT scan reveal that the parallel plate assumption in modeling fluid flow in fracture media seldom reflects the nature of flow through fractures. The effective hydraulic aperture is reduced with increased variance of the aperture distribution. Beyond an aperture size of approximately 60 microns, the effect of roughness or tortuosity is found to be insignificant. The sensitivity studies on matrix permeability show that the fracture has to be modeled with a two dimensional aperture distribution regardless of the value of matrix permeability. Even though the flow rates may appear to be the same, the pressure drop across the core is different. Matrix heterogeneity in cores with high permeability does not affect the flow rate through fracture significantly

Simulation of Naturally Fractured Reservoirs using Empirical Derived Transfer Function

In previous work, we have shown that we are able to model the spontaneous imbibition experiment utilizing the X-Ray CT scan results. We continue our effort by including the imbibition modeling into dual porosity simulation by changing the fluid transfer term. A detail explanation about different transfer functions and derivation of mathematical modeling till developing dual porosity simulator using empirical derived transfer function are presented in this report.

Important findings from this study - Diffusivity equation is sufficient to model imbibition experiments. Imbibition experiments provide us with empirical transfer functions that can be used to model dual porosity simulation. Empirical dual porosity simulation is inherently faster because the number of unknowns per grid block is reduced to two from four. “Material Balance” is not conserved to the extent of conventional dual porosity formulations.

Fracture Aperture Calibration

This study addresses the use of an X-Ray CT scanner to image fracture aperture distribution. And shows how to generate the fracture aperture calibration that be used later on to describe aperture distribution under different overburden conditions.
Important findings from this study - The calibration curve shows a linear trend even at very small apertures.

Fracture Aperture Distribution

In previous work, we have performed experimental work to describe the effect of different stresses on rock properties. Important conclusions can be drawn from the work include:

1. The laboratory result shows that the change in overburden pressure significantly affects the fracture permeability and fracture aperture.
2. The results also infer that the effect of stresses may be most pronounced in fractured reservoirs where large pressure changes can cause significant changes in fracture aperture and related changes in fractured permeability.
3. The change in porosity with different overburden pressure has shown to be small compared to significant effect on permeability.
4. At high overburden pressure the influence of existing fracture permeability on fluid flow contributor in permeable rocks (> 200 md) is not too significant.
5. The reduction of effective permeability due to fractures with applied stress is greater than that of the unfractured core. The fracture aperture and fracture permeability decreases with an increase in the applied stress.
6. Fracture flow dominates when the applied stress is less; however, the matrix flow rate increases as applied stress increases and dominates at high stress even if the fracture does not heal completely.
7. The hydrostatic stress has the greatest impact on reduction the matrix and fracture permeabilities and fracture aperture followed by the triaxial and uniaxial stresses.

This research uses X-ray CT scanner to image the fracture aperture under various overburden pressures and using a calibration curve, measures the fracture aperture at various points along the length of the core, thus generates sufficient data for characterizing the distributions of fracture apertures.
Our experimental results show that parallel plate approach of the fractures is no longer valid when the fracture aperture is small due to significant applied overburden pressure. The result of this study confirms the previous studies that fracture aperture distribution is lognormal distribution without overburden pressure. Upon applied overburden pressure, the distribution still follows the common lognormal distribution.
Important findings from this study - Parallel plate approach of the fractures is no longer valid when the fracture aperture is small due to significant applied overburden pressure. The result of this study confirms the previous studies that fracture aperture distribution is lognormal distribution at no overburden pressure. Upon applied overburden pressure, the distribution still follows the common lognormal distribution.

Project Fact Sheet
Progress work efforts at Project Fact Sheet are listed in Appendix A.

I. MODELING FLUID FLOW THROUGH A SINGLE FRACTURE USING EXPERIMENTAL, STOCHASTIC, AND SIMULATION APPROACHES

1.1 Introduction

Earlier it was shown that fracture modeling using a parallel plate approach proved inadequate to reproduce the experimental observations.[1] In this chapter, sensitivity of fracture modeling, error involved in the experiments and saturation match of fracture imbibition experiments using an X-ray CT scanner are established.

To recount the modeling procedure for the experiments in which flow experiments were conducted through a fracture created artificially at the center of a core, a numerical model which utilized a commercial simulator (CMG™) was used to study the fluid flow through fractures at different overburden pressures. The laboratory process in which the water was injected through the fracture was duplicated in this modeling effort. Rectangular grid blocks were used to overcome the difficulty of modeling a cylindrical core shape.[2,3] 31x31 grid blocks were used in the x and z directions with 1 grid block in the y direction. The fracture layer is located only in the 16th layer and the rest are matrix layers. The permeability in the fracture layer was calculated based on two parallel plates without fracture roughness. All the layers were injected with constant water injection of 5 cc/hr. At the opposite end, two production points were located in the matrix and fracture layers to quantify the amount of water produced at those two points.

In the experimental process, the core is saturated with the water. Once water injection was initiated with a constant rate, water was produced simultaneously. Then the water that was produced from both matrix and fracture layers at the end point was recorded. In the simulation, however, the initial water saturation condition is assumed zero to visualize the movement of water through a single fracture. The water saturation change in the matrix and fracture during transient state can be observed as illustrated in Fig. 1.1.

A few minutes after the injection was started, the flow rate was still in the transient condition and then reached a steady state condition at later time as shown in Fig. 1.2. At steady state, the amount of water produced from matrix and the fracture was recorded. Similar simulation runs were performed for different overburden pressures.

1.2 Error analysis

Any experimental data is subject to errors. So an error analysis was performed using the experimental data to quantify the range of error in the calculation of matrix and fracture flow rates. The summary of the error analysis for the injection rate case of 5 cc/min is presented in Table 1.1. The parameter fracture flow rate (Q_f) in Table 1.1 was calculated by subtracting the matrix flow rate from the total injection rate. From the table we find that the errors involved in the calculation of fracture flow rates are relatively small (< 8%), at lower overburden pressures (500 and 1000 psia) when compared to the high overburden pressure case (1500 psia). This indicates that the values obtained at high overburden pressure have a large degree of uncertainty.

This could be due to the fact that at high overburden pressures, the characteristics of the matrix have a dominant influence on fracture flow. Due to time constraints, the high levels of uncertainty at higher overburden pressures have not been explored or taken into account while modeling. This is an area where more analysis could be done in the future.

The results for the 5 cc/min injection case were compared with the experimental results as shown in Figs. 1.3 and 1.4. The dotted lines indicate the experimental results.

Even though the quality of the match for both flow rate and pressure drop are not very good due to using a single fracture model, which assumed a smooth fracture surface between two parallel plates, the simulation results follow the trend of the laboratory results.

To make sure that resulting discrepancies in flow rates did not arise due to assumption or the error involved in the experimental measurement, modeling was done to match the experimental observation, namely the pressure drop across the core. Figures 1.5 and 1.6 show the matching between experimental and simulated results for average pressure drop across the core and flow rates, respectively. The aperture widths and their corresponding permeabilities with overburden pressures for the pressure drop match are given in Table 1.2. From the resulting average fracture flow rates, the effective aperture width was back-calculated from cubic law. The results of the effective aperture width calculated from fracture flow rates and the comparison to the effective aperture widths inferred from experiments is given in Table 1.3. The results reveal that the effective

fracture aperture widths obtained by matching the average pressure drop (actual measured parameter in the experiments) is outside the range of effective aperture widths inferred from experiments. So the deviations from the cubic law did not arise due to the assumption or the error involved but could be due to the rough nature of the fracture surface. Even if we assume that the deviation in flow rates was due to the error involved, a simultaneous match for the average pressure drop and the average flow rates could not be achieved.

1.3 X-ray CT scanner results

In an attempt to study the movement of brine in a fractured core, a simple experiment was carried out using an X-ray CT scanner. The experimental procedure involved injecting water at a rate of 0.5 cc/min from the top-center of the core. The injection was done through the fracture. The movement of brine on a cross section perpendicular to the fracture observed through the CT-Scan is presented in Fig. 1.7.

The experiment was modeled using a commercial simulator. The fracture was modeled as smooth plates hence having a constant permeability layer. Since the aperture value could not established through the scan pictures due to the resolution, an aperture value of 50 microns was assumed. From the observations, it was found that smooth fracture assumption failed to recreate the saturation-front movement seen through CT-scans (Fig 1.8). The fluid moved through the fracture quickly because of its high permeability. Hence for modeling purposes a parallel plate approach for fractures fails to portray the true nature of flow. The flow on a smooth fracture surface is found to be different than flow on a rough fracture surface. As could be observed from scans and modeling results, the shape of sweep occurring in a plane perpendicular to the fracture is not adequately described by parallel plate modeling. Hence there is a need to model fractures quite different from what has been done in the past.

1.4 Simulation of X-ray CT scanner experiments

Once it was concluded that smooth fracture modeling could not replicate the movement and the average saturation calculated from CT-scans, modeling was carried out using the integrated methodology. This time the fracture apertures were distributed

and roughness accounted for through a friction factor. Figure 1.9 illustrates the result of this kind of modeling.

The distributed fracture modeling also adequately matched the average water saturation inferred from X-ray CT-scans (Fig.1.10). The parallel plate model neither reproduced the movement of the water front nor matched the average water saturation obtained from the CT scans. As a result of this match, fracture aperture was estimated to be around 120 microns and the aperture distribution had a variance of 260 micron^2.

1.5 Sensitivity studies

1.5.1 Effect of variance of aperture distribution on fracture flow rate

For sensitivity studies a core model with 31x15 grid block size was used in the x and y directions with 15 layers in the z direction. The fracture layer was incorporated in the 8th layer and the rest are matrix layers. The modified permeability layer was used for the fracture layer, while the matrix layers had a constant permeability. All the layers were subjected to constant rate water injection of 5 cc/min through injection points located at one extreme end and penetrating through all the layers. At the opposite end two production points were located, one for the matrix layers and the other for the fracture layer to quantify the amount of water produced at those two points. For this study, a single phase was used.

Initially, with a constant mean aperture size of 56.4 μm, the fracture aperture distribution was generated solely through a lognormal distribution. Aperture distributions were obtained for different variances (100, 200, 600, 1000 (micron^2)). From the simulation results, it was found that the increased variance in the fracture aperture distribution leads to a reduction in the mean hydraulic aperture size. The hydraulic aperture is the value of the aperture required to produce the observed pressure drop across the core. This observation can be explained from previous observations by Dagan[4] , who approximated the change in effective hydraulic aperture as a result of roughness through,

$$h_{eff}^{\ 3} \approx h_{hyd}^{\ 3}(1-1.5\,\sigma_h^{\ 2}/\langle h_{hyd}\rangle^2) \qquad (1)$$

where, h_{eff} is the effective hydraulic aperture as a result of roughness (microns) and σ_h^2 is the variance of hydraulic aperture (microns)^2 and $\langle h_{hyd}\rangle$ is the mean hydraulic aperture.

In our simulation, experiments show the same trend as observed by Dagan. Figure 1.11 illustrates the lognormal realizations of aperture distributions with constant width and different variances while Figure 1.12 shows the comparative plots between simulated and Dagan's approximation of hydraulic aperture reduction as a result of increased roughness (variance).

1.5.2 Determination of critical aperture size

In order to establish the limitation or restriction of this approach simulation runs were performed maintaining a constant variance and different aperture widths. Figure 1.13 illustrates the log-normal realizations of constant aperture variance but different aperture widths In other words, the aim of this sensitivity study was to determine the critical aperture width beyond which rough fracture surfaces could be treated as a smooth parallel plates. Figure 1.14 compares flow rates from fracture between the simulation runs of distributed fracture apertures, accounting for roughness and parallel plate assumptions. In parallel plate assumptions, the fracture layer was assumed to be uniform rather than being distributed log-normally. Hence it had a constant permeability throughout. From the Figure it is seen that as the aperture size increases the effect of rough surfaces also gradually decreases. From the observations it is inferred that beyond an aperture size approximately 60 microns, the effects of roughness or tortuosity is found to be insignificant. This is rooted in the fact that larger aperture size means lower overburden pressure. So it could be inferred that as over burden pressure increases, the effect of roughness becomes more predominant.

1.5.3 Effect of matrix permeability

The permeability of the Berea core used in the experiments is about 300 md. Usually in fractured reservoirs the matrix permeability varies in the range of 1 to 10 md. A sensitivity study was conducted to determine if matrix permeability had any impact in determining flow rates through fractures. Simulation runs were performed varying the permeability range from 0.001 to 1000 md. The size of the fracture aperture was 40 microns and the variance of the aperture distribution was 200. The injection rate of water was 5 cc/min. From the results, it was inferred that only if the matrix permeability

increased to beyond 1000 md, was the pressure drop across the core reduced considerably. When considering a moderate permeability matrix (k = 1 md) embedded with high fracture permeability (k ≈ 135000 md in this case), there is a significant pressure drop across the core. This pressure drop reduces significantly only when the matrix permeability increases beyond 1000 md. Figure 1.15 illustrates this phenomenon. The fracture flow much as would be expected, following the same trend (Fig 1.16).

Sensitivity studies were also conducted to observe the impact of matrix permeability between rough fracture surfaces and smooth parallel plates. Figure 1.17 compares the fracture flow rates between smooth and rough fractures for different matrix permeabilities.

Although the impact on fracture flow rates were insignificant, the effect on pressure drop was quite significant. For a range of matrix permeability between 0.001 md and 10 md, the difference in the pressure drop between rough fracture surfaces and smooth parallel plates varied from 7 to 6.2 psia. Thus distributing the fracture apertures mainly affects the pressure distribution in the core. Figure 1.18 illustrates the difference in pressure drop across the core between rough fracture and smooth fractures. The difference is almost negligible at a matrix permeability of 1000 md, however, in reality we seldom find a naturally fractured reservoir with high matrix permeability like that.

1.5.4 Effect of matrix heterogeneity

In the core experiments a Berea core was used. A Berea core is known to be fairly homogeneous with high matrix permeability. The true effect of matrix heterogeneity can only be established after having studied the core with an X-ray CT scanner. The porosity distribution of the core can be established through CT scans. But for permeability distribution some kind of empirical correlation has to be used, since matrix permeability heterogeneity cannot be established through CT scans. In this research an attempt was made to study the effect of matrix heterogeneity on flow through the fractures. Two cases were run to study the effect. The first case had a single value for matrix permeability (100 md) and in the second case the matrix permeabilities were distributed randomly in the range of 80 to 130 md. In both the cases the fracture permeability layer was distributed through the lognormal distribution (mean aperture = 60 microns and variance = 500

micron [2]). Figures 1.19 and 1.20 show the distribution of permeabilities used in the matrix (case 2) and the fracture layer respectively.

The total area of the matrix in this study was 5 cm * 5 cm * 5 cm. The simulation grid size used was 15*15*15. The fracture layer was introduced in the 8th layer in the z-direction. An injection rate of 5 cc/min was applied at one end and was produced at the other end. The fracture flow rates obtained from both the cases were 3.76 cc/min (case 1) and 3.82 cc/min (case 2). The difference in the flow rates was 0.04 cc/min, which is about a 1% change from the case of constant matrix permeability. Therefore, matrix heterogeneity of a core with high matrix permeability (100 md in this case) does not play a significant role in affecting flow contributions through a fracture.

1.5.5 Simulator testing

Sensitivity studies were also performed to test whether the simulator provides accurate results when confronted with a very high permeability region (fracture) among surrounding matrix blocks (low permeability regions). A one-dimensional model was established in which serial flow was modeled across blocks of moderate permeability (10 md) with a high permeability block embedded in the center. The values for high permeability were varied from 100 md to 10000000 md. An example of the model is shown in Fig. 1.21, where the value of the high permeability region is 10000 md. The model was injected from one end and produced at the other end. The injection rate used in this case was 5 cc/min. The producer was operated at atmospheric pressure. The pressure drops obtained from simulations were compared with those obtained from Darcy's law. The pressure drop across the core is obtained from Darcy's law, however:

$$\Delta p = \frac{Q * \mu * l}{\bar{k} A} \qquad (2)$$

where Q is the matrix flow rate (cc/sec), $\bar{k}$ is the average matrix permeability (Darcy), A is the matrix area (cm^2), Δp is pressure drop across the core (atm), μ is viscosity (cp) and L is core length (cm).

The average permeability $\bar{k}$ for this model can be obtained through [1],

$$\bar{k} = \frac{L}{\sum \frac{l_i}{k_i}} \tag{3}$$

where L is the total length of the core, l_i is the length of the grid block (x-dir) and k_i is the corresponding grid block permeability.

The results of simulation testing are given in Fig. 1.22. The pressure drops obtained from simulation are compared with those obtained from Darcy's law. The comparison shows the values obtained from simulation are consistent with Darcy's law. The maximum deviation was about 0.25 psi, which is less than 1% of the actual value. Accurate results can be obtained from increased griding.

1.6 Conclusions and future work

Even though much work still remains to procure all the necessary analysis and data to provide a detailed modeling procedure for flow through single fractures, the proposed methodology is able to model flow experiments through single fractures fairly well. So far, the following conclusions can be drawn based on the work:

1. Quantification of effective aperture widths is possible through proper experiment design.
2. The effect of friction due to surface roughness needs to be taken into account while modeling. In these experiments friction reduced the flow through the fractures by approximately 24%. In addition to the reduction of flow, the pressure drop observed across the core is quite different from the one that would result due to smooth parallel plate modeling.
3. The effective hydraulic aperture is reduced with increased variance of the aperture distribution.
4. Beyond an aperture size of approximately 60 microns, the effects of roughness and tortuosity are found to be insignificant.
5. The sensitivity studies on matrix permeability show that the fracture has to be modeled with a two dimensional aperture distribution regardless of the value of matrix permeability. Even though the flow rates may appear to be the same, the pressure drop across the core is different.

6. Matrix heterogeneity in cores with high permeability does not affect the flow rate through fracture significantly.
7. The simulator is found to give consistent results when a very high permeability region is embedded among moderate permeability blocks.
8. The simulation results suggest that a parallel plate model is insufficient to predict fluid flow in the fracture system. Consequently, the spatial heterogeneity in the fracture aperture must be included in the modeling of fluid flow through fracture system.
9. The results also infer that the effect of stresses may be most pronounced in fractured reservoirs where large pressure changes can cause significant changes in fracture aperture and related changes in fracture permeability.
10. At high overburden pressures the influence of existing fracture permeability is not too significant. This conclusion is limited to the Berea core, which has high matrix permeability.
11. X-ray CT scans reveal that parallel-plate modeling of fractures seldom reflect the true nature of flow through fractures.
12. Though it is shown that effective aperture successfully modeled experimental results using the integrated methodology, the value of the fracture aperture is only a close estimate. The correct value of the fracture aperture can be obtained with high accuracy using an X-Ray CT Scan.

Modeling flow through fractures is an area of active research. The methodology described in this work could open more perspectives in fracture modeling. Improvements could be made to this model by distributing porosity in the core scale and also considering the effect of matrix heterogeneity. Our next step would be to apply this methodology to two-phase flow and also upscaling from core scale to field scale.

Nomenclature

A = matrix area (cm^2)
f = friction factor
k_m = matrix permeability (Darcy)
k_f = fracture permeability (Darcy)
L = core length (cm)
l = diameter of the core (cm)

q_m = matrix flow rate (cc/sec)
q_f = fracture flow rate (cc/sec)
w = effective fracture width (cm)
Δp = pressure drop across the core (atm)
μ = viscosity (cp)

Table 1.1—Experimental error analysis.

Overburden Pressure, psia	K_m, md	Pressure Drop psia	Q_m cc/min	Q_m cc/min		Q_f cc/min		Error in Q_f, %
				mean	Std dev	mean	Std dev	
500.00	max = 299.96	1.00	1.21	1.44	±0.27	3.56	±0.27	7.59
		1.40	1.70					
	min= 292.44	1.00	1.18					
		1.40	1.66					
1000.00	max = 273.02	2.20	2.44	2.41	±0.11	2.59	±0.11	4.25
		2.30	2.55					
	min = 255.41	2.20	2.28					
		2.30	2.39					
1500.00	max = 240.12	4.20	4.11	4.34	±0.47	0.66	±0.47	70.68
		5.00	4.90					
	min = 222.23	4.20	3.80					
		5.00	4.53					

Table 1.2—Fracture properties obtained from pressure drop match.

Overburden Pressure (psia)	Fracture aperture (microns)	Average Kf (md) dp match
498.05	74.5	470,000.00
985.65	57.6	280,000.00
1500.5	41.3	146,500.00

Table 1.3—Comparison of fracture properties from simulation and experimental results.

Qinj	Pressure	Aperture width (experiments)		Aperture width (simulation)
cc/min	psia	mean (microns)	σ (microns)	microns
5	500	56.15	±4.73	74.51
	1000	40.40	±0.59	54.62
	1500	20.57	±5.80	41.36

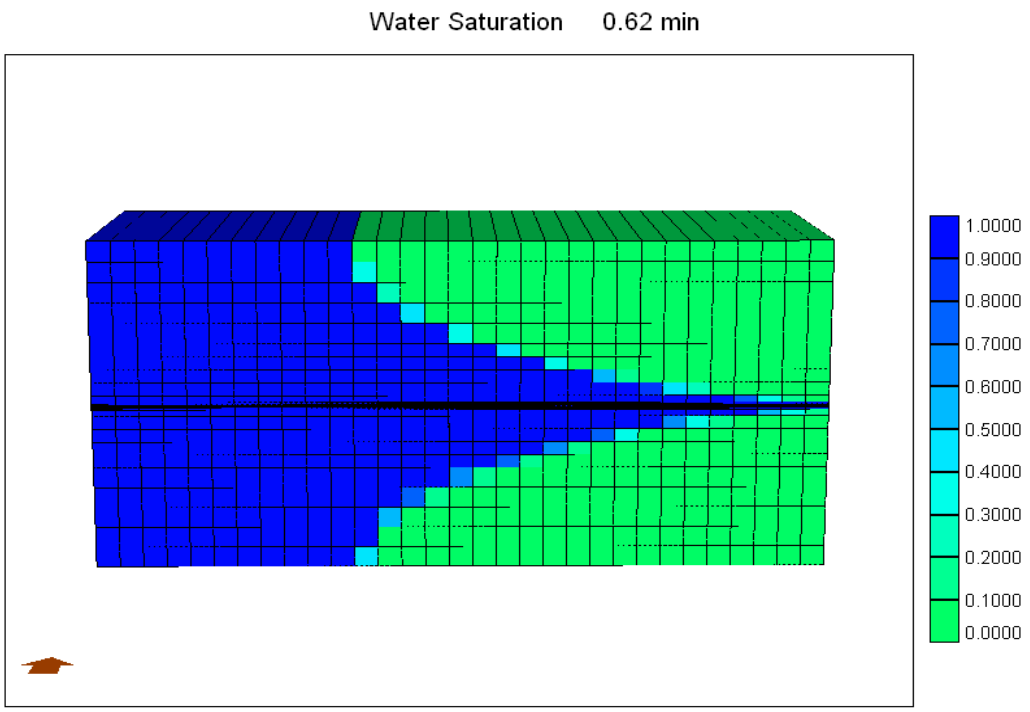

Figure 1.1—Water saturation change in matrix and fracture at transient flow condition.

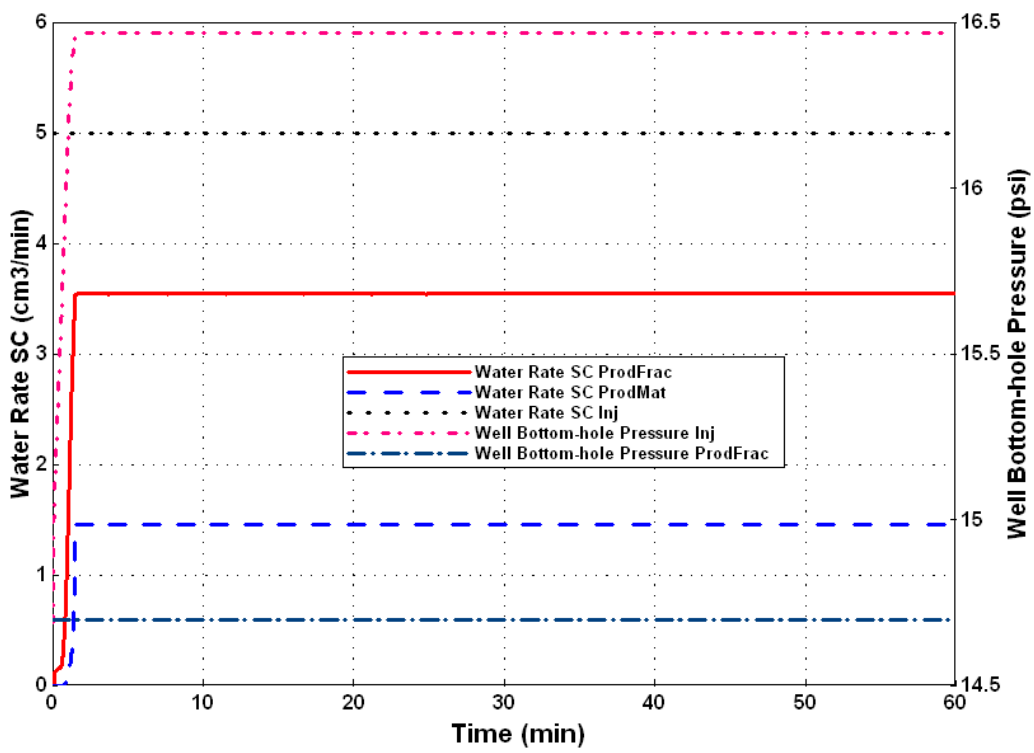

Figure 1.2—Simulation results of flow rates and pressure drop injected at 5cc/min and overburden pressure of 500 psi.

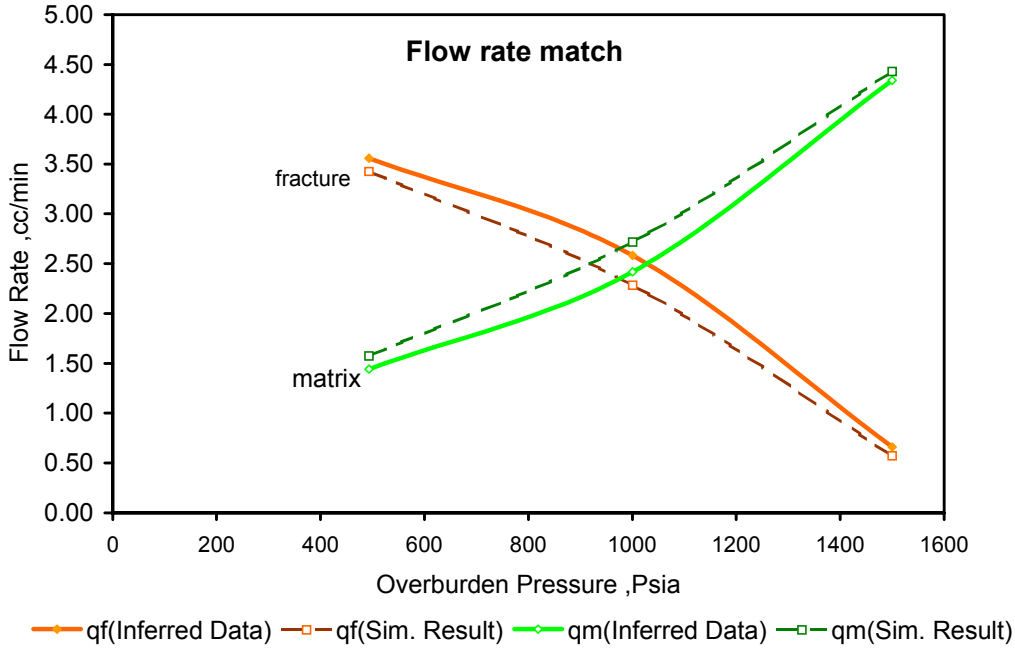

Figure 1.3—Average flow rate comparison between laboratory and simulation results at 5 cc/min and each different overburden pressure.

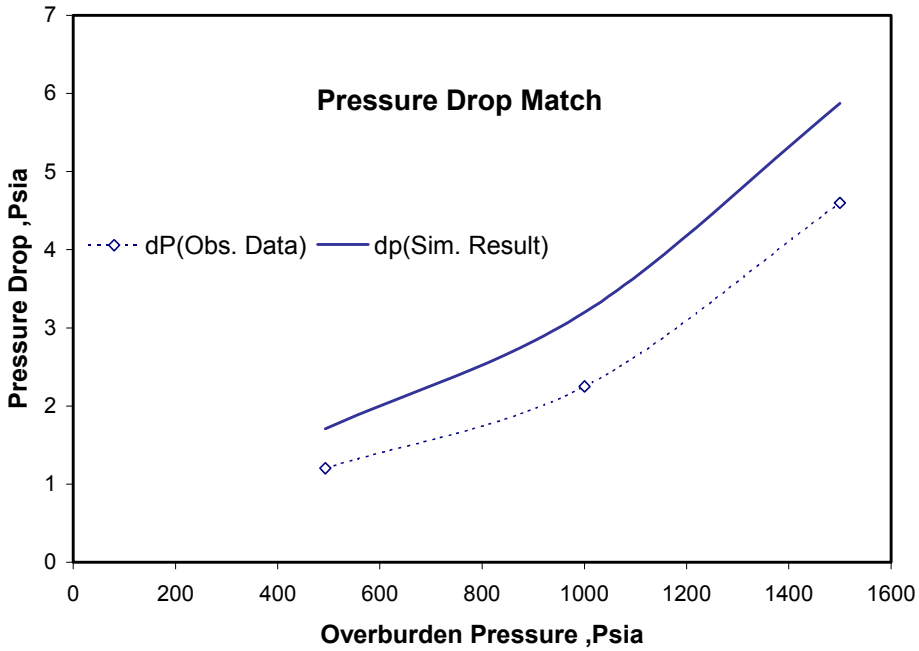

Figure 1.4—Average pressure drop comparison between laboratory and simulation results at 5 cc/min and each different overburden pressure.

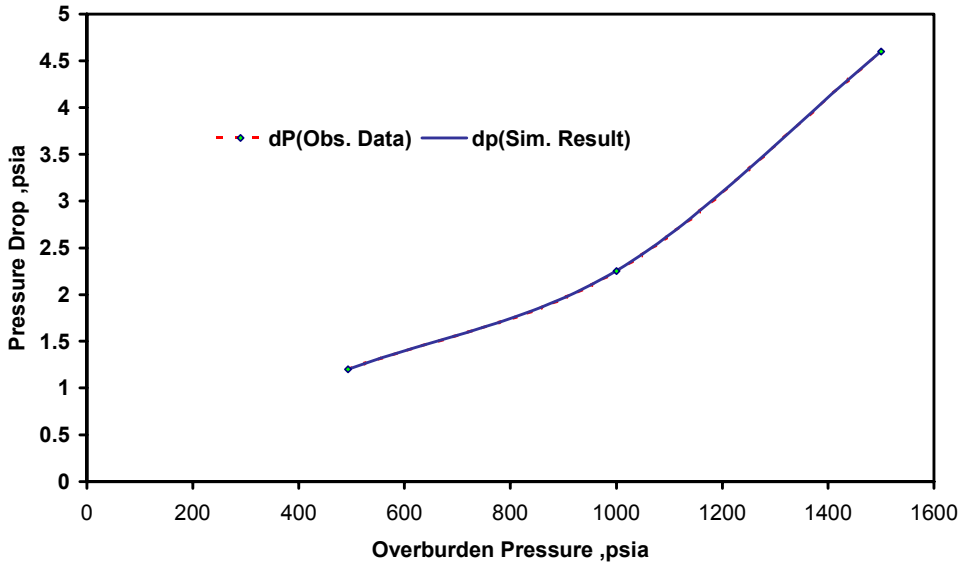

Figure 1.5—Average pressure drop match between observed and simulation results for the fractured core experiment for 5 cc/min injection rate.

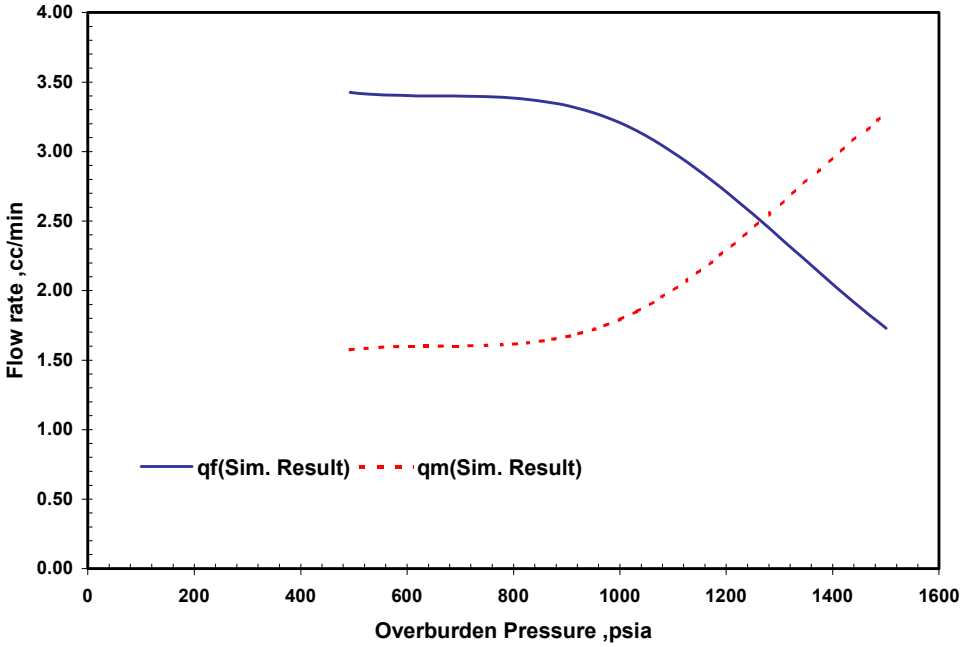

Figure 1.6—Average flow rates observed for the corresponding average pressure drop match across the core at 5 cc/min injection rate.

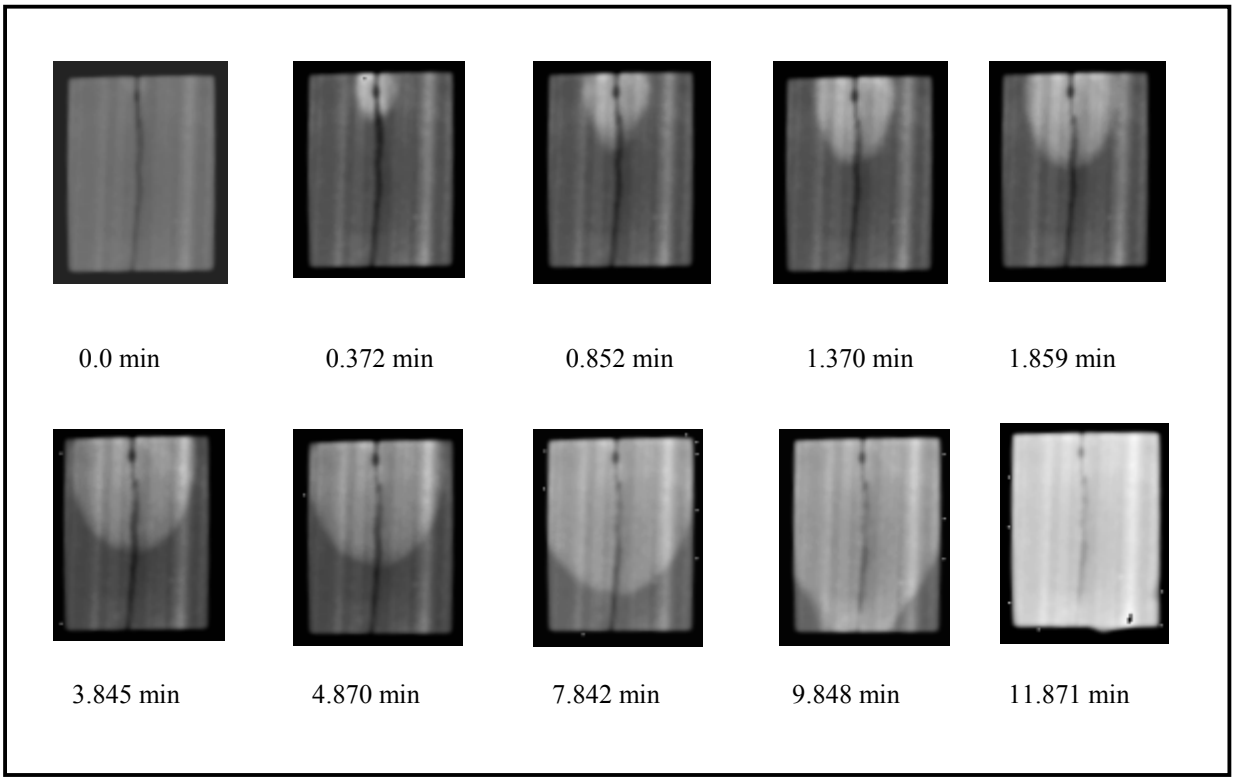

Figure 1.7—X-ray CT scans (perpendicular to the fracture) of single-phase gravity drainage experiment through a fractured core.

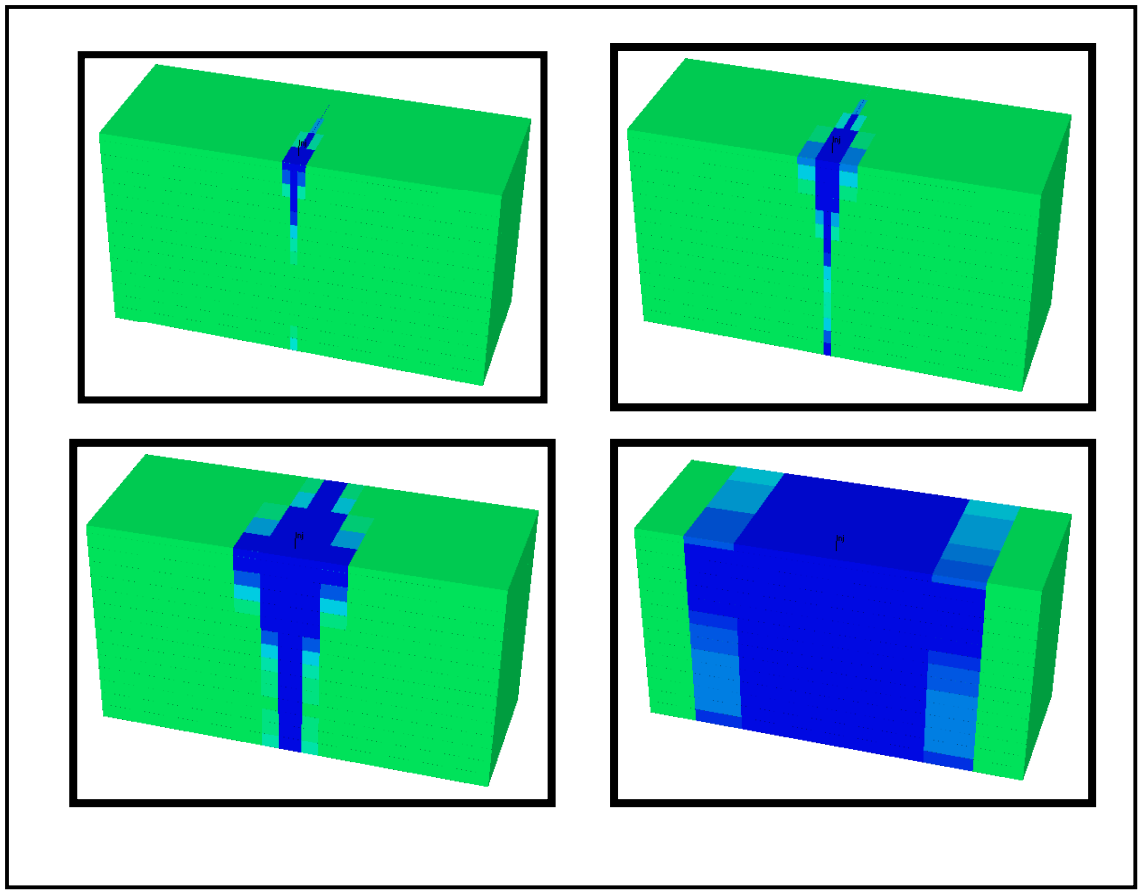

Figure 1.8—Fluid movement through a core with smooth fracture.

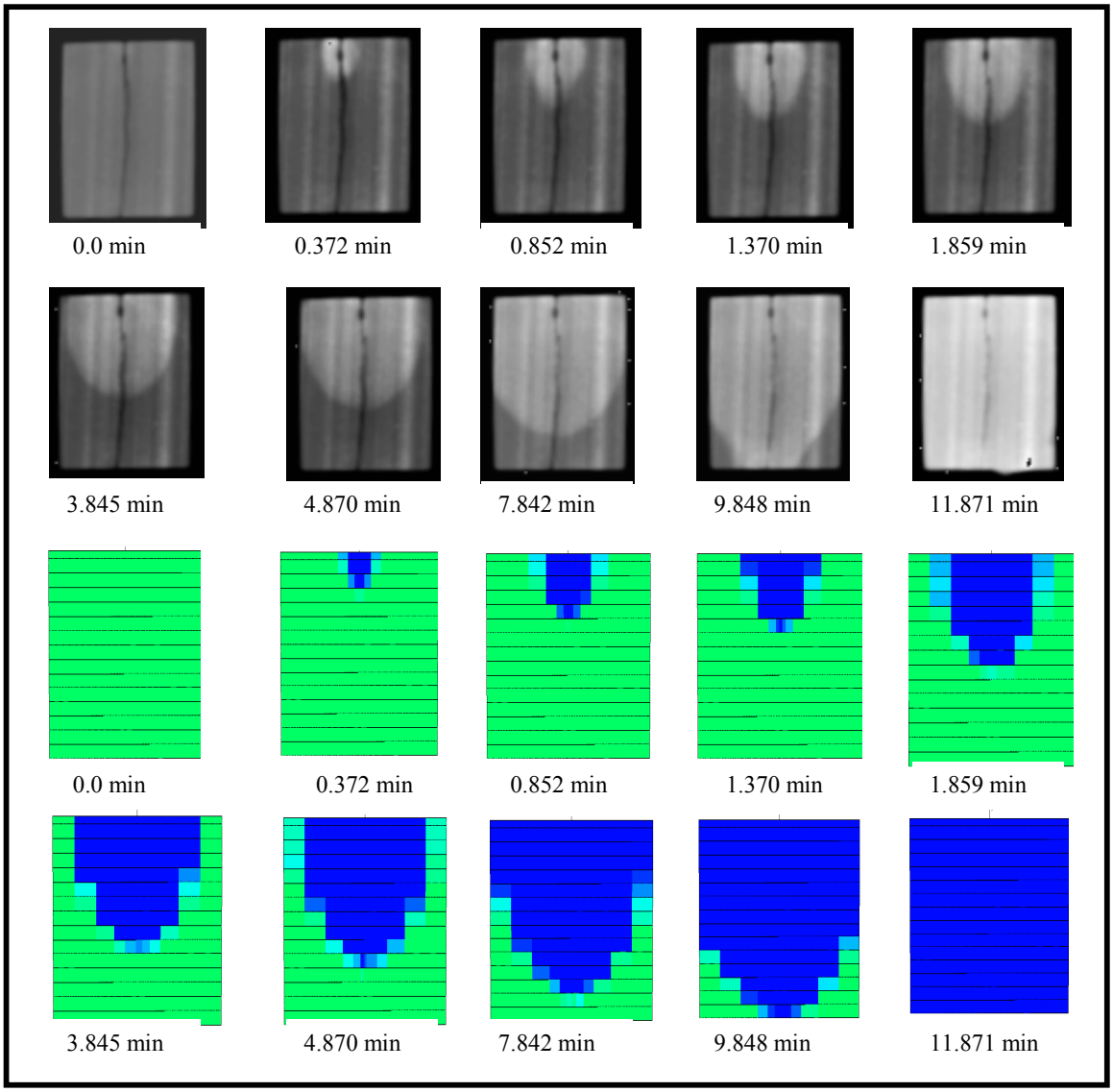

Figure 1.9 —Fluid front movement through a core with a distributed fracture surface.

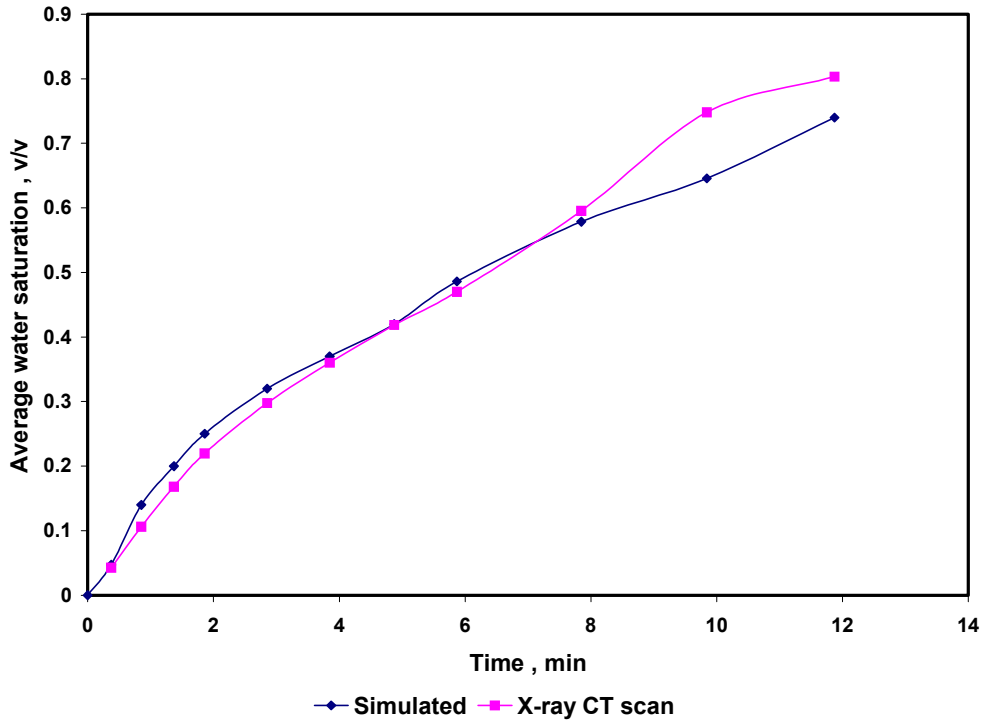

Figure 1.10—Average water saturation match between simulation and X-ray CT scan.

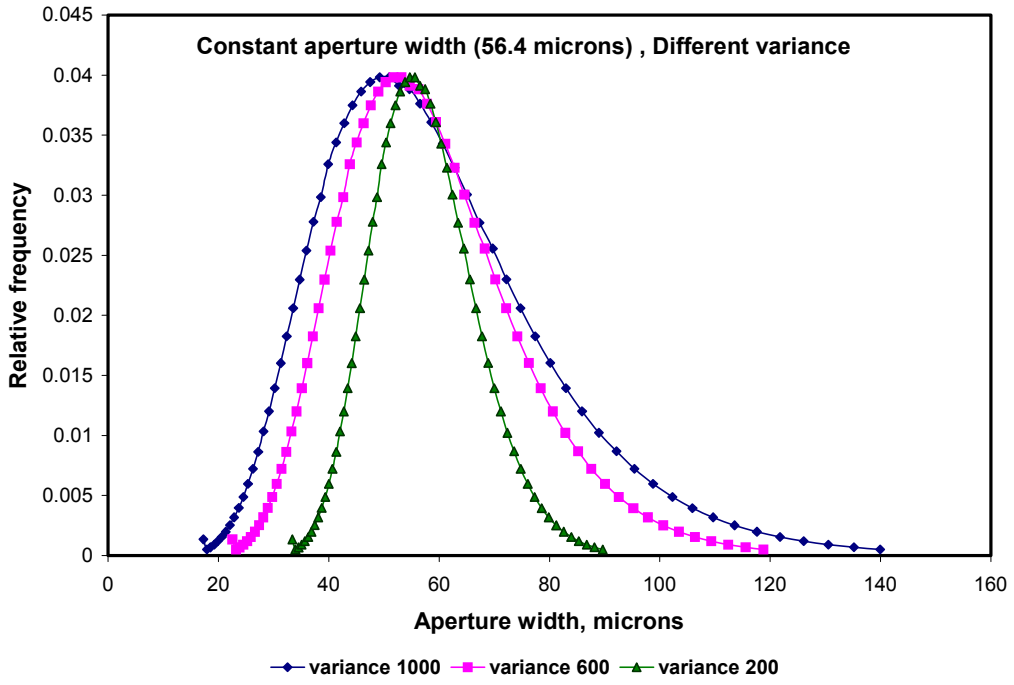

Figure 1.11—Log-normal distribution for constant aperture width, different variances.

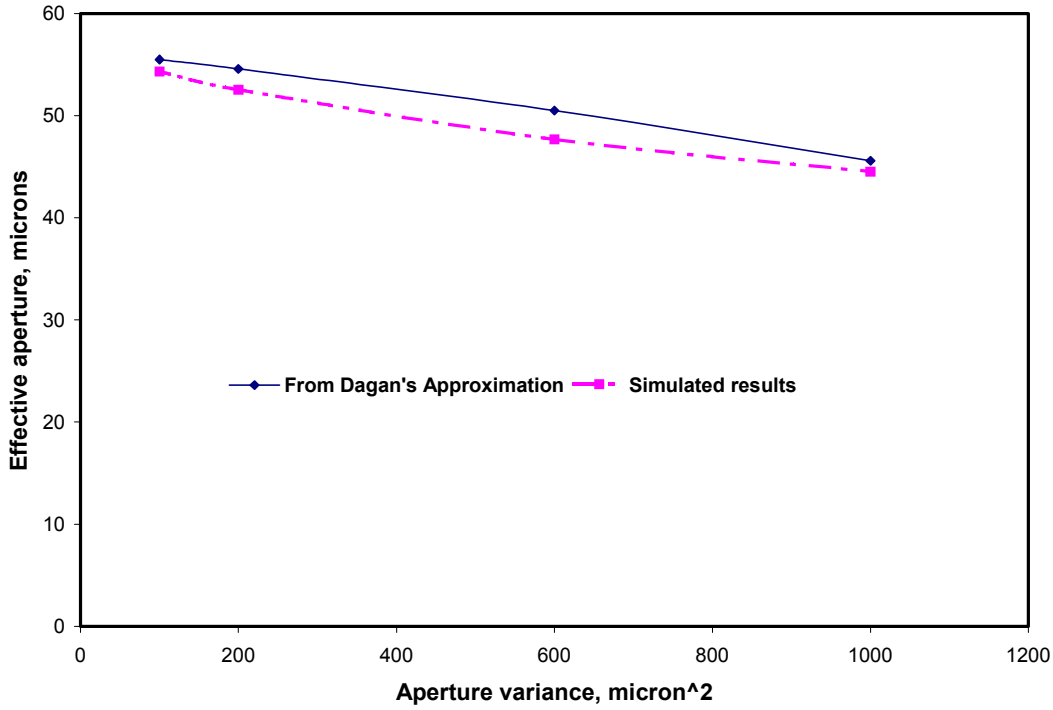

Figure 1.12—The comparative plots of hydraulic aperture reduction as a result of increased roughness (variance)

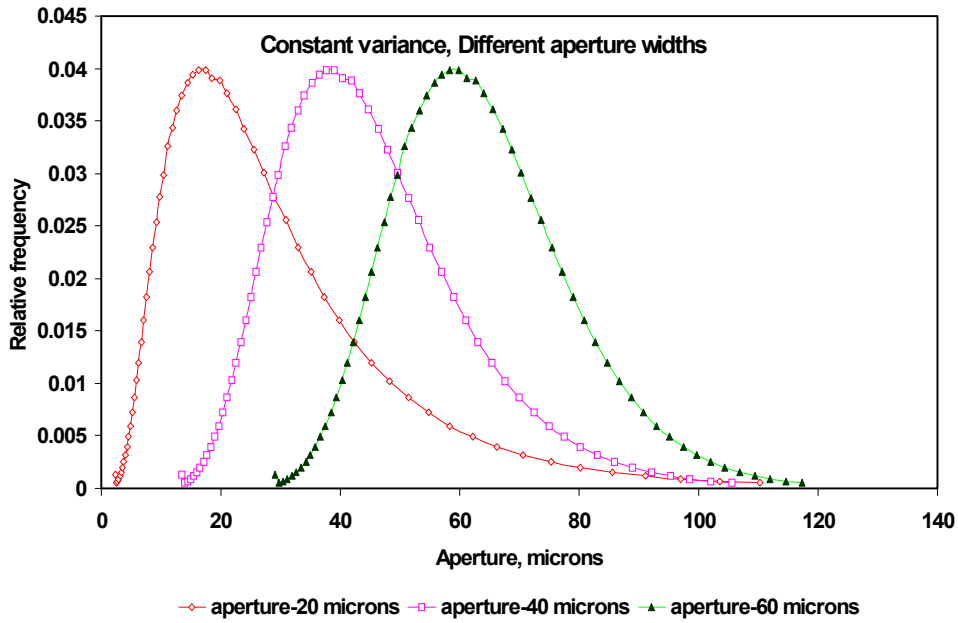

Figure 1.13 —Log-normal distribution for constant variance, different aperture widths.

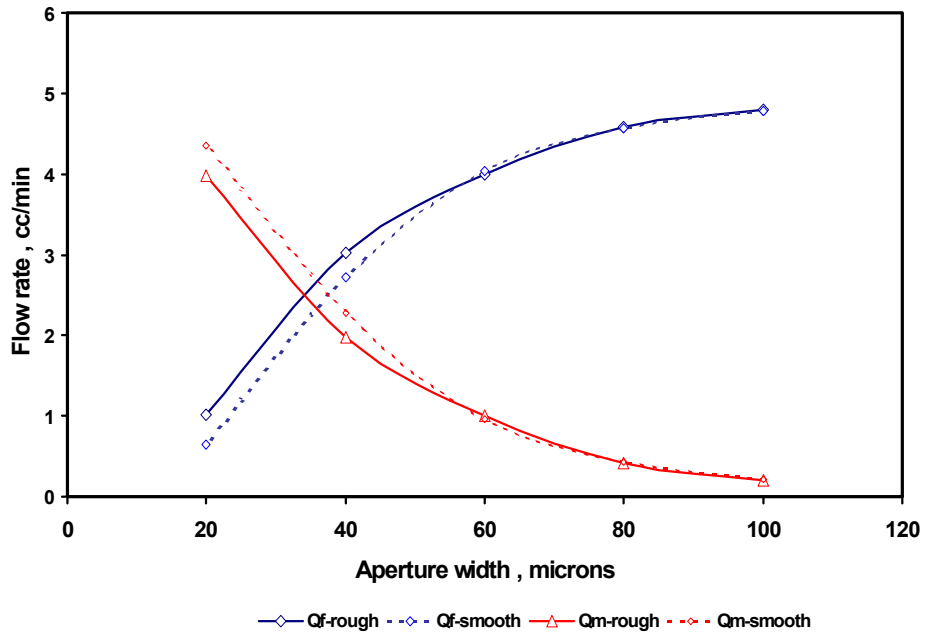

Figure 1.14—Comparison between parallel plate (smooth) and distributed aperture flow (rough) for different apertures.

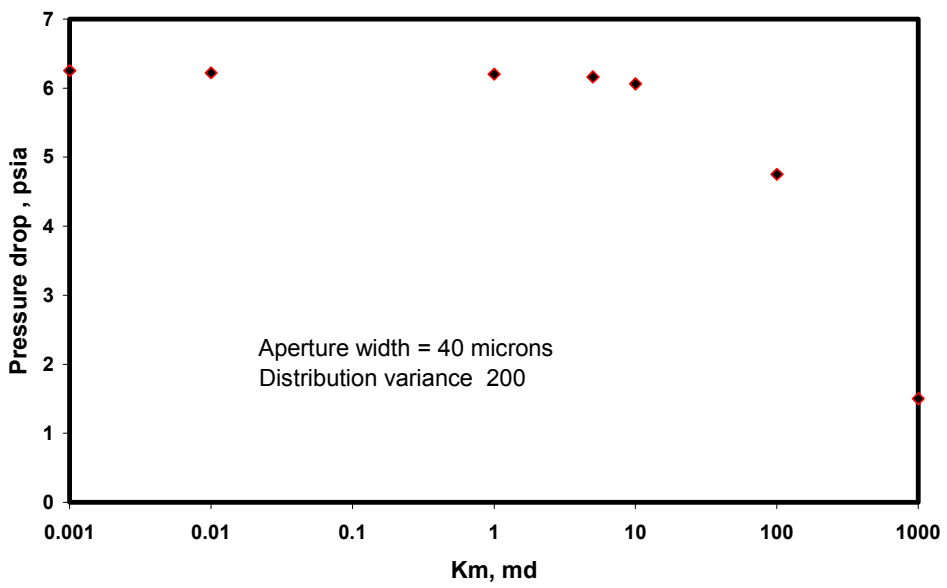

Figure 1.15—Effect of matrix permeability on pressure drop across the core.

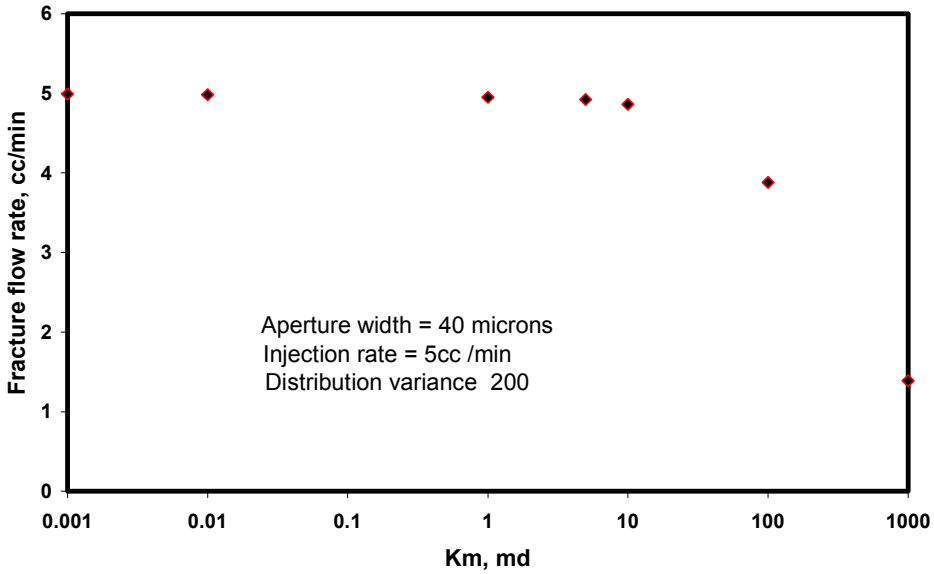

Figure 1.16—Effect of matrix permeability on fracture flow rate.

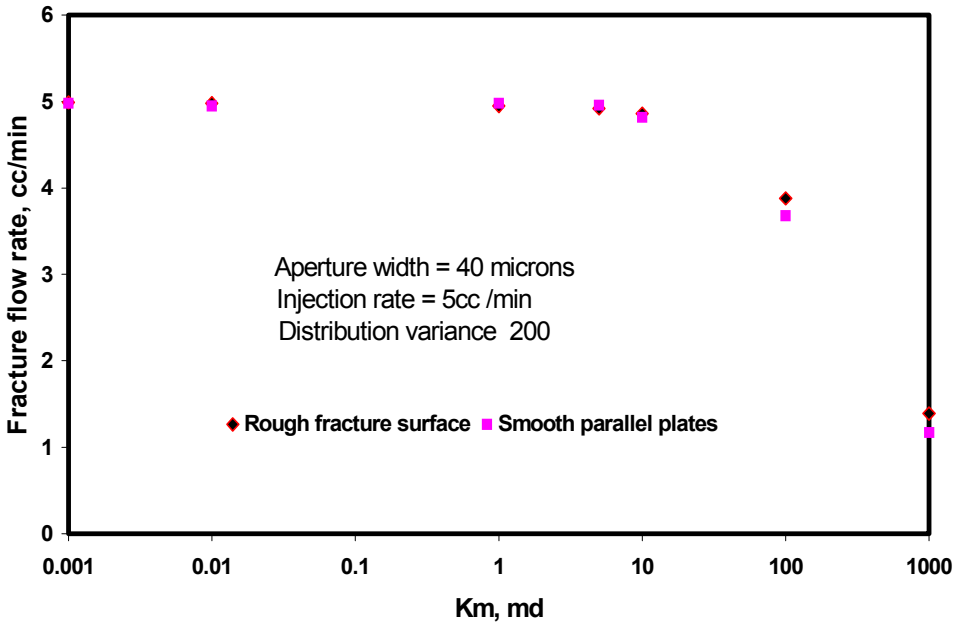

Figure 1.17—Comparison of fracture flow rates between smooth and rough fractures for different matrix permeabilities.

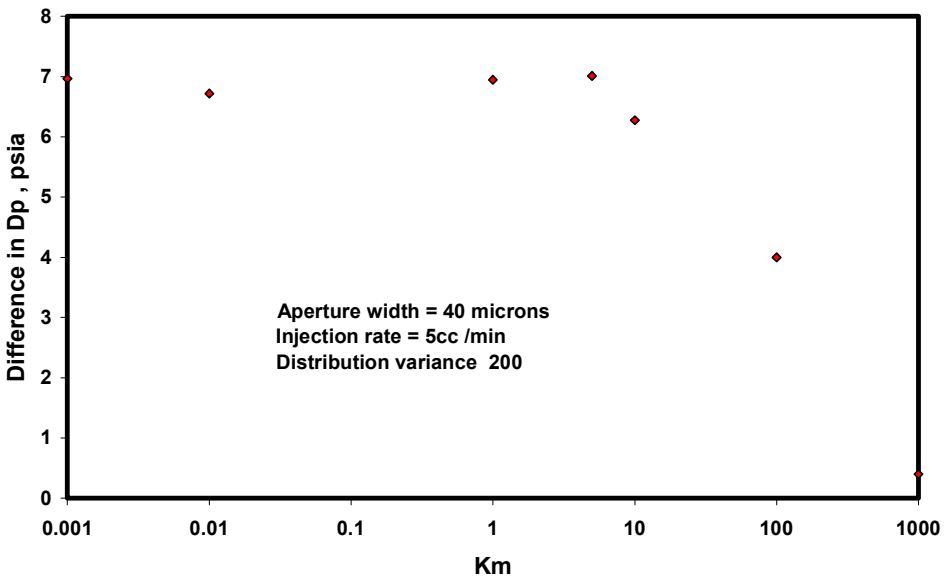

Figure 1.18—Difference in pressure drop across the core between smooth and rough fractures at different matrix permeabilities.

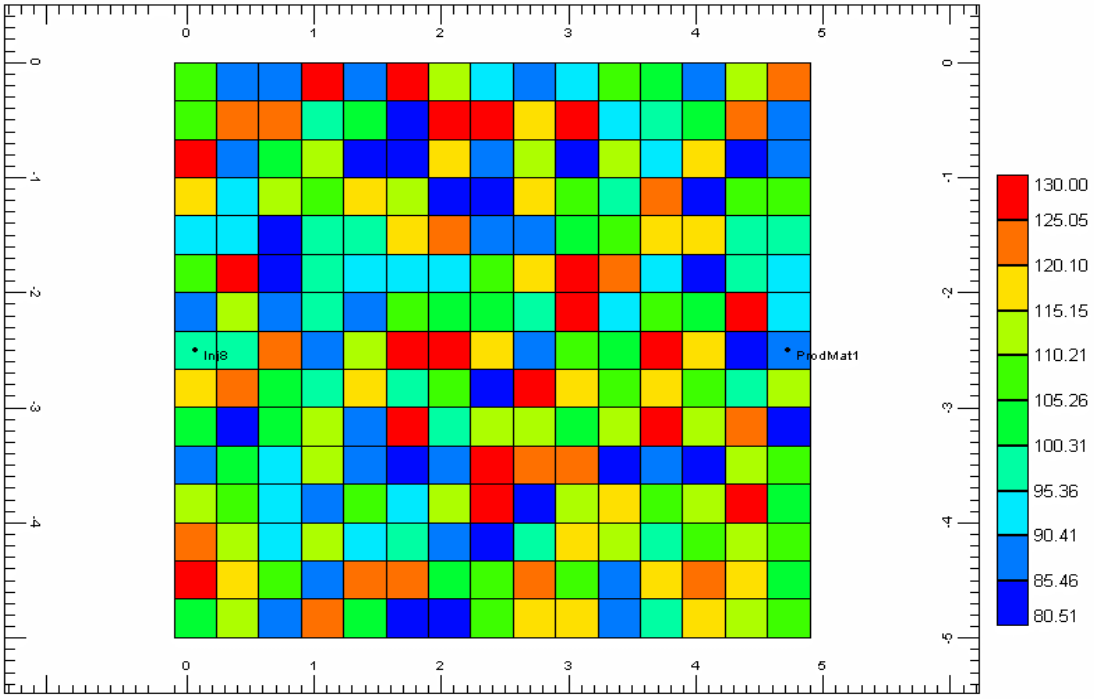

Figure 1.19—Distribution of matrix permeability layer (case 2).

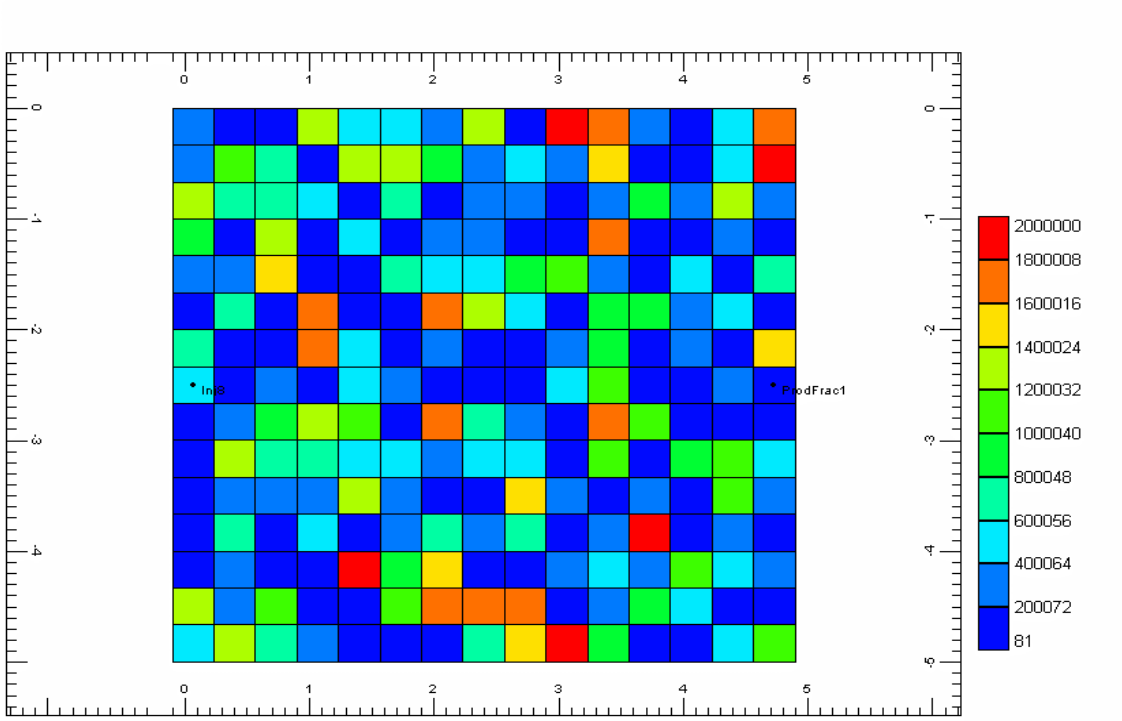

Figure 1.20—Distribution of fracture permeability layer (cases 1 and 2).

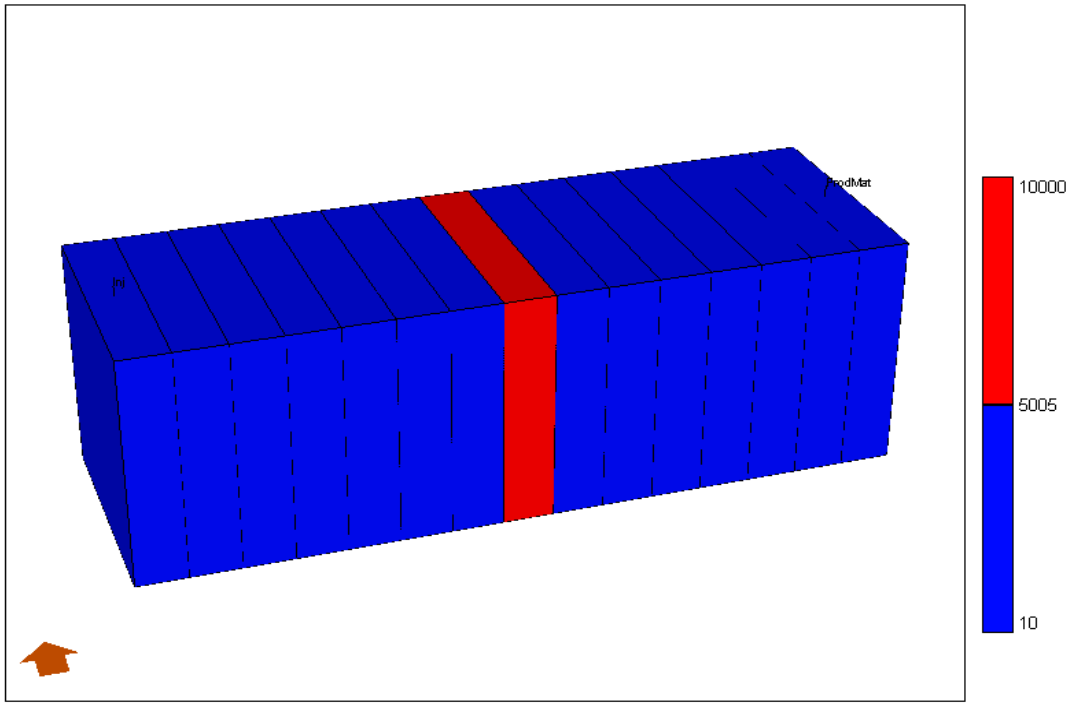

Figure 1.21—One-dimensional model employed in simulation testing.

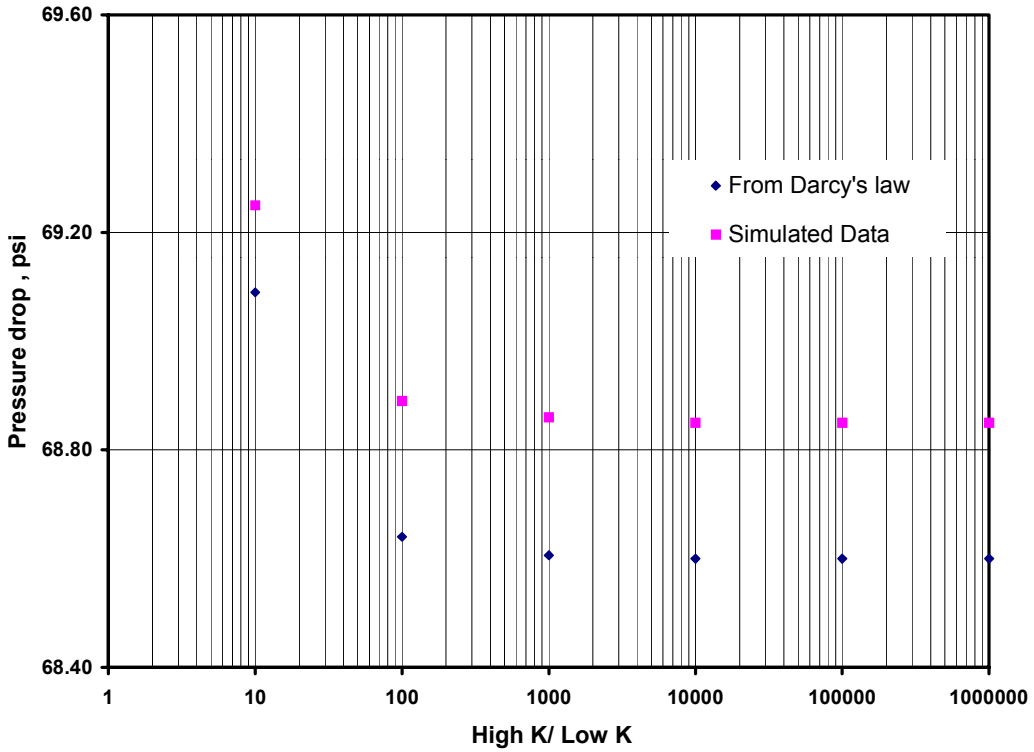

Figure 1.22—Comparative plot of pressure drops observed from simulation and through Darcy's law.

REFERENCES

1. Schechter, D.S.: "Investigation of Efficiency Improvements during CO_2 Injection in Hydraulically and Naturally Fractured Reservoirs," Second Semi-Annual Technical Progress Report, US DOE Contract No.: DE-FC26-01BC15361, (October 2002).
2. Putra, E., Fidra, Y., and Schechter, D.S.: "Study of Waterflooding Process in Naturally Fractured Reservoirs from Static and Dynamic Imbibition Experiments," paper SCA 9910 presented at the 1999 International Symposium of the Society of Core Analysts, Colorado, 1-4 August.
3. Alfred, D.: "Modeling Fluid Flow Through a Single Fracture Using Experimental, Stochastic and Simulation Approaches," master's thesis, Texas A&M University, 2003.
4. Zimmerman R.W. and Bodvarsson, G.S.: "Hydraulic Conductivity of Rock Fractures" *Transport in Porous Media* (1996), **23**, 1-30.

II. SIMULATION OF NATURALLY FRACTURED RESERVOIRS USING EMPIRICALLY DERIVED TRANSFER FUNCTION

2.1 INTRODUCTION

Proper simulation and modeling of naturally fractured reservoirs is a challenging issue in reservoir engineering.[1, 2, 3] Fractures play an important role in fluid distribution and flow in a naturally fractured reservoir. Hence their proper characterization is of great significance to the validity of the simulation results. Two divergent approaches are present for the proper simulation of naturally fractured reservoirs, single continuum methods and dual continuum methods.

Single continuum methods treat the matrix and fracture as one. Grid blocks are assigned high permeability and low porosity values, to represent fractures. Although this method yields accurate results, this method is usually very slow and taxes both computation speed and memory.

Dual continuum methods decouple the pore space into fractures and matrix. Dual porosity methods, probably synonymous with dual continuum methods, were first introduced by Warren and Root[4] and result in simplified computation techniques. Dual porosity models assume that the fracture medium is the main flow path and the matrix provides fluid storage only. The fracture and matrix medium are coupled by a factor called the transfer function, which physically represents the flow of fluids from the matrix to the fracture.

Dual Continuum methods, to date, utilize statistics and history matching to estimate the value of the shape factor. This shape factor is essentially the coupling factor between the matrix and fracture (Gilman[5]) and is the key for transfer between fracture and matrix. The equations for the single and dual continuum methods are provided in the next section.

Lab imbibition experiments provide an estimate of the relative permeability and capillary pressures.[6, 7] In these experiments the core can be idealized as matrix and the adjoining wetting phase as the fracture. The rate of change of water saturation in the core gives us an estimate of the rate of change of matrix saturation when surrounded by a fracture filled with wetting phase. This in essence, is the rate of transfer of fluids from matrix to the fracture. Imbibition experiments using X-Ray CT scans provide us with the saturation of the non-wetting phase within the core. In addition to the recovery, the saturation also needs to be accounted for to provide an accurate transfer function. The present research proposes to utilize the laboratory experiments (recovery of non-wetting phase) as the transfer function term in the dual porosity simulation.

2.2 LITERATURE REVIEW AND PRESENT STATUS

With increasing numbers of deep-water exploration, more fractured, vuggular and heterogeneous reservoirs are being explored and developed. This has increased the interest the petroleum industry has towards more unconventional and fractured reservoir modeling. With the advent of faster computers with large amounts of memory storage, the industry is now able to model complex reservoirs faster and with increasing accuracy. In this section, commonly used approaches for naturally fractured reservoir modeling and inter-porosity flow estimation are reviewed. Modeling of fluid flow in naturally fractured reservoirs can be broadly classified into the following models[7]:

1. Discrete Fracture Network Models.
2. Hybrid Models.
3. Equivalent Continuum Models.

Discrete networks consist of modeling a population of fractures. Equivalent Continuum methods model reservoirs by assigning equivalent rock and fluid parameters to large rock masses. Hybrid models are a combination of both discrete fracture networks and equivalent continuum methods. Although the selection of any particular model depends not only on the reservoir and the type of fluid flow behavior to be numerically simulated,

but also on the amount of computer memory and processor power available for the project. In general, the equivalent continuum modeling approach is the favored approach to model naturally fractured reservoirs because of the ease of computation. Whenever large models with accurate data are to be solved with a high degree of accuracy, the other two models may be applied. It has been shown that the equivalent continuum method is sufficient to model reservoir rocks that have undergone multiple and extensive deformations (high fracture density) and/or any formations where matrix permeabilities are large enough that fluid flow is not influenced by any individual fracture or series of fractures that form a conducting channel[18]. Because of the focus to this study, the most important equivalent continuum models – single-porosity and dual-porosity models – are briefly reviewed.

Single Porosity Modeling. Single Porosity modeling is the common method of modeling non-fractured reservoirs. This model does not differentiate between the matrix and the fracture continua and the equivalent rock and fluid properties are assigned to both the continuum. Agarwal *et al*[19] have used the single continuum method to model a carbonate reservoir with large number of fractures in the North Sea. Since this methodology doesn't differentiate between any of the continuum, this can be safely said to be the most accurate modeling method. But its accuracy is dependent on the number of grid-blocks used. Most of the single porosity modeling of naturally fractured reservoirs is done with a large number of grid blocks for greater accuracy and thus can lead to large computational times.

To circumvent this problem Agarwal *et al*[19] used pseudo-relative permeability functions. In developing these pseudo-relative permeability curves, dual porosity simulation was done on a stack of matrix blocks and then the relative permeabilities developed were matched with fine grid simulation. This method receives special consideration because of the ease of computation produced by this methodology. The problem with the methodology was that new sets of dynamic pseudo-functions had to be calculated for changes in operating conditions.

Dual Porosity Modeling. Dual porosity simulation is the mathematical modeling of fluid flow in reservoirs with significant secondary porosity. To model fluid flow it is necessary to spatially define the secondary porosity. Since this process is inherently complex and cannot be easily quantified, an idealization is made. This idealization was initially proposed by Barenblatt *et al*[20]. This approach was proposed for single-phase fluid flow and consisted of dividing the porous media in two superimposed media, a continuous system of fractures (secondary porosity) and a discontinuous matrix (primary porosity) system. The fracture system is further assumed to have negligible storage capacity, but to be the primary flow path. Meanwhile the matrix (primary porosity) is assumed to be the storage medium of the system but has negligible flow capacity. This idealization was introduced to the petroleum engineering by Warren and Root[21] who presented an analytical solution for the single phase radial flow in a reservoir with significant contribution of the secondary porosity towards flow. The idealization made the following assumptions:

- The primary porosity is isotropic and is contained in a symmetric array of identical parallelepipeds.
- All the secondary porosity is contained in a set of orthogonal fractures, which are oriented in a direction parallel to the axis of permeability.
- Flow can occur in the secondary porosity and from the primary porosity to the secondary porosity, but not in the primary porosity.

The idealization can be visualized as in **Fig. 2.1**. Both the primary and fracture media are consistent in neither orientation nor continuity in **Fig. 2.1** (a), which is the actual reservoir. This actual reservoir is idealized as shown in **Fig. 2.1** (b). The idealized reservoir can be viewed as a series of primary porosity contained in the parallelepipeds, which are disconnected from each other, by a series of continuous secondary porosities.

Other idealizations include parallel horizontal fracture[22] and matchstick column models[4]. Multi-porosity models are a special case of dual porosity models, which assume that the

fracture set interacts with two groups of matrix blocks with distinct permeabilities and porosities[23].

2.3 TRANSFER FUNCTION

The primary and secondary porosities are coupled by a factor called the transfer function or the inter-porosity flow. Physically this can be termed as the rate of fluid flow between the primary and the secondary porosities. Since the secondary porosity is the only fluid path and it lacks in fluid storage, the dual porosity simulation method can be imagined as a system of secondary porosity with the primary porosity as the major source for the fluid. The transfer function can be regarded as the "heart" of the dual porosity. The transfer function is the parameter that is changed to effect the transition from the actual reservoir as shown in **Fig. 2.1 (a)** to the ideal reservoir as shown in **Fig. 2.1 (b).** Transfer functions can be broadly classified into four types

1. Empirical Transfer Functions.
2. Scaling Transfer Functions.
3. Diffusivity Transfer Functions.
4. Transfer Functions that use Darcy Law.

2.3.1 Empirical Transfer Functions

Empirical models assume the transfer or inter-porosity flow can be attributed to the imbibition phenomenon. They assume a function is used to describe the time rate of exchange of oil and water for a single matrix block when surrounded by fractures with high water saturation. Empirical transfer functions usually consist of two parts

1. A curve fitting expression to describe recovery as a function of time.
2. A scaling equation to express the time in terms of rock and fluid properties.

The first empirical oil recovery function was given by Aronofsky[24]. He showed that the rate of transfer of fluids from the matrix can be approximated by an exponential decline function as shown

$$R = R_{\infty}(1 - e^{-\lambda t}) \tag{1}$$

deSwaan[25] used the above relation to derive an analytical expression for the water oil ratio and the cumulative oil production from a linear reservoir with water flooding. His theory also accounts for the fact that in a reservoir exploited by water flooding, the matrix blocks downstream from the waterfront are subject to varying degree of saturation of fractures due to the water imbibition of the matrix blocks upstream. His theory modifies the well-known Buckley-Leverett formulation by addition of a term for the inter-porosity flow or the transfer function.

$$-\frac{\partial q}{\partial x} = h\phi \frac{\partial S_w}{\partial t} + \frac{N_{ma}}{\tau_1} \int_o^t e^{-(t-\theta)/\tau 1} \frac{\partial S_w}{\partial \theta} d\theta \tag{2}$$

Also assuming that the fractional flow coefficient is the same as the mobile water saturation, he derived an analytical solution for the above equation. The analytical solution contains an integro-differential term to account for the inter-porosity flow:

$$S_w = \begin{cases} 0, t < t_{Lf} \\ 1 - e^{-t/\tau} \int e^{-y} I_o(2\sqrt{ty/\tau}) dy, t > t_{LF} \end{cases} \tag{3}$$

Kazemi et al[26] solved the analytical expression derived by deSwaan by using explicit finite difference and trapezoidal rule. Reis and Cil[27] proposed a new relation for oil recovery function

$$R = R_{\infty}(1 - e^{-0.69(\lambda t)^n}) \tag{4}$$

Civan[28] extended the Arfonsky relation by addition of an exponential term as shown in equation 2.5:

$$R = R_{\infty}(1 - e^{-\lambda t_1} - e^{-\lambda_2 t}) \tag{5}$$

The second exponential term was justified by the fact that the collection of oil droplets in the fracture consist of two different irreversible processes, namely:

1. Expulsion of oil droplets from the matrix into the fracture.
2. Entraining of the oil droplets in the fracture by the fluid present in the fracture.

Equation 5 was used in the Buckley-Leverett equation, similar to deSwaan, and a numerical solution was developed. This numerical solution used the quadrature solution. He showed that the quadrature solutions are easier to compute than the finite difference solutions for the case of end point mobilities. Civan and Gupta[29] proposed an additional term to the equation 2.5 as shown below:

$$R = R_{\infty}(1 - e^{-\lambda t_1} - e^{-\lambda_2 t} - e^{-\lambda_3 t}) \tag{6}$$

The third term was added to include the "dead-end" pores of the matrix but the results obtained did not justify the need for the inclusion of this third term[30]. The above said empirical methods suffer from the following fallacies:

1. This method is limited to water flooded reservoirs.
2. The capillary pressure role in oil recovery is neglected.
3. Gravity is neglected.
4. This method is limited to two phases only.

2.3.2 Scaling Transfer Functions

Scaling transfer functions are used to predict recovery in field size cases, together with the results from lab experiments. Rapoport[31] proposed the "scaling laws" applicable in case of water-oil flow. Using these laws Mattax and Kyte[32] presented the dimensionless time to scale up laboratory data to field size cases. The dimensionless time is given as:

$$t_D = t\sqrt{k/\phi}\left(\frac{\sigma}{\mu_w L^2{}_c}\right) \tag{7}$$

Du Prey[33] performed imbibition experiments on cores within centrifuges to account for gravity effect on imbibition. He showed that the dimensionless time defined by the previous equation couldn't be used to model the experiments. He also showed that the dimensionless equation 7 couldn't be used for matrix blocks of different sizes. He defined three more dimensionless parameters

- Dimensionless shape factor
- Dimensionless mobility

- Capillary to gravity ratio

The dimensionless time was defined for two low capillary to gravity ratio and for high capillary to gravity ratio. His definitions are as follows:

$$t_c = \frac{H^2 \phi \Delta S \mu_o}{P_{ct} k_{o\max}}$$
$$t_g = \frac{H \ \phi \Delta S \mu_o}{\Delta \rho g k_{o\max}} \tag{8}$$

Where

t_c	Dimensionless time factor for high capillary gravity ratio
t_g	Dimensionless time factor for low capillary gravity ratio

Ma et al[34] studied the relationship between water wetness and the oil recovery from imbibition. The characteristic length to scale up time was also defined for various cases. The authors also defined "effective viscosity" to remove the issue of comparable viscosities between the lab and field cases.

$$t_D = t\sqrt{\frac{k}{\phi}}\frac{\sigma}{\mu_g}\frac{1}{L_c^2} \tag{9}$$

where

$$\mu_g = \sqrt{\mu_w \mu_{nw}} \tag{10}$$

Although the scaling transfer functions are the best transfer function representations, the following are the requirements for the correct formulation of scaling transfer functions:

1. The shapes of the matrix blocks for the field and lab cases must be of the same shape.
2. The fluid mobilites must be comparable.
3. The initial and boundary conditions for both the lab and matrix cases must be the same.

4. The capillary pressures must be directly proportional.

Because of these inherent assumptions the scaling transfer functions are not widely used.

2.3.3 Transfer Function Using Darcy Law

Transfer functions that use "Darcy's Law" assume that the transfer of fluids from the matrix to the fracture can be adequately be described by Darcy's law with an appropriate geometric factor that accounts for the characteristic length and the flow area between the matrix and the fracture.

The first model was proposed by Barenblatt *et al* which is analgous to a model used for heat transfer in a heterogeneous medium. They assumed that the outflow of fluids from matrix blocks into the fractures is steady-state and that the fluid transfer rate is a function of the viscosity of the fluid, the pressure drop between the matrix and fracture systems, and matrix-rock properties related to geometry and porous interconnectivity in the matrix block. According to Barenblatt *et al.*, the fluid transfer rate per unit volume of rock is calculated from the following expression:

$$q = \frac{\sigma K_m}{\mu}(p_m - p_f) \tag{11}$$

Where σ is a shape factor related to the specific surface of the fractures, p_m and p_f are the average pressures in the matrix and fracture domains, respectively, and q is the fluid transfer rate between the matrix and fracture. Although this transfer function is the most popular, there is hardly any agreement between various researchers regarding the shape factor. Bourbiaux *et al*[35] presented a comparison of shape factors found in the literature. **Table 2.1** is a modified version of the Bourbiaux table as reported by Penula-Pineda.[36]

Although the transfer functions of this family are the most popular they suffer from the following fallacies

1. These assume a linear gradient of pressures between the matrix and the fracture centers.

2. They also assume that the whole storage is present in the matrix blocks only.
3. These transfer functions lack a lab background that the other methods enjoy.
4. They also assume that all the matrix blocks exist at the same saturation.
5. Recovery from "n" number of matrix blocks is equal to "n" times the recovery from a single matrix block.
6. Linear relative permeability is assumed in the fracture media.

2.3.4 Diffusivity Transfer Functions

These transfer functions assume that the inter-porosity flow can be approximated by "diffusion" phenomenon. These functions are based on incompressible flow and assumes that diffusivity equation[43] is sufficient to model the inter-porosity flow between the matrix and the fracture media. Hernandez and Rosales[44] proposed the first diffusivity transfer function. They developed an analytical equation for the oil production from water flooded reservoirs and verified the same from imbibition experiments on Berea cores.

$$N_{pn} = 1 - \frac{8}{\pi^2} \sum_{n=0}^{\alpha} \frac{1}{(2n+1)^2} \exp[-(2n+1)^2 t_D] \tag{12}$$

Hayashi and Rosales[45] developed a technique for making visual observations of water imbibition processes in porous media saturated with oil. They found that the spontaneous penetration of the water by imbibition was similar to diffusion phenomenon. Also based on experimental results, a theoretical model is proposed for explaining imbibition processes:

$$N_{pn} = 1 - [\frac{8}{\pi^2} \sum_{n=0}^{\alpha} \frac{1}{(2n+1)^2} \exp[-\frac{D(2n+1)^2 \pi^2 t}{L^2}\ ]^2 \tag{13}$$

D is a coefficient to be estimated by trial and error.

2.3.5 Comparison of the Transfer Functions.

Reis and Cil have made comparisons between the various transfer functions on several imbibition experiments with different boundary conditions and found the following:

1. The match between the diffusivity models and the experimental data were found to be good except at early times.
2. The scaling function was found to match the experiments within experimental errors.
3. The empirical function was found to have a good agreement with the experimental values.

For single-phase inter-porosity flow, Najurieta[46] showed that deSwaan's analytical model results were equivalent to numerical solutions provided by Kazemi, which accounted for pressure transient effects by assuming non-steady state flow at the matrix/fracture interface.

The procedure developed in this study is intended for implementation in existing simulators without significantly increasing computational work while representing pressure transient and saturation gradient effects on the inter-porosity flow as accurately as possible. In the following chapter, the conceptual model that is the basis for the proposed procedure was presented.

2.3.6 Flow Visualization Using X-Ray Tomography

Computerized Tomography is a non-destructive technique that utilizes X-Rays and mathematical reconstruction algorithms to generate a cross-sectional slice of an object[47]. Hounsfield[48] patented the first X-ray CT technique which was initially used for medical purposes. The applications of X-Ray CT in the petroleum industry has ranged from detection of rock heterogenties[49, 50,51] to determination of bulk densities[52]. However, the main use of CT has been found in flow visualization.

A detailed explanation of the principles and application of X-Ray CT can be found in the literature.[49]

2.4 METHODOLOGY - PROCEDURE OF STUDY

2.4.1 Simulator to model the imbibition experiments

Imbibition or transfer of fluids can be treated as a diffusion phenomenon. Thus, discretizing the diffusion equation (as shown below) a simulator can be developed to match the recovery of non-wetting phase with time and the spatial variation of saturation.

$$D(S_w) = -(\frac{k}{\phi}\frac{\lambda_w \lambda_o}{\lambda_w + \lambda_o})\frac{dP_c}{dS_w} \qquad \frac{\partial}{\partial t}(\frac{\phi S_w}{B_w}) + \nabla(\frac{kk_{rw}}{\mu_w B_w}\nabla P_c) = 0$$

Where

S_w = Wetting Phase Saturation

ϕ = Porosity

k = Permeability

λ_w = Wetting phase mobility

λ_o = Non-wetting phase mobility

P_c = Capillary Pressure

Conventionally, only the ultimate recovery versus time is matched to obtain the relative permeability and capillary pressure information[24]. However, with the advent of the CT-Scan, saturations, as a function of time and space can be quantified. Matching not only the recovery but also the saturations can lead to identification of heterogeneity in the core, and thus can be effective in modeling of vugs and microfractures.[25,26]

2.4.2 Dual porosity simulator

A dual porosity simulator is developed which uses the recovery of the non-wetting phase with time data as the transfer function. The derivation of the flow equations are as given below.

2.4.2.1 Fracture Flow Equations

Stating Darcy's law for multiphase flow in porous media, we have:

$$\vec{u}_w = -\frac{k\,k_{rw}}{\mu_w}\nabla\Phi_w = -\frac{k\,k_{rw}}{\mu_w}\nabla(p_w + \rho_w gh) \tag{14}$$

$$\vec{u}_o = -\frac{k\,k_{ro}}{\mu_o}\nabla\Phi_o = -\frac{k\,k_{ro}}{\mu_o}\nabla(p_o + \rho_o gh) \tag{15}$$

Since the primary flow path in dual porosity formulation is the fracture we have the Darcy Law as follows:

$$\vec{u}_{wf} = -\frac{k_f k_{rwf}}{B_{wf}\mu_{wf}}\nabla(p_{wf} + \rho_w gh) \tag{16}$$

$$\vec{u}_{of} = -\frac{k_f k_{rof}}{B_{of}\mu_{of}}\nabla(p_{of} + \rho_o gh) \tag{17}$$

From the definition of capillary pressure, the water phase pressure can be expressed in terms of oil phase pressure as:

$$P_c = p_o - p_w = P_c(S_w); \qquad p_w = p_o - P_c \tag{18}$$

Thus 14 can be re-written as:

$$\vec{u}_{wf} = -\frac{k_f k_{rwf}}{B_{wf}\mu_{wf}}\nabla(p_{of} - P_{cf} + \rho_w gh) \tag{19}$$

Consider a control volume (Secondary Porosity) of dimensions Δx, Δy as shown in **Fig. 2.2**. For the sake of brevity, the subscript f is dropped in the derivation of the conservation of mass.

From conservation of mass principle, we have that:

[Rate of change of mass in Control Volume = Rate of Net Influx]

Consider the control volume in **Fig. 2.2**, for the phase water we have:

Rate of change of mass of water in X direction:

$$\rho_w \vec{u}_{wx} \Delta y - (\rho_w \vec{u}_{wx} + \frac{\partial}{\partial x}(\rho_w \vec{u}_{wx})\Delta x)\Delta y$$

Similarly for the Y direction:

$$\rho_w \vec{u}_{wy} \Delta x - (\rho_w \vec{u}_{wy} + \frac{\partial}{\partial x}(\rho_w \vec{u}_{wy})\Delta y)\Delta x$$

Rate of accumulation of water:

$$\frac{\partial}{\partial t}(\phi S_w \rho_w \Delta x \Delta y) + \tau$$

Where τ is the rate of flow of water from the matrix to the fracture, since the primary porosity also contributes to the accumulation of water in the fractures.

Thus the conservation of mass can be written in the following form:

$$\frac{\partial}{\partial t}(\phi S_w \rho_w \Delta x \Delta y) + \tau = (\rho_w \vec{u}_{wy} \Delta x - (\rho_w \vec{u}_{wy} + \frac{\partial}{\partial x}(\rho_w \vec{u}_{wy})\Delta y)\Delta x) + (\rho_w \vec{u}_{wx} \Delta y - (\rho_w \vec{u}_{wx} + \frac{\partial}{\partial x}(\rho_w \vec{u}_{wx})\Delta x)\Delta y) \quad (20)$$

Simplifying equation 20 similar to the conservation of mass as described in the earlier chapter we have,

$$\phi \frac{\partial}{\partial t}(S_w) + \tau_w = \nabla.(\vec{u}_w) \quad (21)$$

Similarly for oil phase we have:

$$\phi \frac{\partial}{\partial t}(S_o) + \tau_o = \nabla.(\vec{u}_o) \quad (22)$$

Substituting equations 17 and 18 in equations 21 and 22, we have that:

$$\phi \frac{\partial}{\partial t}(S_{wf}) + \tau_w = \nabla.(-\frac{k_f k_{rwf}}{B_{wf}\mu_{wf}} \nabla(p_{of} - P_{cf} + \rho_w g h)) \quad (23)$$

$$\phi \frac{\partial}{\partial t}(S_{of}) + \tau_o = \nabla.(-\frac{k_f k_{rof}}{B_{of}\mu_{of}} \nabla(p_{of} + \rho_o g h))$$

We know that the sum of the saturations is unity. Hence:

$$S_o + S_w = 1; S_o = 1 - S_w; \frac{\partial S_o}{\partial t} = -\frac{\partial S_w}{\partial t} \tag{24}$$

Simplifying equation 23 and using 24 in 23, we have that:

$$-\phi \frac{\partial}{\partial t}(S_{wf}) + \tau_o = \nabla.(-\frac{k_f k_{rof}}{B_{of}\mu_{of}} \nabla(p_{of} + \rho_o gh)) \tag{25}$$

$$\phi \frac{\partial}{\partial t}(S_{wf}) + \tau_w = \nabla.(-\frac{k_f k_{rwf}}{B_{wf}\mu_{wf}} \nabla(p_{of} - P_{cf} + \rho_w gh)) \tag{26}$$

Multiplying both sides of the equation by the bulk volume we have:

$$V_p \frac{\partial}{\partial t}(S_{wf}) - V_b \tau_o = \nabla.(a_o \nabla(p_{of} + \rho_o gh)) \tag{27}$$

$$-V_p \frac{\partial}{\partial t}(S_{wf}) - V_b \tau_w = \nabla.(a_w \nabla(p_{of} - P_{cf} + \rho_w gh)) \tag{28}$$

Where

a = Symmetric coefficient defined as:

$a_w = \frac{k_f k_{rwf}}{B_{wf}\mu_{wf}} V_b$

The above equations don't consider source and sink terms such as injection wells, production wells, etc. To include wells into equation 27 and 28 the flow rate is added to the RHS with the convention of positive for production and negative in case of an injector. Therefore equations 27 and 28 can be rewritten as:

$$V_p \frac{\partial}{\partial t}(S_{wf}) - V_b \tau_o - q_o = \nabla.(a_o \nabla(p_{of} + \rho_o gh)) \tag{29}$$

$$-V_p \frac{\partial}{\partial t}(S_{wf}) - V_b \tau_w - q_w = \nabla.(a_w \nabla(p_{of} - P_{cf} + \rho_w gh)) \tag{30}$$

2.4.2.2 Matrix Flow Equations

Consider a matrix control volume similar to **Fig. 2.2**. The rate of inflow into the matrix is zero as there is no flow into the matrix while the rate of outflow from the matrix into the transfer function, the conservation of mass can be written as:

$$0-\tau=\frac{\partial}{\partial t}(\phi S) \tag{31}$$

$$-\tau_w=\frac{\partial}{\partial t}(\phi S)_{wma} \tag{32}$$

$$-\tau_o=\frac{\partial}{\partial t}(\phi S)_{oma} \tag{33}$$

2.4.2.3 Empirical Transfer Function

The empirical equations are derived from the imbibition experiments that are conducted on the matrix core. To scale the time from the imbibition experiments to the field size Mattax and Kyte proposed the following transformation:

$$\left(t\frac{\sigma}{\mu_w L^2}\sqrt{\frac{k}{\phi}}\right)_{model}=\left(t\frac{\sigma}{\mu_w L^2}\sqrt{\frac{k}{\phi}}\right)_{matrixblock} \tag{34}$$

Therefore time can be converted to dimensionless time as:

$$t_D=\left(t\frac{\sigma}{\mu_w L^2}\sqrt{\frac{k}{\phi}}\right) \tag{35}$$

From the imbibition data, a table of the recovery versus time is obtained. The time from the imbibition experiments can be converted to dimensionless form as given by equation 35, and also the recovery can be converted into dimensionless form using the following equation

$$R_D = \frac{R}{V_R} \tag{36}$$

Therefore, from the numerical simulation of the imbibition experiment, a table of the recovery and time in dimensionless units can be obtained. Now the problem resolves by expressing the dimensional recovery in terms of the transfer function.

DeSwaan proposed that the rate of imbibition into the fracture from the matrix could be expressed as:

$$\tau = R_\alpha \lambda \int_o^t e^{-(t_D - \varepsilon)\lambda} \frac{\partial S_{wf}}{\partial \varepsilon} d\varepsilon \tag{37}$$

He also derived the Buckley-Leverett solution for the 1-D, 2-Phase water flooding displacement process. Considering the integral as shown above, the transfer function can be written as:

$$\tau = R_\alpha \lambda \sum_{j=0}^{n} \left\{ [S_{wf}(t_{j+1}) - S_{wf}(t_j)] \prod_{k=j}^{n} e^{-\lambda \Delta t_k} \right\} \tag{38}$$

Simplifying equation 38 we have:

$$\tau = R_\alpha \lambda \{ Sum^{n-1} e^{-\lambda \Delta t_{Dn}} \} \tag{39}$$

Where:

$$Sum^{n-1} = Sum^{n-2} + (S_{wf}{}^{n} - S_{wf}{}^{n-1}) e^{-\lambda \Delta t_{Dn-1}} \tag{40}$$

Equation 29 and 30 combined with equation 39 can be written as:

$$-V_p \frac{\partial}{\partial t}(S_{wf}) - \sum R_\alpha \lambda \{ Sum^{n-1} e^{-\lambda \Delta t_{Dn}} \} - q_o = \nabla.(a_o \nabla(p_{of} + \rho_o g h)) \tag{41}$$

$$V_p \frac{\partial}{\partial t}(S_{wf}) - \sum R_\alpha \lambda \{ Sum^{n-1} e^{-\lambda \Delta t_{Dn}} \} - q_w = \nabla.(a_w \nabla(p_{of} - P_{cf} + \rho_w g h)) \tag{42}$$

Therefore the problem is reduced to a two-unknown, two-equation problem.

2.4.2.4 Discretization of the Equations

Equation 41 and 42 can be discretized as shown in the previous chapter using the finite difference technique, and the following equation can be arrived

$$\Delta a_o \Delta \Phi_o = -\frac{V_p / B_o}{\Delta t} \delta S_w + q_o + \sum R_\alpha \lambda \{ Sum^{n-1} e^{-\lambda \Delta t_{Dn}} \} \tag{43}$$

$$\Delta a_w \Delta \Phi_w = \frac{V_p / B_w}{\Delta t} \delta Sw + q_w + \sum R_\alpha \lambda \{ Sum^{n-1} e^{-\lambda \Delta t_{Dn}} \} \tag{44}$$

Where

a	= Symmetric Coefficient
Φ	= Potential. Defined as
$\Delta \Phi_w$	= Δ(p-P_c) - $\rho_w g \Delta H$
$\Delta \Phi_o$	= Δ(p) - $\rho_o g \Delta H$
Operator Δ	= Defined as

$$\Delta = \frac{\partial}{\partial x} + \frac{\partial}{\partial y}$$

Writing the equations 43 and 44 after finite difference discretization, neglecting gravity we have

$$\begin{aligned} & a^{n+1}_{ow\,i\text{-}1} (\Phi^{n+1}_{i\text{-}1} - \Phi^{n+1}_{i}) + a^{n+1}_{oE\,i} (\Phi^{n+1}_{i+1} - \Phi^{n+1}_{i}) + a^{n+1}_{oS\,j} (\Phi^{n+1}_{j\text{-}1} - \Phi^{n+1}_{j}) + a^{n+1}_{oN\,j} (\Phi^{n+1}_{j+1} - \Phi^{n+1}_{j}) \\ & = -\frac{V_p / B_o}{\Delta t} (Sw^{n+1} - Sw^{n}) + q_o + \sum R_\alpha \lambda \{ Sum^{n-1} e^{-\lambda \Delta t_{Dn}} \} \end{aligned} \tag{45}$$

$$\begin{aligned} & a^{n+1}_{ww\,i\text{-}1} (\Phi^{n+1}_{i\text{-}1} - \Phi^{n+1}_{i}) + a^{n+1}_{wE\,i} (\Phi^{n+1}_{i+1} - \Phi^{n+1}_{i}) + a^{n+1}_{wS\,j} (\Phi^{n+1}_{j\text{-}1} - \Phi^{n+1}_{j}) + a^{n+1}_{wN\,j} (\Phi^{n+1}_{j+1} - \Phi^{n+1}_{j}) \\ & = \frac{V_p / B_w}{\Delta t} (Sw^{n+1} - Sw^{n}) + q_w + \sum R_\alpha \lambda \{ Sum^{n-1} e^{-\lambda \Delta t_{Dn}} \} \end{aligned} \tag{46}$$

The equations 45 and 46 are highly non-linear. With the advent of faster computers the conventional IMPES formulation of the above equation is not necessary as the IMPES method are known for their stability problems. Hence the fully implicit option is applied. To solve the equations mentioned, Newton-Raphson's method of solution can be applied.

Newton-Raphson's Solution of Non-Linear Equations. Consider equations 45 and 46. They can be posed in the matrix form as shown below:

$$\vec{A}\vec{X} = \vec{b} \tag{47}$$

Where

$$\vec{X} = \begin{bmatrix} \Phi_f \\ S_{wf} \\ . \\ . \\ \Phi_f \\ S_{wf} \end{bmatrix}$$

$\vec{A}$ Coefficient Matrix

$\vec{b}$ Right Hand Side Matrix

Since both "A" and "b" matrices in 47 are functions of "X" matrix the system of equations is non-linear. Rewriting the equation:

$$\vec{R} = \vec{A}\vec{X} - \vec{b} \tag{48}$$

Where R matrix is called the residual matrix. Using the Taylor's series expansion the residual matrix can be written as:

$$\vec{R}^{n+1} = \vec{R}^{n} + \left(\frac{\partial \vec{R}}{\partial x}\right)^{n} (\vec{x}^{n+1} - \vec{x}^{n}) \tag{49}$$

Setting R^{n+1} to zero as the objective is to reduce the residual to zero; the following equation can be derived:

$$\vec{R}^{k} = -\left(\frac{\partial \vec{R}}{\partial x}\right)^{k} \Delta\vec{x}^{k+1} \tag{50}$$

Where

Δx^{k+1}	$x^{k+1}-x^{k}$
k	Iteration counter

Equation 50 is similar to 47. Therefore the equations 45 and 46 can be posed in the form of residuals and the partial derivative in the equation 50 can be computed as the coefficient of the change in residual with respect to a variable and the difference matrix can to be computed.

In order to solve equation 50, at the beginning of every time step the value of the iteration counter is set to unity and the residuals are computed at the previous time step. Then the jacobian matrix is computed at the iteration level. Then the equation 50 is solved. With the new difference matrix, the variables is updated and checked for convergence. If the variables have not converged, the iteration counter is incremented and the process is repeated till convergence. A flow diagram is presented in **Fig. 2.3.**

Posing Equations in the Residual Form. We know that both the relative permeability and capillary pressures are a function of water saturation. Therefore the coefficient "a" is not a constant but is a spatial variable of water saturation. Therefore, we can use the equation:

$$k_{ro}^{n+1} = k_{ro}^{k} + \left(\frac{k_{ro}^{n+1} - k_{ro}^{k}}{S_w^{n+1} - S_w^{k}}\right)(S_w^{n+1} - S_w^{k}) \tag{51}$$

$$= k_{ro}^{k} + k_{ro}'\,(Sw^{n+1} - Sw^{k}) \tag{52}$$

Where

n	Time step counter
k	Iteration counter
`	Prime operator

Therefore the symmetric coefficient can be written as:

$$a_{oE}^{n+1} = a_{oE}^{k} + a_{oE}'\,(Sw^{n+1} - Sw^{k}) \tag{53}$$

Similarly:

$$a_{wE}^{n+1} = a_{wE}^{k} + a_{wE}'(Sw^{n+1} - Sw^{k}) \tag{54}$$

Therefore equation 45 can be written as (ignoring gravity):

$$\begin{aligned}&\left[a_{oWi}^{k} + a_{oW}'_{i}(S_{w}^{n+1}{}_{i} - S_{wi}^{k})\right]\left(p_{i\text{-}1}^{n+1} - p_{i}^{n+1}\right) + + \left[a_{oEi}^{k} + a_{oE}'_{i}(S_{w}^{n+1}{}_{i} - S_{wi}^{k})\right]\left(p_{i+1}^{n+1} - p_{i}^{n+1}\right)\\ &+\left[a_{oSj}^{k} + a_{oS}'_{j}(S_{w}^{n+1}{}_{j} - S_{wi}^{k})\right]\left(p_{j\text{-}1}^{n+1} - p_{j}^{n+1}\right) + + \left[a_{oNj}^{k} + a_{oN}'_{j}(S_{w}^{n+1}{}_{j} - S_{wj}^{k})\right]\left(p_{j+1}^{n+1} - p_{j}^{n+1}\right)\end{aligned}$$

$$= -\frac{V_p / B_o}{\Delta t}(S_{wi}{}^{n+1} - S_{wi}^{n}) + q_o + \sum R_\alpha \lambda \left\{Sum^{n-1} e^{-\lambda \Delta t_{Dn}}\right\} \tag{55}$$

Now converting the unknowns to difference terms, we have:

$$S_w^{n+1} = S_w^{k} + S_w^{*} \tag{56}$$

$$p^{n+1} = p^{k} + p^{*} \tag{57}$$

Rewriting equation 55 in terms of these unknowns we have:

$$\begin{aligned}&\left[a_{oWi}^{k} + a_{oW}'_{i} S_{wi}^{*}\right]\left(p_{i\text{-}1}^{k} - p_{i}^{k} + p_{i\text{-}1}^{*} - p_{i}^{*}\right) + \left[a_{oEi}^{k} + a_{oE}'_{i} S_{wi}^{*}\right]\left(p_{i+1}^{k} - p_{i}^{k} + p_{i+1}^{*} - p_{i}^{*}\right)\\ &+\left[a_{oSj}^{k} + a_{oS}'_{j} S_{wj}^{*}\right]\left(p_{j\text{-}1}^{k} - p_{j}^{k} + p_{j+1}^{*} - p_{j}^{*}\right) + \left[a_{oNj}^{k} + a_{oN}'_{j} S_{wj}^{*}\right]\left(p_{j+1}^{k} - p_{j}^{k} + p_{j+1}^{*} - p_{j}^{*}\right)\end{aligned}$$

$$= -\frac{V_p / B_o}{\Delta t}(S_{wi}{}^{k} + S^{*}{}_{wi} - S_{wi}^{n}) + q_o + \sum R_\alpha \lambda \left\{Sum^{n-1} e^{-\lambda \Delta t_{Dn}}\right\} \tag{58}$$

Now consider the first term on the left hand side of equation 58:

$$\begin{aligned}&\left[a_{oWi}^{k} + a_{oW}'_{i} S_{wi}^{*}\right]\left(p_{i\text{-}1}^{k} - p_{i}^{k} + p_{i\text{-}1}^{*} - p_{i}^{*}\right)\\ &= a_{oWi}^{k}(p_{i\text{-}1}^{k} - p_{i}^{k}) + a_{oWi}^{k}(p_{i\text{-}1}^{*} - p_{i}^{*}) + a_{oW}'_{i} S_{wi}^{*}(p_{i\text{-}1}^{*} - p_{i}^{*}) + a_{oW}'_{i} S_{wi}^{*}(p_{i\text{-}1}^{k} - p_{i}^{k})\end{aligned}$$

The third term is a product of two differences, and as the differences are small, the third term can be neglected. Expanding each term in equation 58 and bringing the unknowns to the left hand side, the equation can be rewritten as

$$a^k_{oW_i}(p^*_{i\text{-}1} - p^*_i) + a_{oW}{}'_i\, S^*_{wi}(p^k_{i\text{-}1} - p^k_i) + a^k_{oE_i}(p^*_{i+1} - p^*_i) + a_{oE}{}'_i\, S^*_{wi}(p^k_{i+1} - p^k_i)$$

$$+ a^k_{oS_j}(p^*_{j\text{-}1} - p^*_j) + a_{oS}{}'_j\, S^*_{wj}(p^k_{j\text{-}1} - p^k_j) + a^k_{oN_j}(p^*_{j+1} - p^*_j) + a_{oN}{}'_j\, S^*_{wj}(p^k_{j+1} - p^k_j) + \frac{V_p / B_o}{\Delta t}(S^*{}_w)$$

$$= \begin{array}{l} a^k_{oW_i}(p^k_{i\text{-}1} - p^k_i) + a^k_{oE_i}(p^k_{i+1} - p^k_i) + + a^k_{oS_j}(p^k_{j\text{-}1} - p^k_j) + a^k_{oN_j}(p^k_{j+1} - p^k_j) \\ + \dfrac{V_p / B_o}{\Delta t}(S^k{}_w - S^n{}_w) + q_o + \sum R_\alpha \lambda \{Sum^{n-1} e^{-\lambda \Delta t_{Dn}}\} \end{array} \tag{59}$$

The right hand side of equation 59, which doesn't contain any unknowns can be construed as being the residual. Thus the equation can be written as

$$\vec{R}^k = -\left(\frac{\partial \vec{R}}{\partial x}\right)^k \Delta \vec{x}^{k+1} \tag{60}$$

Where

$$\Delta \vec{X} = \begin{bmatrix} p^* \\ S^*{}_w \\ . \\ . \\ p^* \\ S^*{}_w \end{bmatrix}$$

The jacobian matrix can be computed from the coefficients of individual variables in equation 59. A similar equation for the water phase is

$$a^k_{wW_i}(p^*_{i\text{-}1} - p^*_i) + a_{wW}{}'_i\, S^*_{wi}(p^k_{i\text{-}1} - p^k_i) + a^k_{wE_i}(p^*_{i+1} - p^*_i) + a_{wE}{}'_i\, S^*_{wi}(p^k_{i+1} - p^k_i)$$

$$+ a^k_{wS_j}(p^*_{j\text{-}1} - p^*_j) + a_{wS}{}'_j\, S^*_{wj}(p^k_{j\text{-}1} - p^k_j) + a^k_{wN_j}(p^*_{j+1} - p^*_j) + a_{wN}{}'_j\, S^*_{wj}(p^k_{j+1} - p^k_j) - \frac{V_p / B_o}{\Delta t}(S^*{}_w)$$

$$= \begin{array}{l} a^k_{wW_i}(p^k_{i\text{-}1} - p^k_i) + a^k_{wE_i}(p^k_{i+1} - p^k_i) + + a^k_{wS_j}(p^k_{j\text{-}1} - p^k_j) + a^k_{wN_j}(p^k_{j+1} - p^k_j) \\ - \dfrac{V_p / B_w}{\Delta t}(S^k{}_w - S^n{}_w) + q_w + \sum R_\alpha \lambda \{Sum^{n-1} e^{-\lambda \Delta t_{Dn}}\} \end{array} \tag{61}$$

Numerical Method of Estimating the Jacobian. In order to estimate the jacobian matrix, an alternate method can also be used. Jacobian matrix can be estimated from numerical methods as opposed to analytical methods. Consider equations 59 and 61. The jacobian matrix for equation 59 (only 59 is considered for brevity) can be written as

$$\vec{J} = \begin{bmatrix} \frac{\partial R_1}{\partial p_1^*} & \frac{\partial R_1}{\partial S_{w1}^*} & \cdot & \cdot & \frac{\partial R_1}{\partial p_n^*} & \frac{\partial R_1}{\partial S_{wn}^*} \\ \frac{\partial R_{1w}}{\partial p_1^*} & \frac{\partial R_{1w}}{\partial S_{w1}^*} & \cdot & \cdot & \frac{\partial R_{1w}}{\partial p_n^*} & \frac{\partial R_{1w}}{\partial S_{wn}^*} \\ \cdot & \cdot & \cdot & \cdot & \cdot & \cdot \\ \cdot & \cdot & \cdot & \cdot & \cdot & \cdot \\ \frac{\partial R_n}{\partial p_1^*} & \frac{\partial R_n}{\partial S_{w1}^*} & \cdot & \cdot & \frac{\partial R_n}{\partial p_n^*} & \frac{\partial R_n}{\partial S_{wn}^*} \\ \frac{\partial R_{nw}}{\partial p_1^*} & \frac{\partial R_{nw}}{\partial S_{w1}^*} & \cdot & \cdot & \frac{\partial R_{nw}}{\partial p_n^*} & \frac{\partial R_{nw}}{\partial S_{wn}^*} \end{bmatrix} \tag{62}$$

Consider the term in row 1 and column 1 of the jacobian matrix, by definition, the partial differential can be written as

$$\frac{\partial R_1}{\partial p^*_1} = \frac{Lt}{h \to 0}\left(\frac{R_1(p^*_1 + h) - R_1(p^*_1)}{h}\right) = \frac{Lt}{h \to 0}\left(\frac{R_1(p_1 + h) - R_1(p_1)}{h}\right) \tag{63}$$

The user can specify the value of "h" in the above equation and the limit of the ratio can be approximated as the ratio, since the residual is continuous at zero. Therefore the partial differential can be written as

$$\frac{\partial R_1}{\partial p^*_1} = \left(\frac{R_1(p_1 + h) - R_1(p_1)}{h}\right) \tag{64}$$

The other elements in the jacobian matrix can also be written in that form.

Method of Solution of the System of Equations. To solve the system of equations as posed by equation 60 for both the water and the oil phases, the Gaussian elimination method is proposed. Gaussian elimination is briefly described in this section.

To solve a system of equations as shown below,

$$\begin{cases} a_{11}x_1 + a_{12}x_2 + ...a_{1n}x_n = b_1 \\ a_{21}x_1 + a_{22}x_2 + ...a_{2n}x_n = b_2 \\ \quad . \\ a_{n1}x_1 + a_{n2}x_2 + ...a_{nn}x_n = b_n \end{cases} \tag{65}$$

Gaussian elimination's objective is to rewrite the above equation in the following form

$$\begin{cases} \alpha_{11}x_1 + \alpha_{12}x_2 + ...\alpha_{1n}x_n = \beta_1 \\ \quad \alpha_{22}x_2 + ...\alpha_{2n}x_n = \beta_2 \\ \quad . \\ \quad \alpha_{nn}x_n = \beta_n \end{cases} \tag{66}$$

To obtain this transformation the following matrix rules are applied

1. Interchanging of the order of the equations.
2. Multiplication of any equation by a non-zero number.
3. Addition of any equation with a multiple of any other.

After the system of equations is posed in the form indicated by 66, the value of x_n is first calculated using the last equation of the system, then x_{n-1} and so on till x_1 is calculated.

To effect the above transformation the following method or algorithm is used.

1. Starting with the first equation, divide the equation by a_{11} to get one in the first term.
2. Subtract a_{1i} times the first equation from all the equations below the first equation to make the first term in all those equations zero.
3. Repeat the step for the second equation and so on until the last equation consists of only one term.

2.5 DISCUSSIONS

The imbibition simulator was used to match the recovery and spatial variation of saturation. To validate this simulator two experimental cases were modeled.

- Garg *et al*
- Vivek *et al*

Garg et al. Garg *et al* performed a one-dimensional imbibition experiment and using X-Ray CT, developed scans of saturation across the core at various time steps. So in order to model this experiments, the recovery and saturation distributions are necessary to be modeled. Various petro-physical properties that were used for this model are shown in **Table 2.2.** The relative permeabilities were modeled using Corey's equation as shown below.

$$k_{rw} = k_{rw}^{o} S^{n}{}_{w} \tag{67}$$

The capillary pressures were modeled using the following equation.

$$P_c = P_c^{0} \ln S_w \tag{68}$$

By varying the relative permeability "n", "krw^{0}" and "P_c^{0}" values, a match between the lab and simulated data were obtained. **Fig. 2.4** shows the effect of gravity on imbibition response. The effect of gravity is not significant since the height of the core is small. **Fig. 2.5** shows the magnitude of the capillary and gravity forces. The effect of relative permeability exponent "n" can be seen in **Fig. 2.6**. Similarly the effect of end point capillary pressure can be seen in **Fig. 2.7**. By trial and error the recovery and saturation distributions were matched as shown in **Figs. 2.8** and **Fig. 2.9.** The parameters used to obtain this match are shown in **Table 2.3.**

Vivek *et al.* Vivek *et al* performed two dimensional imbibition experiments with oil-saturated core completely surrounded by water. Since X-Ray CT was not used to model the saturation distribution, only the recovery of oil could be matched. The oil recovery

match is as shown in **Fig. 2.10.** The core petro-physical properties are as provided in **Table 2.4**. The capillary pressure values and relative permeability values obtained for this match are tabulated in **Tables 2.5** and **6**.

By modeling these two imbibition experiments successfully, the veracity of the simulator is verified.

Dual Porosity Simulation. A dual porosity simulator was developed using empirical transfer functions, as shown in the previous section, and the results from some test cases were verified using ECLIPSE^{TM}. ECLIPSE models used the conventional transfer functions, i.e, they assumed that the transfer of fluids was governed by the difference in pressures of the matrix and the fracture media.
In order to perform numerical simulation, the imbibition simulator was run for a matrix block and empirical parameters were estimated using curve-fitting techniques. Then these were input into the dual porosity simulator and compared with ECLIPSE under different production schemes.

One Dimensional Model. Using ECLIPSE the pressure and water saturation were compared for a 10x1x1 grid, 1 well model. The well was produced at the low production rate of 1 bbl/day. **Fig. 2.11** presents the fracture pressure and water saturation results for this model compared with ECLIPSE.A good match can be seen between the two models. **Fig. 2.12** presents the comparison with a very high production rate of 10 bbls/day. The empirical model simulator reports the pressure and saturation to be less than one percent off when compared to ECLIPSE.

Dual Dimensional Model. The same reservoir model was extended to a 10x10x1 grid with one well located at 5x5x1. This well was produced at a high production rate and the pressure and water saturations compared with ECLIPSE. **Figs. 2.13** and **2.14** are the pressure profiles along a line drawn parallel to the X-axis and Y-axis respectively. **Fig. 2.15** shows the material balance error of both oil and water phases for the two dimensional case. The water phase material balance increases initially but becomes

constant after 6 days, but the oil phase material balance error increases with time continuously. This is probably due to the empirical transfer function (**Fig. 2.16**). **Fig. 2.17** shows the fitting of the imbibition recovery data with curve fitting parameters.

Comparison with Sub-Domain Method. Kazemi and Gilman[26] presented a 5 spot water flooding case. From this case, a matrix block was selected and synthetic imbibition experiments were performed. The matrix was initially filled with recoverable oil and completely surrounded by fractures. The fracture spacing was selected in such a manner that the matrix block is of the same size as that of the grid block. Fractures that surround the matrix block were saturated with water and a field size imbibition case was thus created. A graphical representation of this model is shown in **Fig. 2.18.**

This model was simulated using a commercially available simulator (CMG) and also by the developed empirical transfer function, dual porosity simulator. **Fig. 2.19** shows the matrix saturation results from the commercially available simulator and the developed simulator. Sub-Domain method, which is a refinement of dual porosity simulation, was also used for this test case. Sub-domain method reports the matrix saturation slightly less than that of the conventional dual porosity simulation. This is because of matrix block refinement in the case of sub-domain method. In this test case, a 5 level sub-domain method was used, that is, the matrix was divided into five different blocks and the average saturation among these divisions were reported as the matrix saturation.

The empirical transfer function model compares well with both these models. In the initial portion of **Fig. 2.19**, it can be seen that the empirical transfer function's results are within the error tolerances of sub-domain method while offset from the conventional dual porosity results. This is because the conventional transfer functions formulations do not honor the initial time behavior of transfer of fluids[58]. The later time behavior of empirical transfer function model is within acceptable limits of both conventional transfer function model and sub-domain models.

2.6 CONCLUSIONS

The following conclusions can be derived from this study.

1. The Diffusivity equation is sufficient to model imbibition experiments.
2. Imbibition experiments provide us with empirical transfer functions that can be used to model dual porosity simulation.
3. Empirical dual porosity simulation is inherently faster, because the number of unknowns per grid block is reduced to two from four.
4. "Material Balance" is not conserved to the extent of conventional dual porosity formulations.

2.7 REFERENCES

1. Ron Nelson: *Geological Analysis of Naturally Fractured Reservoirs,* second edition, Gulf Professional Publishing, St. Louis (2003).
2. Jaeger, J.S. and Cook, N.G.W.: *Fundamentals of Rock Mechanics*, third edition, Chapman and Hall Ltd., New York City (1979).
3. Aguilera, R.: *Naturally Fractured Reservoirs*, second edition, PennWell Pub. Co., Tulsa (1995).
4. Reiss, L.H.: *The Reservoir Engineering Aspects of Fractured Reservoirs*, Golf. Pub. Co., Houston (1980).
5. van Golf-Racht, T.D.: *Fundamentals of Fractured Reservoir Engineering*, Elsevier Scientific Pub. Co., Amsterdam (1982).
6. Nelson, R.A.: *Geologic Analysis of Naturally Fractured Reservoirs*, Golf. Pub. Co., Houston (1985).
7. *Rock Fractures and Fluid Flow: Contemporary Understanding and Applications*, Committee on Fracture Characterization and Fluid Flow, National Academy Press, Washington, D.C. (1996).
8. Livak, B.L.: "Simulation and Characterization of Naturally Fractured Reservoirs," Prod., Reservoir Characterization Technical Conference, Dallas, Academic Press, New York City (1985).
9. Gilman, J.R. and Kazemi, H.: "Improved Calculations for Viscous and Gravity Displacement in Matrix Blocks in Dual-Porosity Simulators," *JPT* (Jan. 1988) 60-70.
10. Labastie, A.: "Capillary Continuity between Blocks of a Fractured Reservoir," paper SPE 20515 presented at the SPE Annual Technical Conference and Exhibition, New Orleans, Sept. 23-26, 1990.
11. Tan, J.C.T. and Firoozabadi, A.: "Dual-Porosity Simulation Incorporating Reinfiltration and Capillary Continuity Concepts: Part I – Single Gridcell," paper SPE 29113 presented at the SPE Reservoir Simulation Symposium, San Antonio, Feb. 12-15, 1995.

12. Firoozabadi, A. and Ishimoto, K: "Theory of Reinfiltration in Fractured Porous Media: Part I – One-Dimensional Model," paper SPE 21796 presented at the Western Regional Meeting, Long Beach, California, March 20-22, 1991.
13. Barkve, T. and Firoozabadi, A.: "Analysis of Reinfiltration in Fractured Porous Media," paper SPE 24900 presented at the Annual Technical Conference and Exhibition, Washington, D.C., Oct. 4-7, 1992.
14. Bourbiaux, B. and Kalaydjian, F.J.: "Experimental Study of Cocurrent and Countercurrent Flows in Natural Porous Media," *SPERE* (Aug. 1990) 361-368.
15. Pooladi-Darvish, M. and Firoozabadi, A.: "Cocurrent and Countercurrent Imbibition in a Water-Wet Matrix Block," *SPEJ* (March 2000) 3-11.
16. McNaughton, D.A., and F.A. Garb. "Finding and evaluating Petroleum Accumulations in Fractured Reservoir Rock." *Exploration and Economics of the Petroleum Industry*, Vol. 13. Matthew Bender & Company Inc. (1975).
17. Hohlt, R.B. "The Nature of Origin of Limestone Porosity", Colorado School of Mines Quarterly (1948) No. 4.
18. Lawn, B. and Wilshaw, R. "Indentation Fracture: Principles and Applications", J. Mater. Sci. (UK) **10** (June 1975) 1049-81.
19. Agarwal, B., Hermansen, H., Sylte, J.E., and Thomas, L.K.: "Reservoir Characterization of Ekofisk Field: A Giant, Fractured Chalk Reservoir in the Norwegian North Sea – History Match," *SPEREE* (Dec. 2000), 534-543.
20. Barenblatt, G.I., Zheltov, I.P., and Kochina, I.N.: "Basic Concepts in the Theory of Seepage of Homogenous Liquids in Fissured Rocks (Strata)," *J. Appl. Math. Mech.* (1960) 24, 1286-1303.
21. Warren, J.E. and Root, P.J.: "The Behavior of Naturally Fractured Reservoirs," *SPEJ* (Sep. 1963) 245-255.
22. Kazemi, H.: "Pressure Transient Analysis of Naturally Fractured Reservoirs with Uniform Fracture Distribution," *SPEJ* (Dec. 1969) 451-462; *Trans*., AIME, **246**.
23. Abdassah, D. and Ershaghi, I.: "Triple-Porosity Systems for Representing Naturally Fractured Reservoirs," *SPEFE* (April 1986) 113-127.

24. Aronofsky, J.S., Masse, L., and Natanson, S.G.: "A Model for the Mechanism of Oil Recovery from the Porous Matrix Due to Water Invasion in Fractured Reservoirs," *Trans.*, AIME (1958) **213**, 17-19.
25. de Swaan, A.: "A Theory of Waterflooding in Fractured Reservoirs," *SPEJ* (April 1978) 117-122; *Trans.*, AIME, **265**.
26. Kazemi, H., Gilman, J.R., and Elsharkawy, A.M.: "Analytical and Numerical Solution of Oil Recovery From Fractured Reservoirs With Empirical Transfer Functions," *SPERE* (May 1992) 219-227.
27. Ries and Cil
28. Civan, F.: "Waterflooding of Naturally Fractured Reservoirs: An Efficient Simulation Approach," paper SPE 25449 presented at the Production Operations Symposium, Oklahoma City, March 21-23, 1993.
29. Gupta, A. and Civan, F.: "An Improved Model for Laboratory Measurement of Matrix to Fracture Transfer Function Parameters in Immiscible Displacement," paper SPE 28929 presented at the SPE Annual Technical Conference and Exhibition, New Orleans, Sep. 25-28, 1994.
30. Civan, F.: "Quadrature Solution for Waterflooding of Naturally Fractured Reservoirs," *SPEREE* (April 1998) 141-147.
31. Rapoport, L.A.: "Scaling Laws for Use in Design and Operation of Water/Oil Flow Models," *Trans*., AIME (1955) 204, 143.
32. Mattax, C.C. and Kyte, J.R.: "Imbibition Oil Recovery from Fractured, Water-Drive Reservoirs," *SPEJ* (June 1962) 177-184; *Trans.*, AIME, **225**.
33. Du Prey, E. L.: "Gravity and Capillary Effects on Imbibition in Porous Media" *Soc. Pet. Eng. J.* (June, 1978) 195-206.
34. Ma, S., X. Zhang, and N.R. Morrow: "Influence of Fluid Viscosity on Mass, Transfer Between Rock Matrix and Fractures," paper presented at the 1995 Annual Technical Meeting of The Petroleum Society of CIM in Banff, Alberta, Canada, May 14-17.
35. Bourbiaux, B. and Kalaydjian, F.J.: "Experimental Study of Cocurrent and Countercurrent Flows in Natural Porous Media," *SPERE* (Aug. 1990) 361-368.

36. Peñuela-Pineda, G.: "Modeling Interporosity Flow For Improved Simulation Of Naturally Fractured Reservoirs," Ph.D. thesis (2002), University of Oklahoma, Norman, OK.
37. Thomas, L.K., Dixon, T.N., and Pierson, R.G.: "Fractured Reservoir Simulation," *SPEJ* (Feb.1983) 42-54.
38. Coats, K.H.: "Implicit Compositional Simulation of Single-Porosity and Dual-Porosity Reservoirs," paper SPE 18427 presented at the SPE Reservoir Simulation Symposium, Houston, Feb. 6-8, 1989.
39. Gilman, J.R. and Kazemi, H.: "Improvements in Simulation of Naturally Fractured Reservoirs," *SPEJ* (Aug. 1983) 695-707.
40. Lim, K.T. and Aziz, K.: "Matrix-Fracture Transfer Shape Factors for Dual-Porosity Simulators," *J. Pet. Sci. and Eng.* (1995) 13, 169-178.
41. Quintard, M. and Whitaker, S.: "Transport in Chemically and Mechanically Heterogeneous Porous Media," *Adv. in Water Res*., (1996) **19** (1), 29-60.
42. Noetinger, B. and Estebenet, T.: "Application of Random Walk Methods on Unstructured Grid to Up-Scale Fractured Reservoirs," paper presented at the 1998 European Conference on Mathematics of Oil Recovery, Peebles, Scotland, Sep 8-11.
43. Chen, J., M,A, Miller, and K. Sepehrnoori: "Theoretical Investigation of Countercument Imbibition in Fractured Reservoir Matrix Blocks," paper SPE 29141 presented at 1995 SPE Symposium on Reservoir Simulation, San Antonio, TX, Feb. 12-15.
44. Hemandez J.C. and C.P. Resales: "Imbibition as a Dispersion Process," paper SPE 23748 presented at the 1992 SPE Latin American Petroleum Engineering Conference, Caracas, Venezuela, March 8-11.
45. Hayashi, J.A. and C.P. Resales: "Visual Investigation of Imbibition Process,", paper SPE 23745 presented at the 1992 SPE Latin American Petroleum Engineering Conference, Caracas, Venezuela, March 8-11.
46. Najurieta, H.L.: "A Theory for Pressure Transient Analysis in Naturally Fractured Reservoirs," *JPT* (July 1980) 1241-1250.

47. Siddiqui, S., Hicks, P.J., Grader, A.S: "Verification of Buckley-Leverett Three Phase Theory Using Computerized Tomography", *J. Pet. Sci. and Engg.* 15 (1996) 1-21.
48. Houndsfield, G.N: "A Method of and Apparatus for Examining a Body by Radiation Such as X- or Gamma-Radiation," Br. Patent No. 1,283,915.
49. Hunt, P.K., Engler, P. and Bajsarowicz, C.: "Computerized Tomography as a Core Analysis Tool: Applications, Instrument Evaluation and Image Improvement Techniques", *Soc. Pet. Eng. J., Formation Evaluation* (Sep. 1988), 1203-1210.
50. Hicks, P.J., Deans, H.A., and Narayanan, K.: "Experimental Measurement of the Distribution of the Residual Oil Saturations in Heterogeneous Carbonate Cores Using X-Ray Computerized Tomography,", paper CIM/SPE 9068 presented at the 1990 International Technical Meeting, Calgary, Alberta, June 10-13.
51. Peters, E.J. and Afzal, N.: "Characterization of Heterogeneities in Permeable Media with Computerized Tomography," *Soc. Pet. Eng. J.* 7: 283-296.
52. Moss, R.M. et al: "Direct Measurement of the Constituent Properties in a Dual Porosity Matrix," presented at the 1990 SCA Ann. Tech. Conf., Houston, TX, Aug. 2-3.
53. Wang, S.Y., et al: "Computer Assisted Tomography for the Observation of Oil Displacement in Porous Media," *Soc. Pet. Eng. J.* (Feb. 1984), 53-55.
54. Vinegar, H. J., and Wellington, S.L.: "Tomographic Imaging of Three-Phase Flow Experiments," Rev. Sci. Instrum. (Jan. 1987), 96-107.
55. Withjack, E.M.: "Computed Tomography for Rock-Property Determination and Fluid-Flow Visualization," *Soc. Pet. Eng. J.* (Dec. 1988), 696-704.
56. Toronyi, R. M. and Forouq Ali, S. M.: " Determining Interblock Transmissibility in Reservoir Simulators," *J. Petrol. Tech.,* **26,** No. 1, pp. 77-78.
57. Raithby, G. D.: "A Critical Evaluation of Upstream Differencing Applied to Problems Involving Fluid Flow," *Comp. Methd. In Appl. Mech. And Eng.,* **9,** No.1, pp. 75-103.
58. Aziz, K. and Lim, K.T.: "Matrix-Fracture Transfer Shape Factors for Dual Porosity Simulators," *J. Pet. Sci. and Eng.* **13** (1995) 169-178.

Table 2.1—Shape Factors as reported by Penula-Pineda

Mathematical Approximations	Slab Geometry	**Square Geometry**	**Cube Geometry**
Warren And Root	12	32	60
Kazemi et al	4	8	12
Thomas et al[37]	-	-	25
Coats[38]	8	16	24
Kazemi and Gilman[39]	-	-	29.6
Limm and Aziz[40]	9.9	19.7	29.6
Quintard and Whitaker[41]	12	28.4	49.6
Noetinger et al[42]	11.5	27.1	-
Bourbiaux et al	-	20	-

Table 2.2—Modeled Garg et al core properties.

Property	**Value**	**Units**
Number of grids blocks in X-Direction	1	-
Number of grids blocks in Y-Direction	1	-
Number of grids blocks in Z-Direction	11	-
Grid Block Dimension X-Direction	4.83	cm
Grid Block Dimension Y-Direction	4.83	cm
Grid Block Dimension Z-Direction	0.67	cm
Density of Oil	0.0006	Lb/cu.ft
Density of Water	62.4	Lb/cu.ft
Permeability X-Direction	300	md
Permeability Z-Direction	300	md
Porosity	0.22	-
Initial Water Saturation	10*0.1, 1.0	-
Boundary Condition	Bottom Most	-

Table 2.3—Parameters for match of imbibition response (Garg et al).

Property	Value	Units
Relative Permeability Exponent	8	-
End Point Relative Permeability	0.045	-
End Point Capillary Pressure	40	psi

Table 2.4—Properties of the core for numerical simulation (Vivek et al)

Property	Value	Units
Number of grids blocks in X-Direction	12	-
Number of grids blocks in Y-Direction	1	-
Number of grids blocks in Z-Direction	12	-
Grid Block Dimension X-Direction	0.3130493	cm
Grid Block Dimension Y-Direction	3.19214817	cm
Grid Block Dimension Z-Direction	0.4621	cm
Density of Oil	48.0	Lb/cu.ft
Density of Water	62.4	Lb/cu.ft
Permeability X-Direction	68	md
Permeability Z-Direction	68	md
Porosity	0. 2092	-
Initial Water Saturation	12*1,10*(1,10*0.46,1), 12*1	-
Boundary Condition	All Sides	-

Table 2.5—Capillary Pressure obtained from the match.

Water Saturation (Fraction)	**Capillary Pressure (psi)**
0.14	2.0
0.2	1.71
0.4	0.91
0.5	0.653
0.6	0.518
0.635	0.46
0.76	0.11
0.8	0.1

Table 2.6—Relative Permeability obtained for the match.

Water Saturation	**Water Relative Permeability**	**Oil Relative Permeability**
0.0	0.33	0.
0.2	0.22	0.15
0.4	0.18	0.37
0.5	0.1	0.4
0.635	0.	0.44
0.76	0.	0.44
0.8	0.	0.44

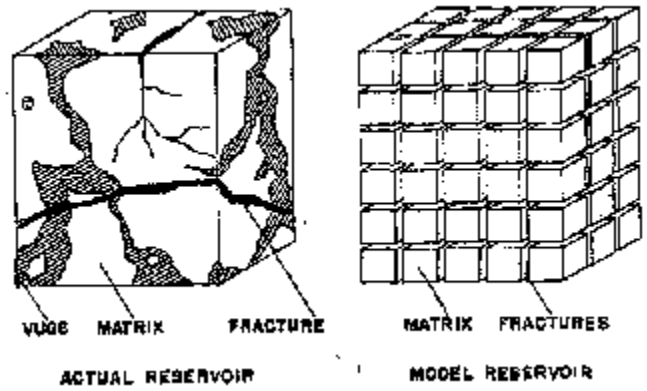

Fig. 2.1— (a) Actual Reservoir (b) Idealized Reservoir.

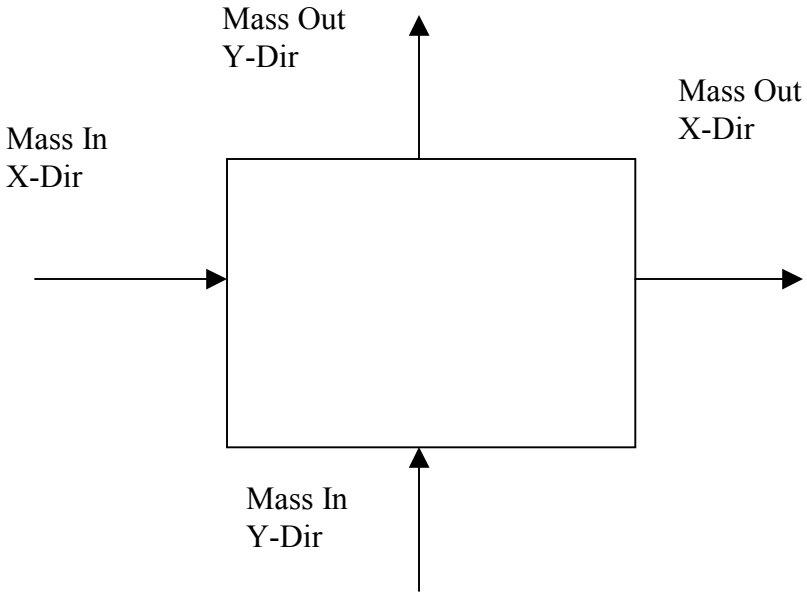

Fig. 2.2—Conservation of mass in a control volume

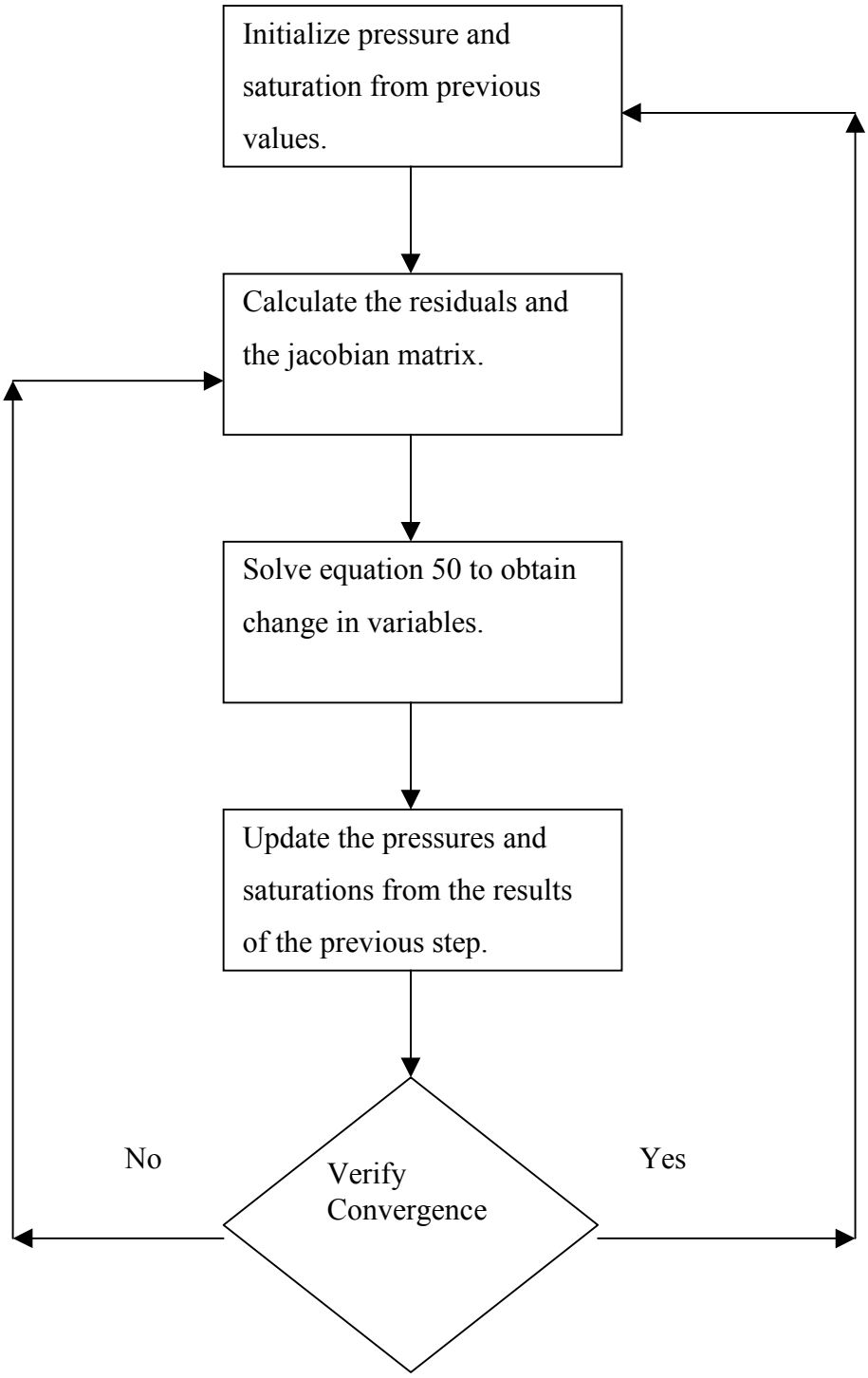

Fig. 2.3—Flow Chart for Newton-Raphson's method of solution.

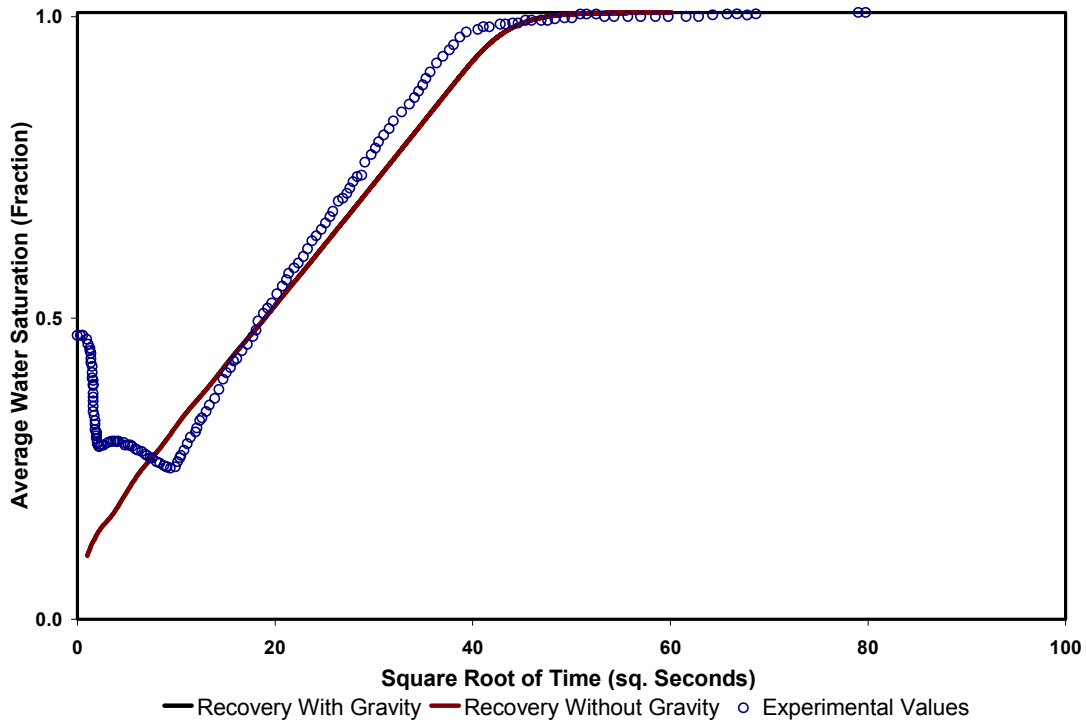

Fig. 4—Effect of Gravity on Imbibition Response

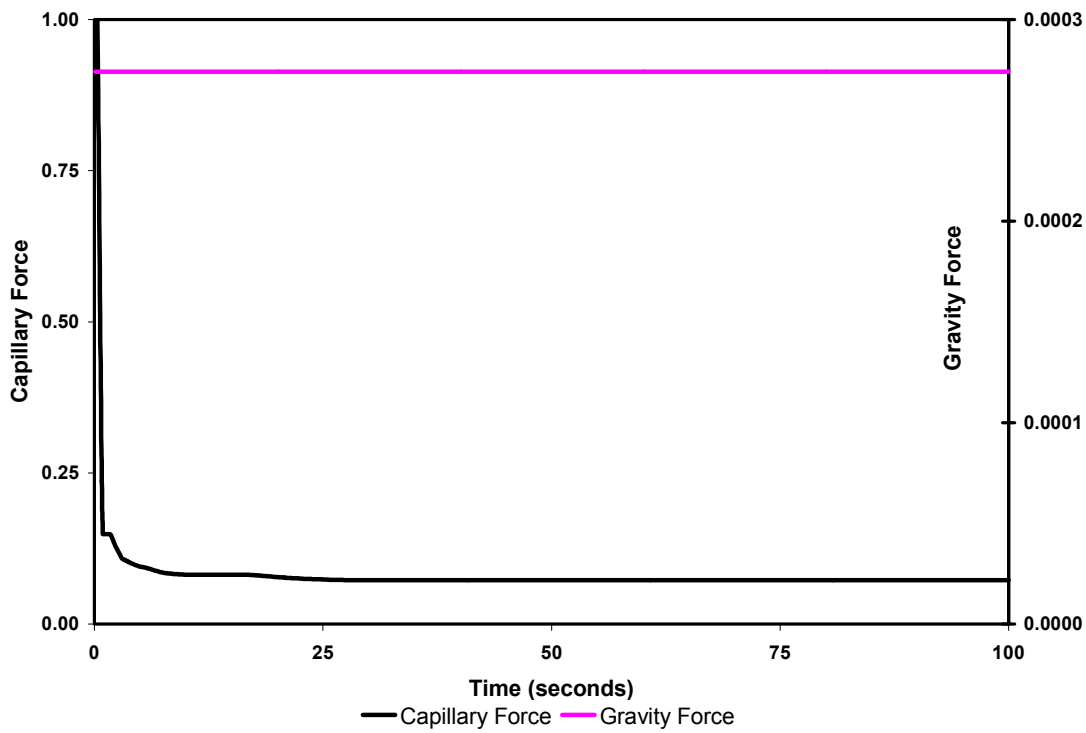

Fig. 5—Gravity and capillary forces as a function of time during imbibition.

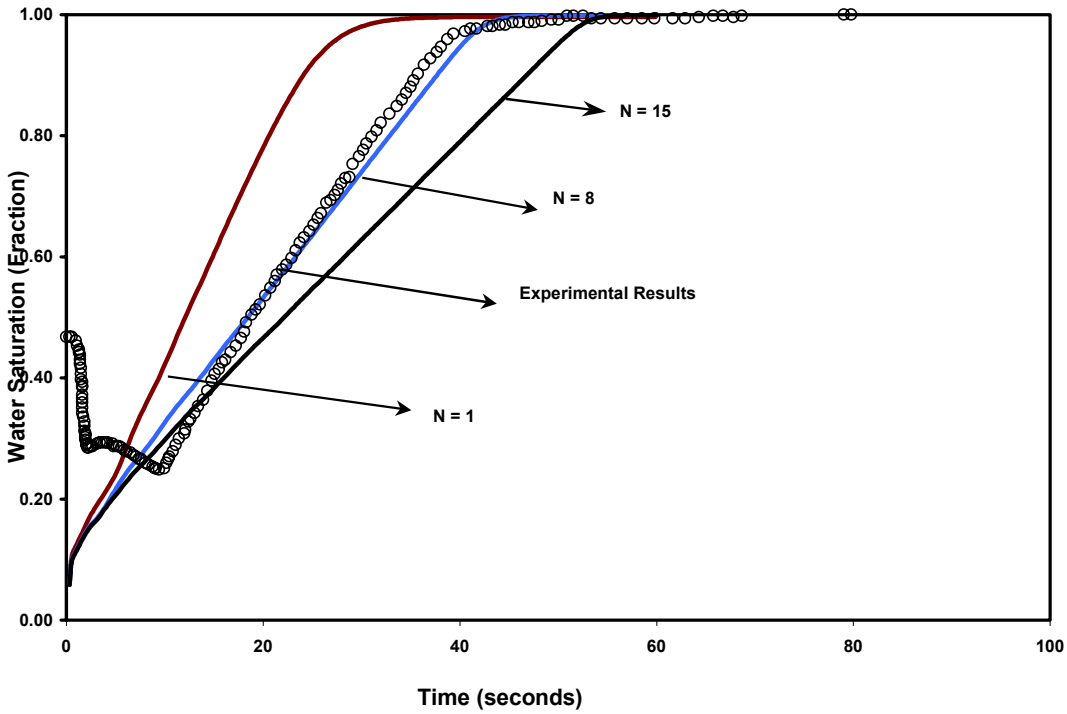

Fig. 6 —Effect of Relative Permeability exponent on Imbibition Recovery.

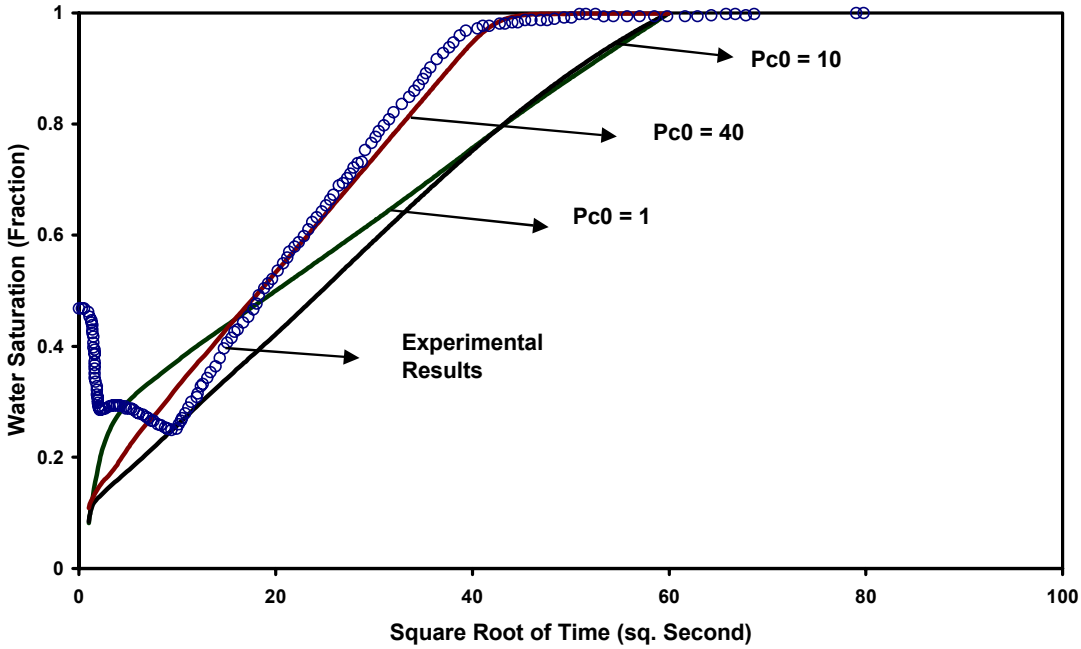

Fig. 7—Effect of end point capillary pressure on imbibition response.

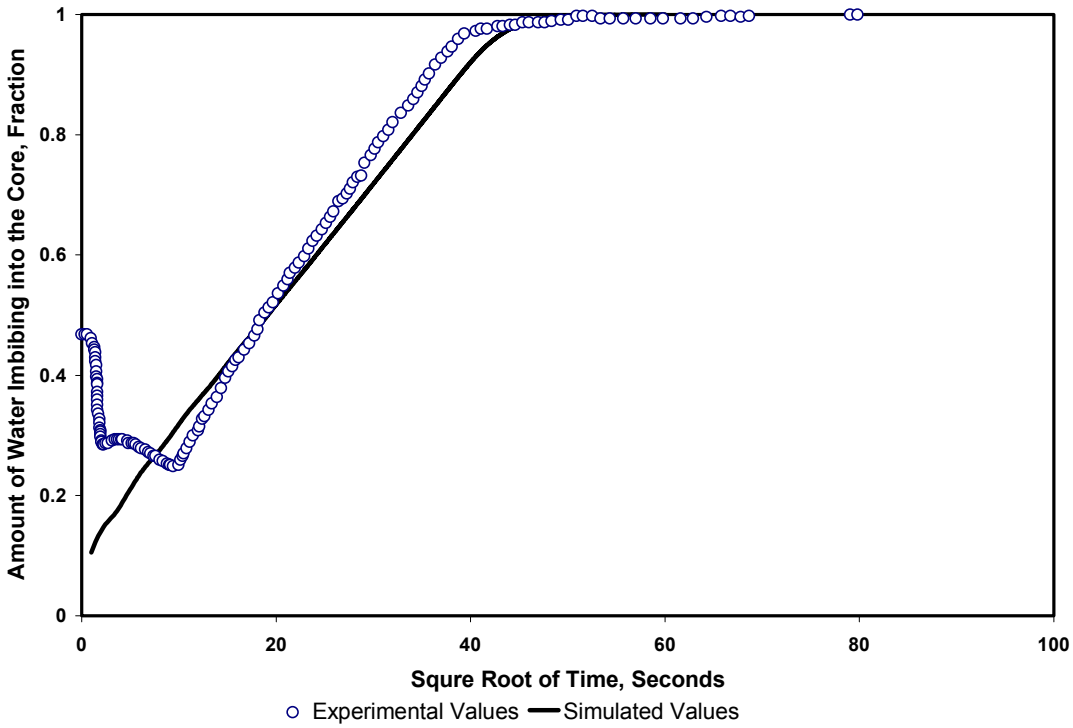

Fig. 8—Match of experimental recovery with simulated recovery.

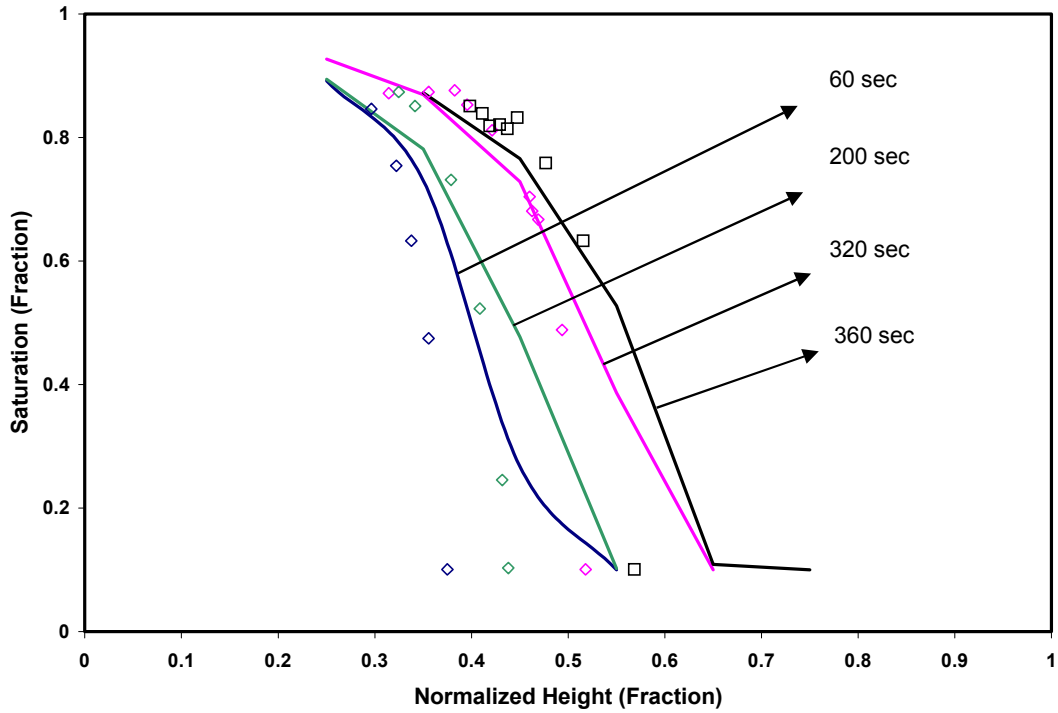

Fig. 9—Match of experimental and simulated saturations.

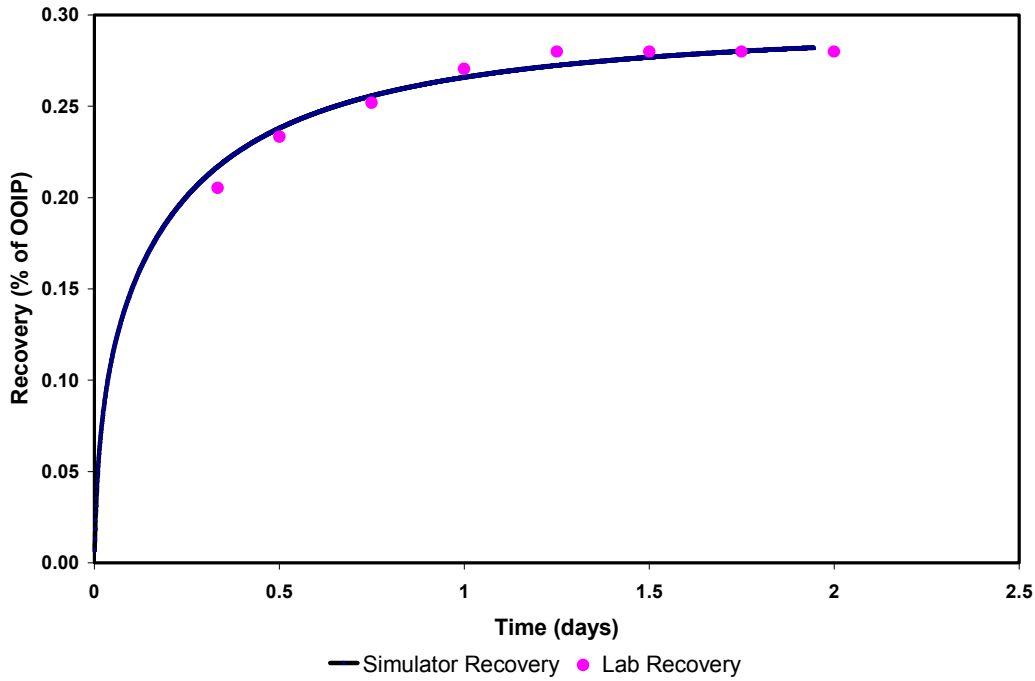

Fig. 10— Match of experimental and simulated recovery.

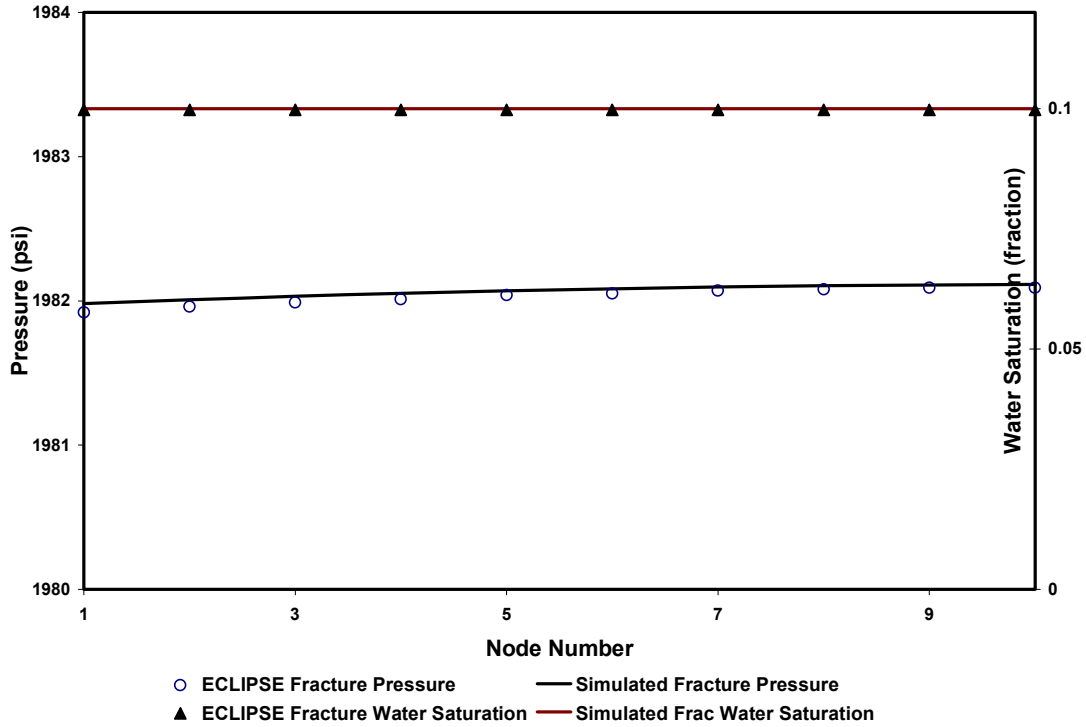

Fig. 11— One dimensional low production rate pressure and water saturation profiles.

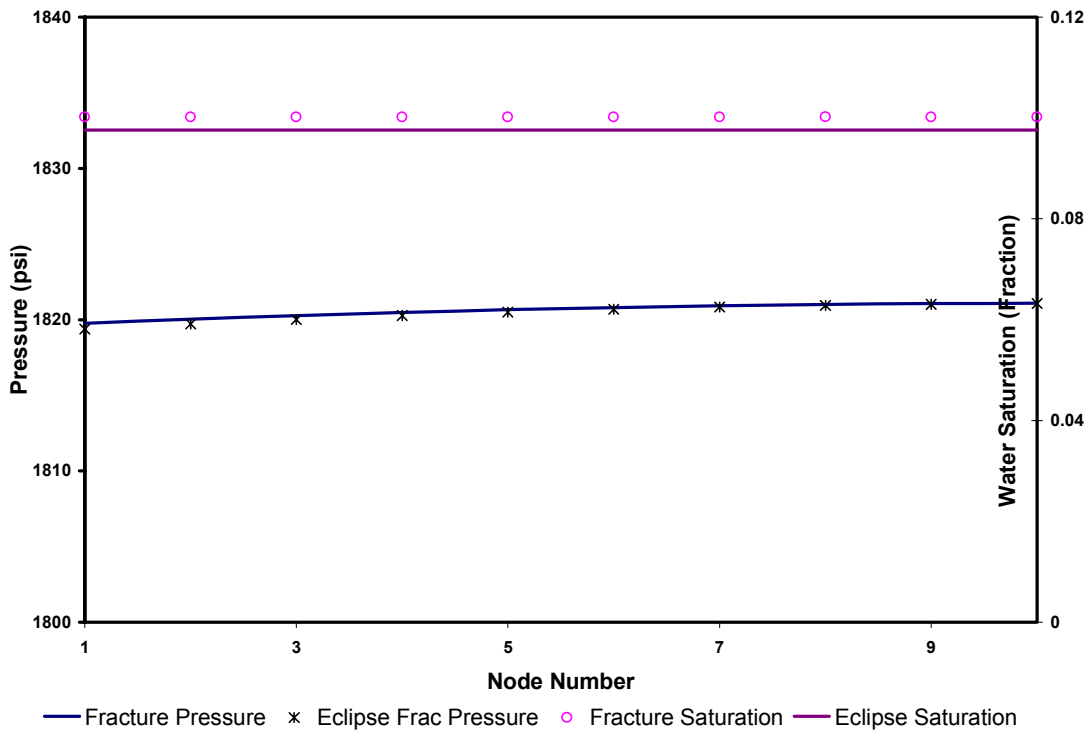

Fig. 12—One-dimensional, high production, pressure and water saturation profiles.

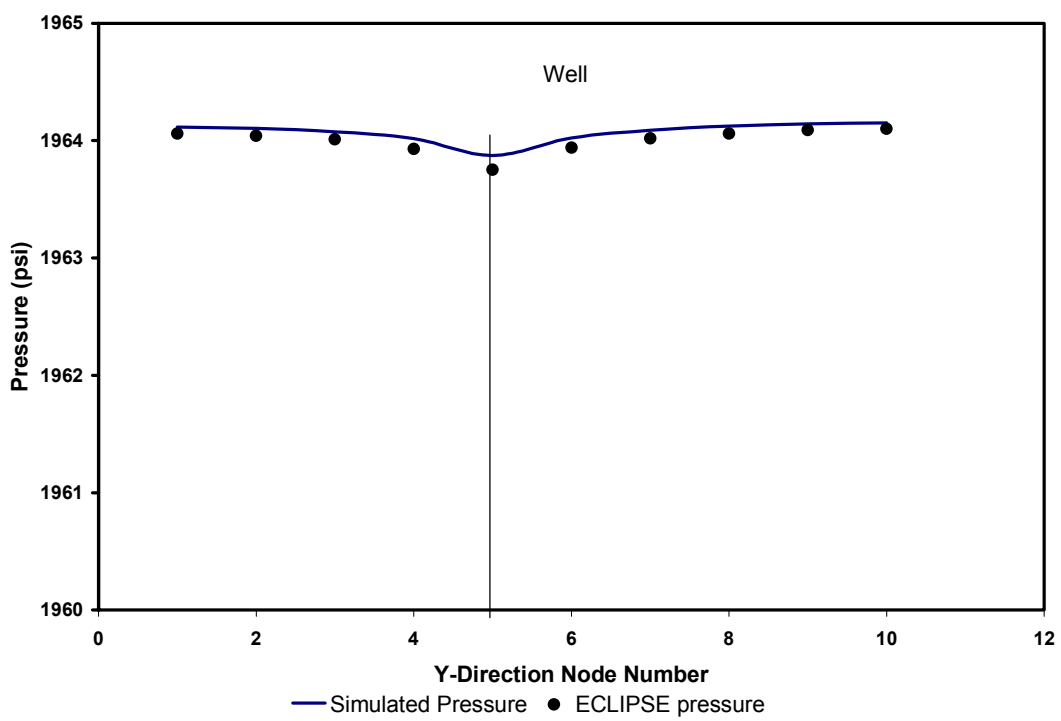

Fig. 13—Pressure Profile along a line parallel to Y axis.

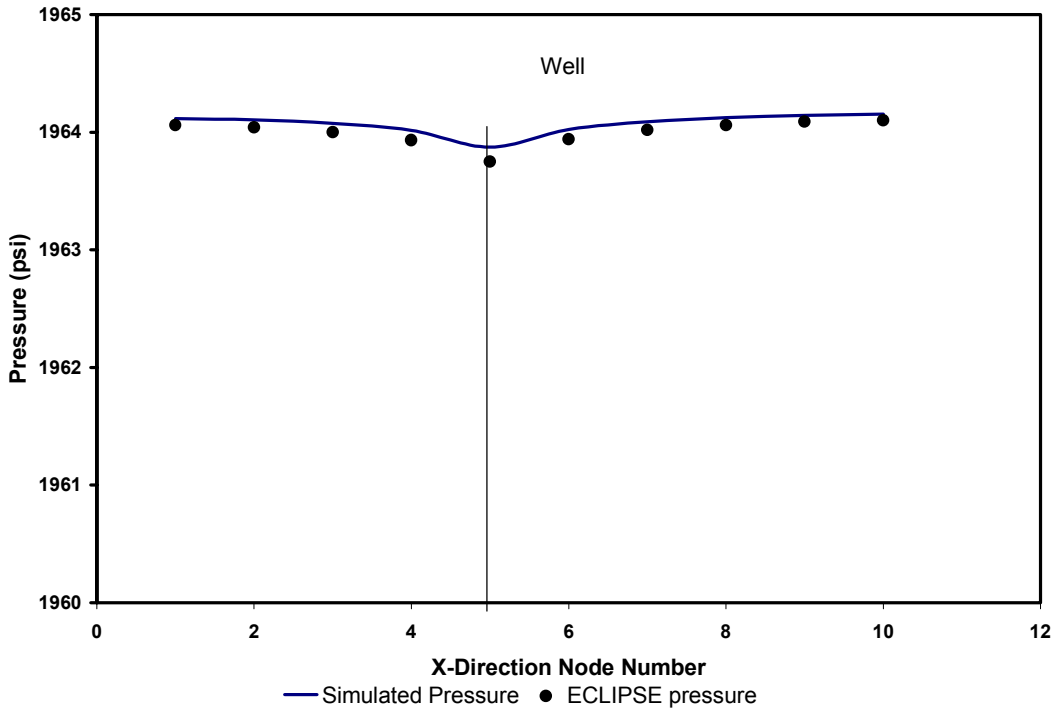

Fig. 14—Pressure profile along a line parallel to X axis.

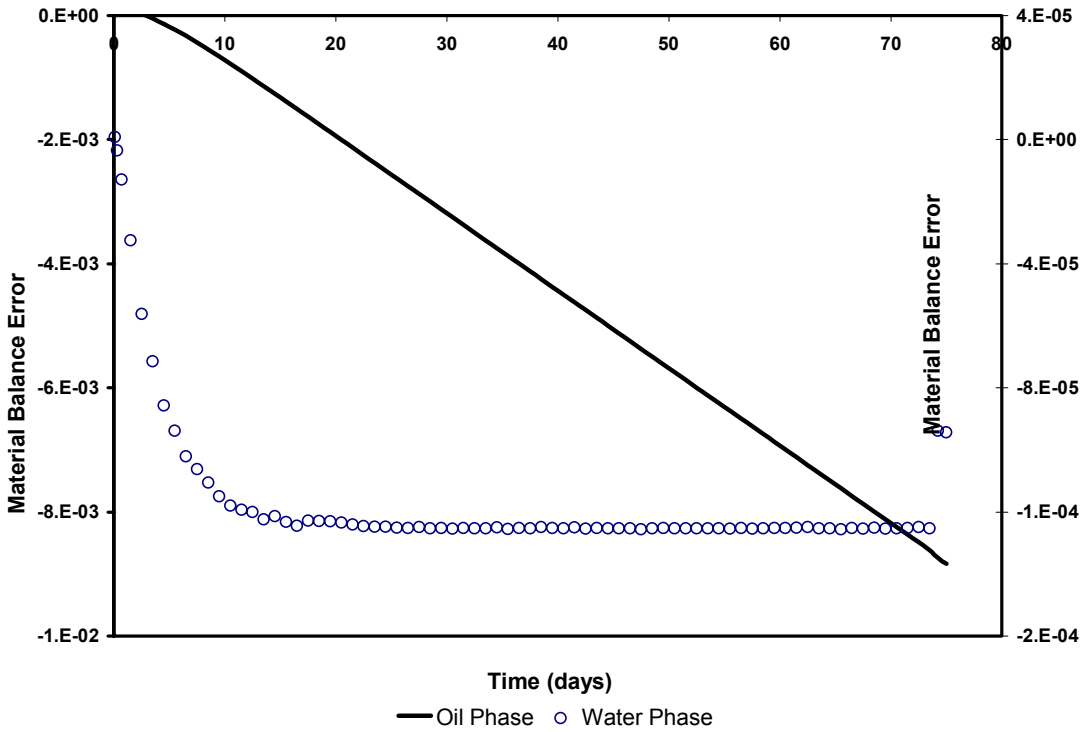

Fig. 15—Material Balance error for the empirical model, two dimensional case.

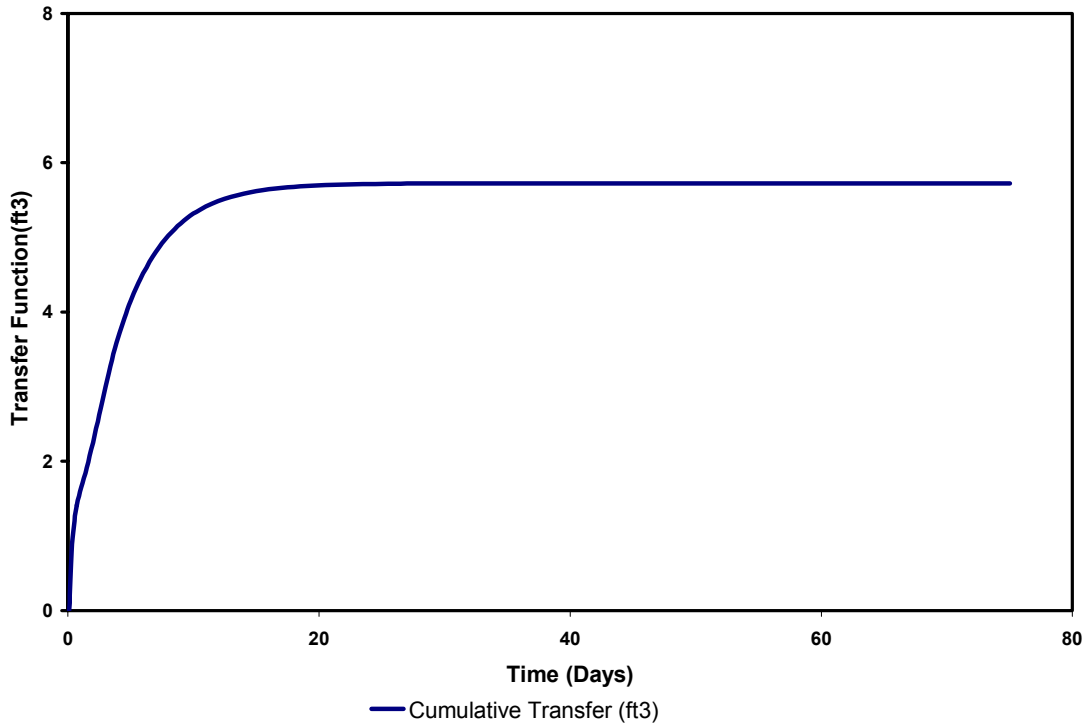

Fig. 16—Empirical transfer function as a function of time

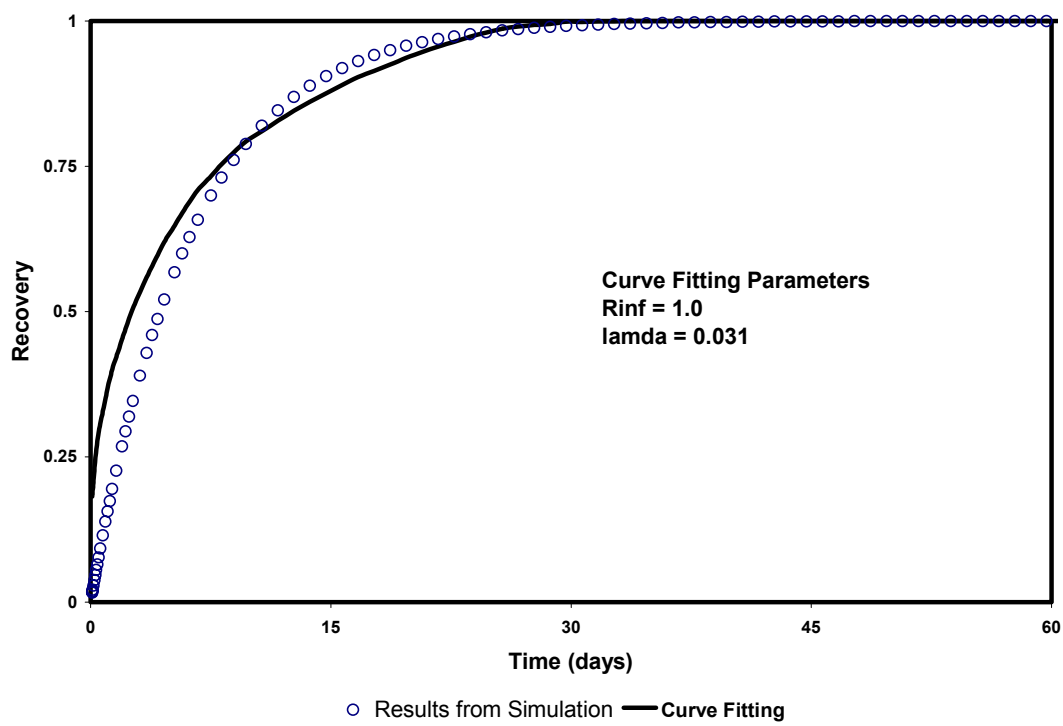

Fig. 17—Imbibition Simulator Response.

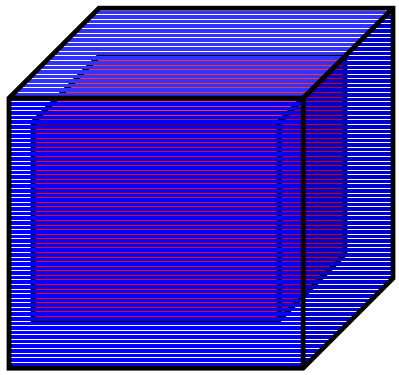

Fig. 18—Representation of the matrix block surrounded by water.

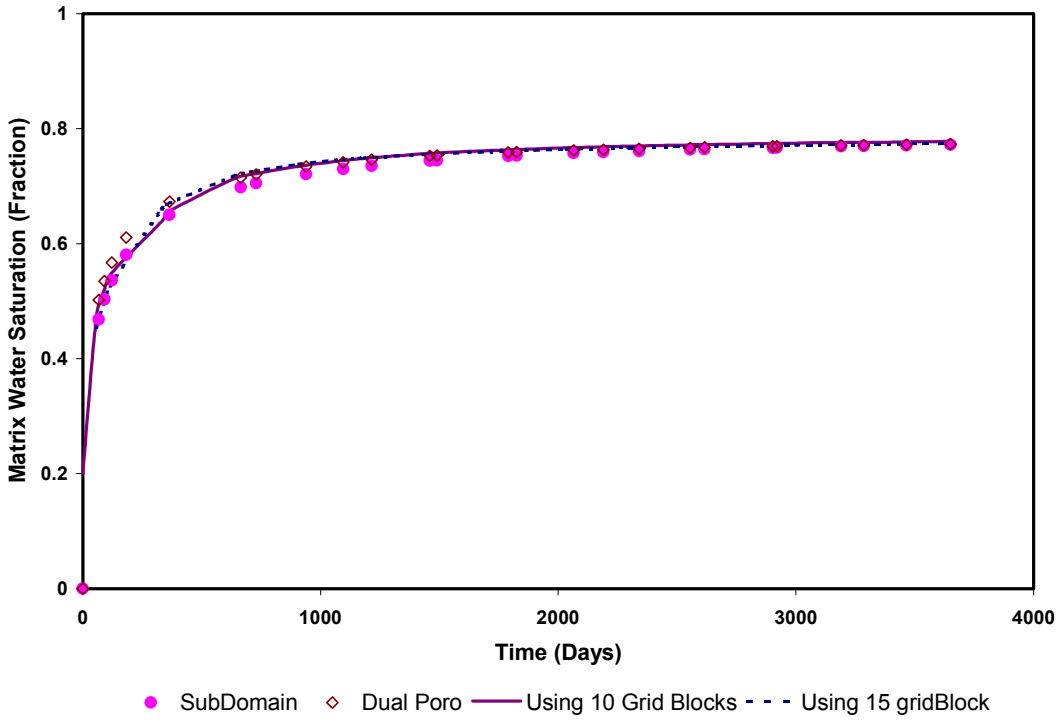

Fig. 18—Comparison of Empirical transfer function with sub-domain method and dual porosity methods.

III. Fracture Aperture Calibration

3.1 Introduction

Flow in fractured media is determined to a large extent by the fracture aperture. Fracture aperture in turn is influenced by a number of factors among which are inclusions and other heterogeneities, stresses, and changes in overburden pressure. The common assumption that the fracture aperture remains constant during the entire life of the reservoir is not valid. It is well known that the permeability decreases with an increase in the overburden pressure (Fatt and Davis[1]; Gray *et al*[2]; Morita *et al*[3]). Putra *et al*[4] also determined experimentally that the overburden pressure causes significant changes in fracture permeability and aperture. Hence, it becomes essential to obtain a fracture aperture distribution under different levels of overburden pressure. Several methods have been used in the past for measurement of fracture aperture. But the common problem associated with these methods is that they are intrusive and hence eliminate the possibility of using the fractured media for fluid flow experiments. Other intrusive techniques are simply inaccurate because of a risk of change in aperture during the course of the experiment. Hence it becomes important to use a non-intrusive, accurate technique to measure fracture aperture. Computerized Aided Tomography (CAT) X-Ray scanning provides a good alternative to the existing techniques to measure fracture aperture. Computerized Tomography is a rapid, non-invasive imaging technique that uses differences in density to image opaque 3D objects[5]. CT scanners work on the principle of generating cross-sectional slices of an object. Multi-angular projections of an object are obtained by concentrating X-Ray beams from a revolving X-Ray tube. These projections are then used to reconstruct the image of the object based on the attenuation of X-Ray

beams[6]. The CT scanner has previously been used effectively to perform a wide variety of experiments which include fluid flow studies, gravity drainage experiments and analysis of miscible floods (Alajmi and Grader[7]; Burger *et al*[7]; Stones *et al*[9]; Hicks *et al*[10]). Keller[11] made use of non-intrusive imaging to obtain aperture calibration curves for granite and sandstone. Using the curve, fracture apertures as small as 35µm can be obtained. A similar technique was followed by He[12] in 1998. Both these techniques use the integrated CT signal to determine fracture aperture. The integration is done by summing up the differences between a minimum rock CT number and the CT numbers pertaining to the fracture.

Thus, in preparation for the fluid flow experiments at A&M, a calibration curve was obtained for Berea sandstone. The technique followed was almost identical to that of Keller's, except for the calculation of the integrated CT signal, which was obtained by summing the CT numbers in the entire area below the set threshold limit.

3.2 Experimental Procedure

A Picker 4th generation CT scanner was used for imaging the core samples. The power, voltage and algorithm requirements were chosen as that of a typical of a sandstone sample. The experimental setup consists of two halves of the same rock sample (Berea Core,) feeler gauges, and core holding equipment. The two halves were polished thoroughly to reduce surface roughness as much as possible. Smoother surfaces ensure that there is a proper match between the halves and hence smaller fractures can be measured. The feeler gauges were then placed between the two flat surfaces to create a fracture of known size. Feeler gauges of size 38 µm, 51 µm, 64 µm, 76 µm, 102 µm, 127

μm, 152 μm, 178 μm, 508 μm, 813 μm were used in the calibration experiment. The sample with the fracture was inserted into a sleeve to avoid artifact effects and held in the core holder. A pressure of 500 psi was applied using a hydraulic jack. Multiple scans were then taken along the length of the core, perpendicular to the longitudinal axis.

3.3 Results and Discussions

Figures 3.1-3.4 show a typical set of scans for the Berea sample with different fracture sizes and their corresponding CT number plots. It can be seen that the CT number at the fracture decreases with an increase in fracture size. The variations in color in the scans are due to different densities in the sample, with the relatively high density rock set to a bright orange color and the lower densities set to green, blue and black in decreasing order of densities. The CT number for a typical Berea sample is about 1600 and that of air is about -1000. The variations in CT numbers are due to the difference in densities. One would normally expect the CT number at the fracture to be the same as that of air, however, this does not happen due to the fact that the CT number at the fracture is influenced by the presence of the rock material around it, a condition termed "oversampling." A plot of CT number versus the pixel number was made with the CT numbers obtained from each scan. Using these, an average CT number plot was obtained to account for minor variations in fracture sizes caused by surface roughness. An example of such a plot is shown in Fig. 3.5. From the plot, a threshold CT number was identified, which essentially is the minimum rock CT number (Fig. 3.6). For calculating the integrated CT signal, the area below the minimum rock CT was divided into triangles and rectangles (Fig. 3.7). Then the area of each individual triangle and rectangle was added

up to find the area under the curve. Fig. 3.8 shows a comparison of the average CT number curves obtained for various fracture sizes. As explained earlier, it can be seen that the CT number decreases with an increase in fracture size. The aperture calibration curve is shown in Fig. 3.9.

3.4 Conclusions

1. The calibration curve shows a linear trend even at very small apertures.
2. Fracture aperture calibration is an important step in determining the effect of fracture size variation in fluid flow experiments.

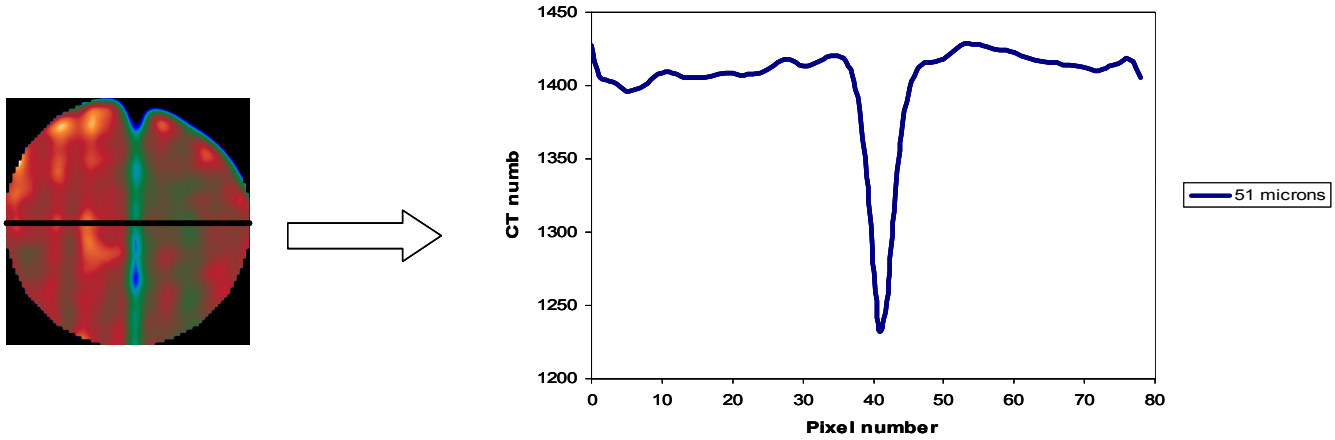

Fig. 3.1— CAT scan for 51 micron fracture size and corresponding CT number plot.

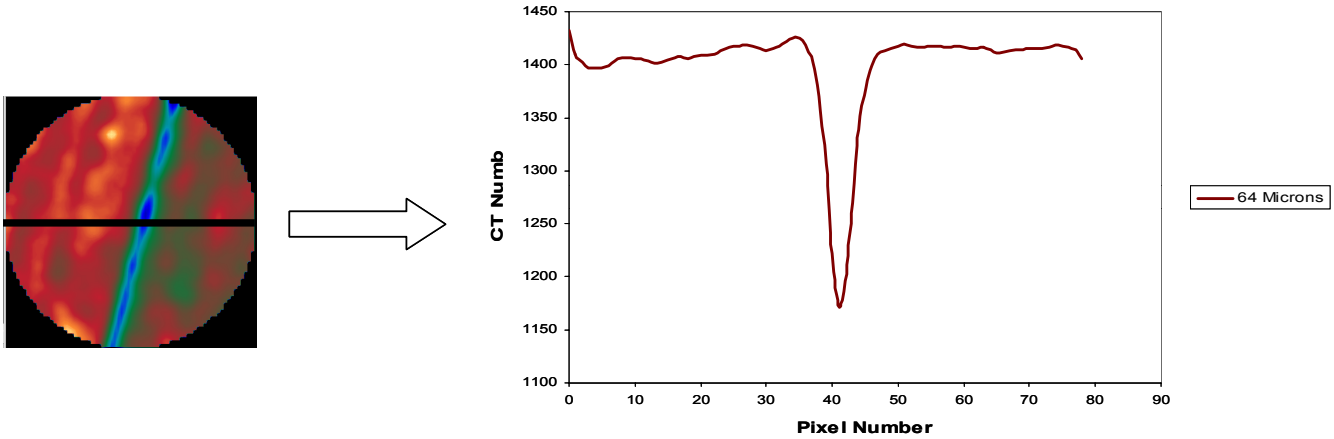

Fig. 3.2— CAT scan for 64 micron fracture size and corresponding CT number plot.

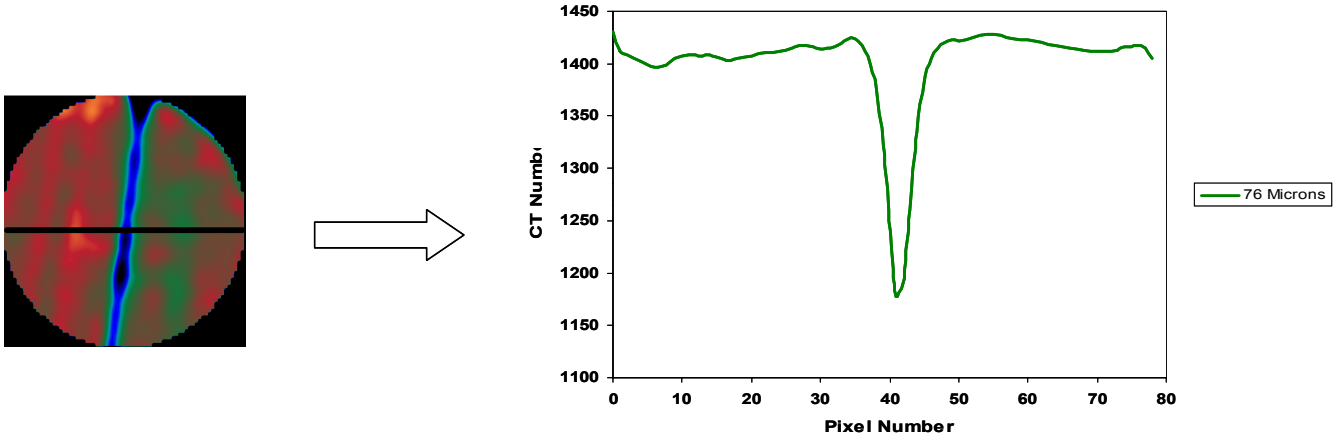

Fig. 3.3— CAT scan for 76 micron fracture size and corresponding CT number plot.

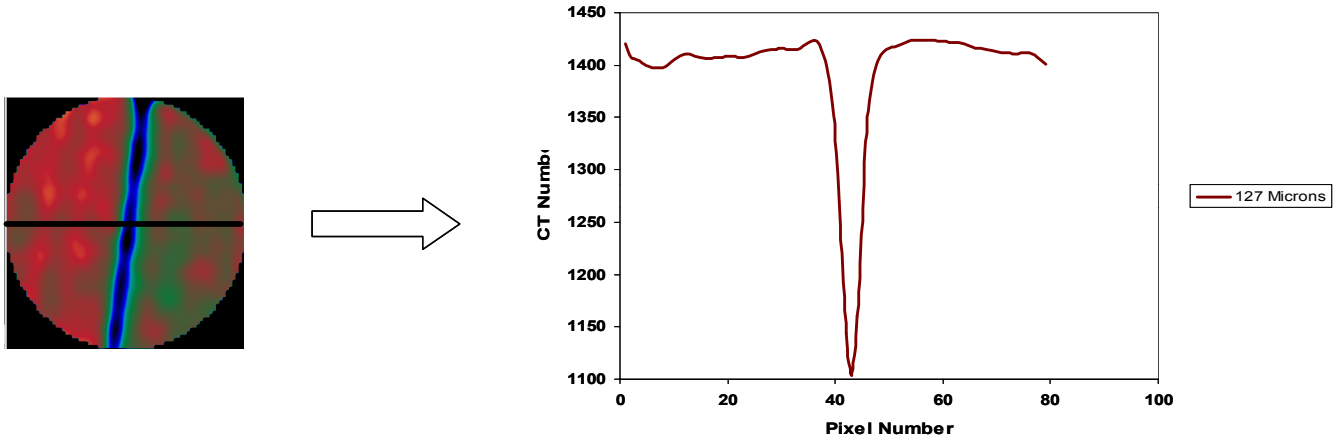

Fig. 3.4— CAT scan for 127 micron fracture size and corresponding CT number plot.

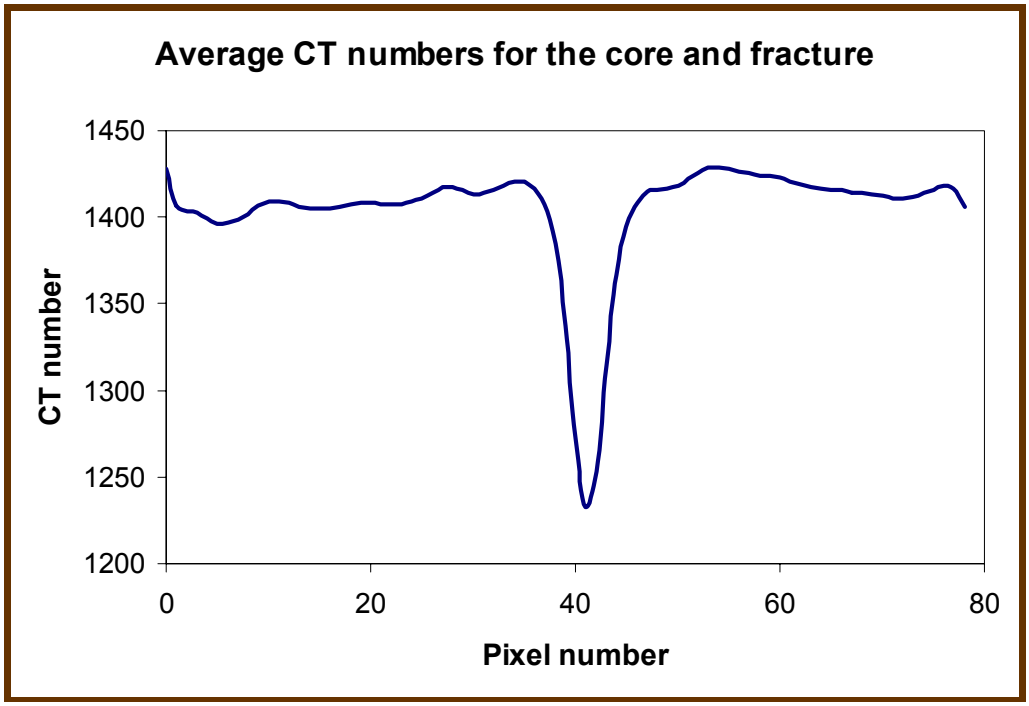

Fig. 3.5—Average CT number plot.

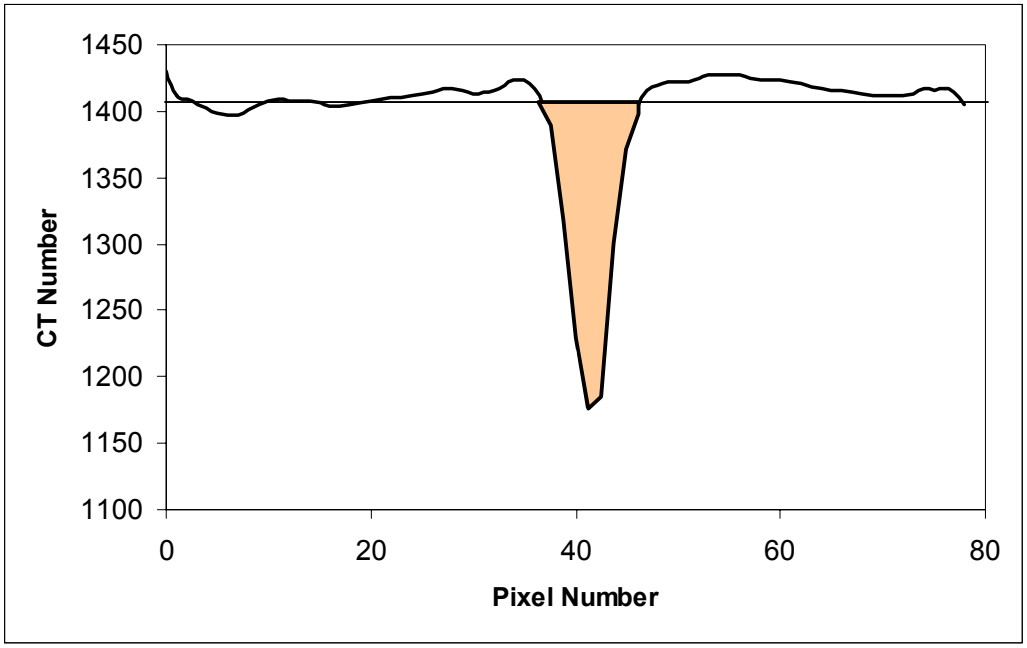

Fig. 3.6— Plot with shaded area representing fracture.

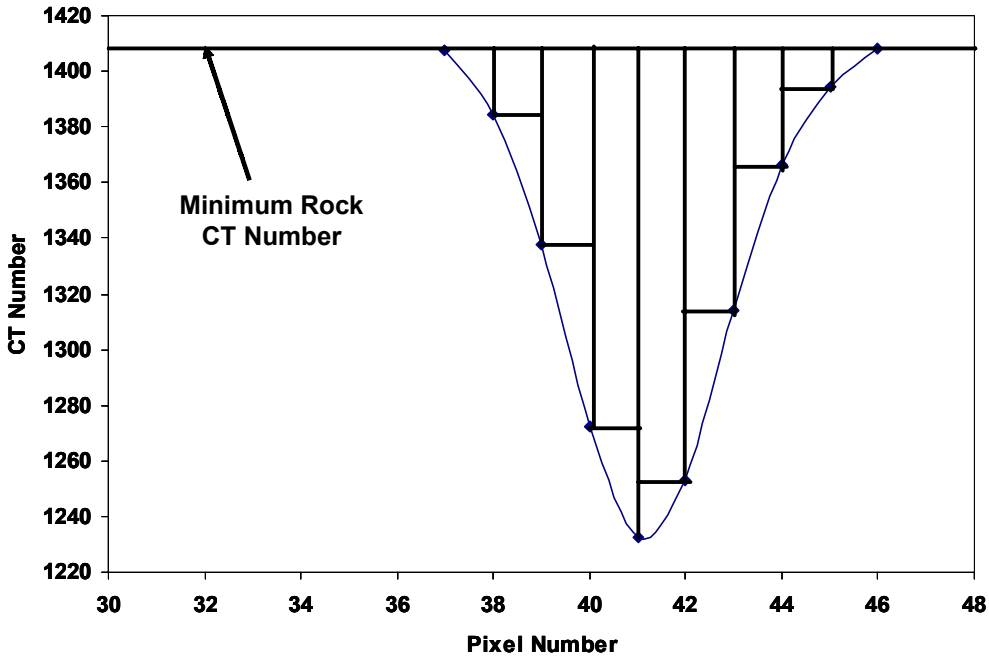

Fig. 3.7— Integrated CT signal determination.

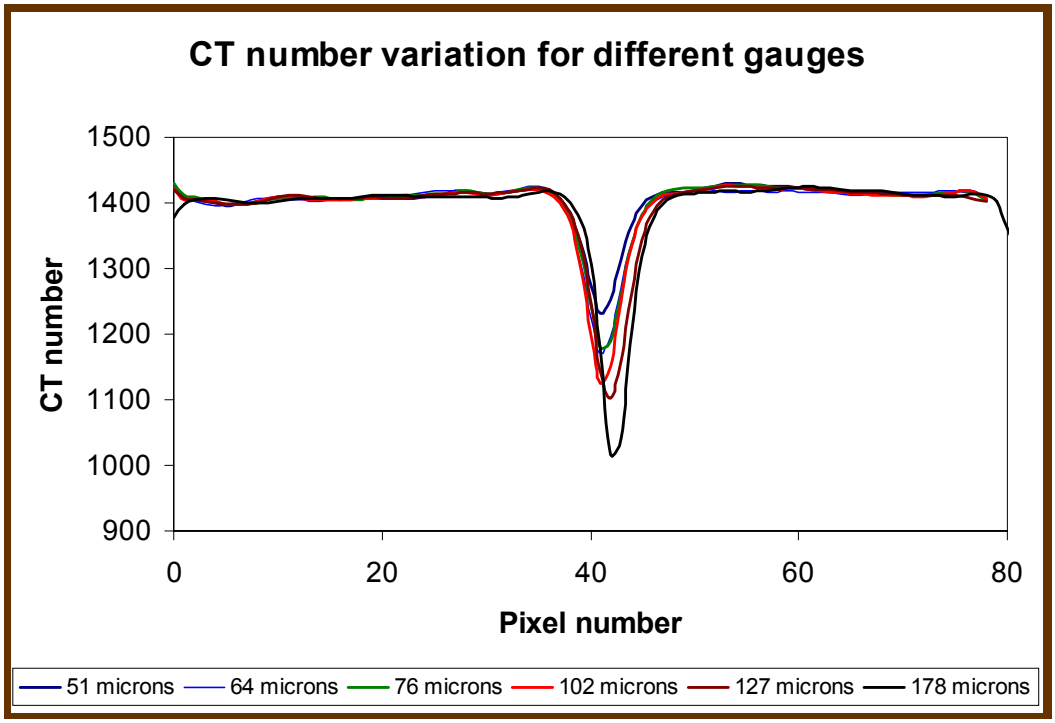

Fig. 3.8— CT number decreases with increase in fracture size.

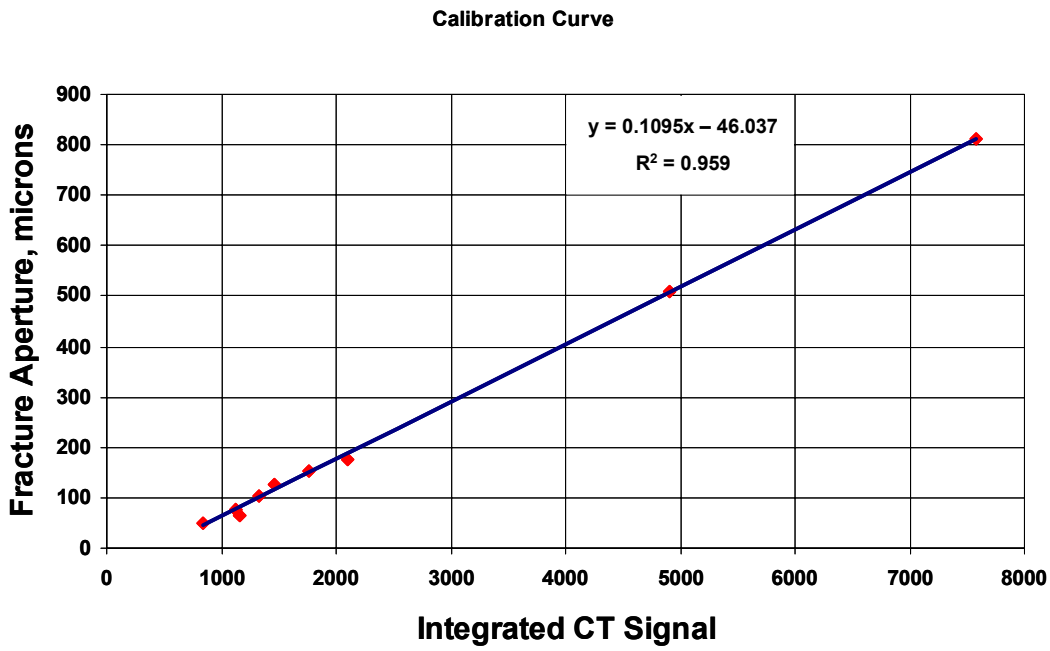

Fig. 3.9—Final calibration curve obtained after area integration.

3.5 References

1. Fatt, I. and Davis, D.H.: "Reduction in Permeability with Overburden Pressure," *Trans.*, AIME (1952) **195**, 329.
2. Gray H. D., Fatt, I., and Bergamini, G.: "The Effect of Stress on Permeability of Sandstone Cores," *SPEJ* (June 1963).
3. Morita, N. *et al.*: "Rock Property Change During Reservoir Compaction," paper SPE 13099 presented at the 1984 SPE Annual Technical Conference and Exhibition, Houston, Texas, 16-19 September.
4. Putra, E., Muralidharan, V., and Schechter, D.S.: "Overburden Pressure Affects Fracture Aperture and Fracture Permeability in a Fracture Reservoir," SA Journal of Technology, Fall 2003.

5. Vinegar, H. J.: "X-ray CT and NMR Imaging of Rocks," *JPT* (March 1986), 257.

6. Wellington, S. L. and Vinegar, H. J.: "CT Studies of Surfactant- Induced CO_2 Mobility Control," paper SPE 14393 presented at the 1985 SPE Annual Technical Conference and Exhibition, Las Vegas, September 22-25.

7. Alajmi, A.F. and Grader, A.S.: "Analysis of Fracture-Matrix Fluid Flow Interactions Using X-Ray CT," paper SPE 65628 presented at the 2000 Eastern Regional Meeting, Morgantown, West Virginia, October 17-19.

8. Burger, J.E. *et al*.: "Effect of Phase Behavior on Bypassing in Enriched Gasfloods,", paper SPE 25254 presented at the 1993 Symposium on Reservoir Simulation, New Orleans, LA, February 28 – March 3.

9. Stones, E.J. *et al*.: "Gravity-Induced Drainage from Fractured Porous Media," paper SPE 24042 presented at the 1992 Western Regional Meeting, Bakersfield, CA, March 30 - April 1.

10. Hicks Jr., P.J. *et al*.: "An Experimental Study of Miscible Displacements in heterogeneous Carbonate Cores Using X-Ray CT," *SPE FE* (March 1994)

11. Keller, A.A.: "High Resolution CAT Imaging of Fractures in Consolidated Materials," *Int. J. Rock Mech. Min. Sci*. (1997), 34 (3/4), 358-375.

12. He, M.: "Application of X-ray Tomography to Measurement of Fractures in Rocks," M.S. Thesis, Stanford University (1998).

IV. Fracture Aperture Distribution

4.1 Introduction

Fluid flow and solute transport through low-permeability tight rocks predominantly occurs in interconnecting fractures. Earlier studies by Snow[2], (1969) and Wilson[3], (1970) assumes the fracture to be a set of parallel plates separated by a constant aperture, and used cubic law to determine fluid flow through the fracture. However, fractures have varied apertures along their path, and therefore, the fluid flow behaves differently from the parallel plate assumption. Upon applying overburden pressure, the rough-walled surfaces can block some portions of the fracture and hence, the fluid flow will not be the same amount as calculated from the parallel plate assumption. Witherspoon *et al.*[5], (1980) have conducted laboratory experiments to validate parallel plate theory and they showed that the parallel plate approximation tends to break down at higher normal stress (>10 MPa) across the fracture. Alfred[17], (2003) also confirmed that the parallel plate assumption is not a valid theory to adequately model the fluid flow experiments when overburden pressure is significant.

Earlier studies on fluid flow through fractures assume that the fracture has constant aperture b_o, represented mathematically by an aperture density distribution $n(b)$, where $n(b)db$ gives the probability of finding aperture values between b and $(b+db)$. This distribution takes the delta form in the case of the parallel plate assumption, with a peak value of b_o, which is given by $\delta(b_o) = \lim_{\varepsilon \to 0} \frac{1}{\varepsilon}$. The analytical solution of a viscous incompressible flow through parallel plate for a steady laminar flow was given by Bear[4], (1972). Once the parallel plate approach is no longer valid, the delta function cannot be assumed for the fracture. Tsang and Witherspoon[6], (1981) accounted for the variation of apertures in a rough fracture, which took a different shape rather than the delta function. Tsang[7], (1984) modeled the variation of fracture apertures by electrical resistors with different resistance values placed on a two-dimensional grid. The results indicate that small apertures play a key role in depressing fluid flow. When the fracture contact area increases, tortuosity and connectivity of fractures become important. Pyrak et al.[10], (1985) performed laboratory experiments wherein they injected molten wood's

metal into single fractures, at different applied stress conditions. The direct evidence of tortuous paths was observed upon opening the cooled metal in the fracture. However, the effect of tortuosity decreases when the distribution is sharply peaked at large apertures with a long tail in the small apertures (Tsang[7], (1984)).

The flow in the single fracture took place in a limited number of channels which was evident from the field experiment carried out on a single fracture by Bourke *et al.*[9], (1985). Upon drilling five holes in the fracture plane and pressurizing each to atmospheric pressure, the results showed that the channels occupied a total area of only about 10% of the fracture plane. Gentier[11], (1986) measured fracture surface roughness profiles in a granite fracture. Upon plotting the apertures, the aperture density distribution was approximated by a gamma function. The density distribution is given by $n(b) = \frac{1}{b_o^2} b e^{-b/b_o}$, where b_o represents the distribution peaks, and the mean aperture is $2b_o$. The same distribution was assumed by Tsang and Tsang[12], (1987) when considering the channeling of flow through fractured media. They assumed the channel width to be a constant of the same order as the correlation length λ, where correlation length is the spatial length within which the apertures have similar values. The reduction in channel apertures affected the tracer breakthrough curves when normal stress across a fracture is increased.

Although gamma distribution is considered, some authors (Bianchi and Snow[1], (1968); Bourke *et al.*[9], (1985)) observed the log-normal distribution of fracture apertures from the experiments conducted on cores and well logs. Later Moreno *et al.*[14], (1988) followed the same approach when conducting flow and tracer transport model experiments in a single fracture. Using the approach, the flow patterns showed strong resemblance to field observations made by Bourke[13], (1987). Tsang and Tsang[15], (1990) used log-normal approach to distribute fracture apertures, (for determining hydrological methods) to obtain relationship between flow and transport measurements of variable apertures. The density function of the log-normal distribution is $n(b)db = \frac{1}{\sqrt{2\pi\sigma^2}} \exp[\frac{-(\log b - \log b_o)^2}{2\sigma^2}] \frac{1}{(\ln 10)b} db$, where σ is the logarithm of the apertures and ($\log b_o$) is the mean. The quantity b_o is the most probable aperture which is

smaller than the mean aperture given by $\bar{b} = b_o \exp[(\sigma \ln 10)^2 / 2]$. They determined the mean aperture from flow and transport measurements and distributed the fractures with the log-normal approach. For a log-normal approach, the geometric mean b_o is smaller than the arithmetic mean b and the discrepancy increases with the spread of the aperture distribution σ. They determined aperture variance from tracer breakthrough. Upon injecting mercury in the fractures, an isolated patch in the larger aperture region occurred and spatial correlation length became small, increasing the occurrence of isolated patches. Alfred[17], (2003) also assumed lognormal distribution for the fracture apertures, for considering fracture roughness. The parallel plate model could not adequately represent the fluid flow results of the laboratory experiment and hence using the fracture aperture distribution, he obtained a better match for the experimental results. He also concluded that beyond a particular value for the mean aperture, the effects of roughness and tortuosity were insignificant.

Keller[16], (1996) imaged the fracture apertures using X-ray CT scanner and found that most of the apertures are in the range of 300 to 500 microns with the exception of some high aperture spikes as high as 4500 microns. Using three different cores, he concluded that the log-normal distribution is adequate in characterizing the fracture aperture. He also compared the geometric mean with the mechanical mean of the apertures and found out that the geometric mean was consistently lower than the mechanical mean. He suggested that for a perfect log-normal distribution, $\frac{a_h}{a_m} = \exp(-\frac{\sigma_h^2}{2})$ where a_h is the geometric mean of the aperture (also known as hydraulic aperture) and a_m is the mechanical mean of the apertures. The smaller aperture regions correlated best with the log-normal distribution.

While a log-normal distribution was suggested for the variable fracture apertures with a single stress level, the issue of the distribution pattern for different stress levels is still unresolved. Usually the fracture apertures were stochastically generated according to the particular distribution and sensitivity studies were made by changing the variance for a particular mean value, however, the mean and variance change when the stress level changes, which might tend to close some of the smaller apertures. Therefore, distribution

pattern cannot be assumed to be the same for all the stress levels unless proved by imaging and measuring the fracture apertures for various levels. This research uses X-ray CT scanner to image the fracture aperture under various overburden pressures and using a calibration curve, measures the fracture aperture at various points along the length of the core, thus generating sufficient data for characterizing the distributions of fracture apertures. The effect of the stress level in the aperture distribution will be useful in analyzing flow and transport phenomenon and tracer studies in the stress-sensitive reservoirs.

4.2 Methodology

4.2.1 Experimental Procedure

For the sake of simplicity, Berea core was used to conduct the experiment. A 1 inch diameter by 2.36 inch length core was used. The core was fractured mechanically in the laboratory using hydraulic cutter as shown in Fig. 4.1. The fractured core was then imaged in the X-ray CT scanner. Images were taken every 1 mm up to 60 mm along the length of the core. The core was then subjected to overburden pressure of 500 psi and again the scans were taken at the same locations. The same procedure was repeated for various overburden pressures of 1000 psi and 1500 psi.

4.2.2 Image Transfer

The images obtained from X-ray CT scanner were transferred to VOXELCALC, software for reading the X-ray data, to obtain the CT number in each pixel. Comparisons of the CT numbers can be made for any row and column across the core as shown in Figs. 4.2 and 3. Figs. 4.4 to 4.7 show the images taken with and without overburden pressures.

4.2.3 Data Preparation

About 6000 data points were taken for each overburden condition. The aperture values from the CT data were obtained by the calibration curve as discussed in the previous section.

4.2.4 Data Distribution

Mean, variance, and standard deviation were obtained for the dataset, which was then plotted. Table. 4.1 shows the range and frequencies of the apertures with and without overburden pressure. Probability distribution was calculated for each condition and is plotted against the fracture apertures as shown in Figs. 4.8 to 4.11. A comparative study was made for different overburden pressures and the result is plotted in Fig. 4.12.

4.3 Discussion

The apertures are distributed in the range of 0 to 2200 microns, with probable apertures in the range of 100 to 500 microns as shown in Fig. 4.8. The tail of the aperture distribution is long and the aperture distribution is right skewed which suggests that the distribution might follow either gamma or lognormal distribution as given in the earlier studies (Gentier[11], (1986); Tsang and Tsang[12], (1987); Keller[16], (1996)). The tail of the apertures controls the fluid flow as fluid will tend to flow through preferred channels of least resistance (Abelin *et al.*[8], (1983), Alfred[17], (2003)). Furthermore, Abelin *et al.*[8] showed that the equivalent apertures derived from tracer migration experiments were bigger than those derived from constant head permeability measurements. Permeability measurements will be largely controlled by small apertures, which in this case is in the range of 100 to 500 microns. The flow rate calculated from this measured permeability will be different due to the presence of some big apertures in the range of 1000 to 2000 microns. Such big apertures, if interconnected may result in larger flow rate than what was calculated. The probability of finding an aperture in the range of 100 to 500 microns is 0.887. There is still 12% chance that the big apertures might be interconnected. The observed result is plotted in Fig. 4.8. The calculated fracture aperture values, when distributed, followed lognormal distribution (Fig. 4.13), with a mean aperture value of 370.53 microns and a variance of 44847. The most probable aperture value, calculated from lognormal distribution is 326.783 microns. The most probable aperture is less than the mean aperture value due to the large variance of the aperture values. Higher the variance, the more skewed the distribution becomes.

Upon increasing the overburden pressure, the mean of the apertures shifts to a lower value (Figs. 4.9-4.11), which suggests that the permeability has decreased due to applied overburden pressure. The decrease of the mean apertures is drastic when an initial overburden pressure of 500 psi was applied. The mean of the apertures becomes 197.997 microns from 370.53 microns as shown in Table. 4.2. The fracture surfaces are rough and have many contact points along the path. If the apertures are more frequent, the contact points become weak and tend to breakdown upon applying the stress. The decrease is not significant upon further increase in overburden pressures. The observed results for different overburden pressures are plotted in Figs. 4.9-4.11. Comparison of observed results with lognormal distribution (Figs. 4.14-4.16) shows that the difference is very small, which proves that the data follows lognormal distribution for different overburden pressures. A comparison of lognormal distribution was made for fracture apertures at different overburden pressures (Fig. 4.17). Since most reservoirs experience overburden pressures, this research will be important to identify some of the uncertainties in fluid flow through fractured reservoirs.

4.4 Conclusions

1. The parallel plate approach of the fractures is no longer valid when the fracture aperture is small due to significant applied overburden pressure.
2. The result of this study confirms the results of previous studies, that fracture aperture distribution is lognormal distribution at no overburden pressure. Upon applied overburden pressure, the distribution still follows the common lognormal distribution.

Table 4.1—Dataset showing range and frequency for various overburden pressure conditions.

No Overburden Pressure		500 Psi Overburden pr.		1000 Psi Overburden		1500 Psi Overburden	
Range	Count	Range	Count	Range	Count	Range	Count
0 - 100	68	0 - 100	1508	0 - 100	2558	0 - 100	2892
100 - 200	353	100 - 200	2393	100 - 200	1999	100 - 200	1890
200 - 300	2139	200 - 300	1287	200 - 300	812	200 - 300	684
300 - 400	2119	300 - 400	368	300 - 400	261	300 - 400	193
400 - 500	832	400 - 500	176	400 - 500	125	400 - 500	109
500 - 600	226	500 - 600	102	500 - 600	85	500 - 600	84
600 - 700	134	600 - 700	79	600 - 700	56	600 - 700	63
700 - 800	85	700 - 800	38	700 - 800	59	700 - 800	36
800 - 900	61	800 - 900	43	800 - 900	54	800 - 900	38
900 - 1000	34	900 - 1000	25	900 - 1000	29	900 - 1000	16
1000 - 1100	27	1000 - 1100	33	1000 - 1100	8	1000 - 1100	4
1100 - 1200	22	1100 - 1200	15	1100 - 1200	1	1100 - 1200	0
1200 - 1300	25	1200 - 1300	4	1200 - 1300	0	1200 - 1300	1
1300 - 1400	19	1300 - 1400	3	1300 - 1400	0	1300 - 1400	0
1400 - 1500	13	1400 - 1500	0	1400 - 1500	0	1400 - 1500	0
1500 - 1600	16	1500 - 1600	0	1500 - 1600	0	1500 - 1600	0
1600 - 1700	7	1600 - 1700	0	1600 - 1700	0	1600 - 1700	0
1700 - 1800	6	1700 - 1800	0	1700 - 1800	0	1700 - 1800	0
1800 - 1900	14	1800 - 1900	0	1800 - 1900	0	1800 - 1900	0
1900 - 2000	5	1900 - 2000	0	1900 - 2000	0	1900 - 2000	0
2000 - 2100	0	2000 - 2100	0	2000 - 2100	0	2000 - 2100	0
2100 - 2200	1	2100 - 2200	0	2100 - 2200	0	2100 - 2200	0

Table 4.2—Statistical Parameters for different overburden conditions.

	No_overburden	500_overburden	1000_overburden	1500_overburden
Mean	370.5273743	197.9978943	157.4180145	138.6561127
Variance	44847.62887	29781.35105	26372.14946	22599.10453
Std_deviation	211.7725876	172.5727413	162.3950414	150.3299855

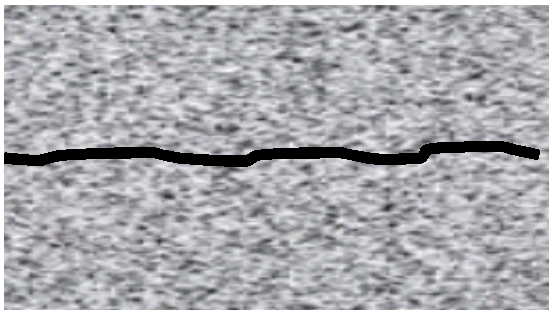

Fig. 4.1—Berea core with fractured in the central plane.

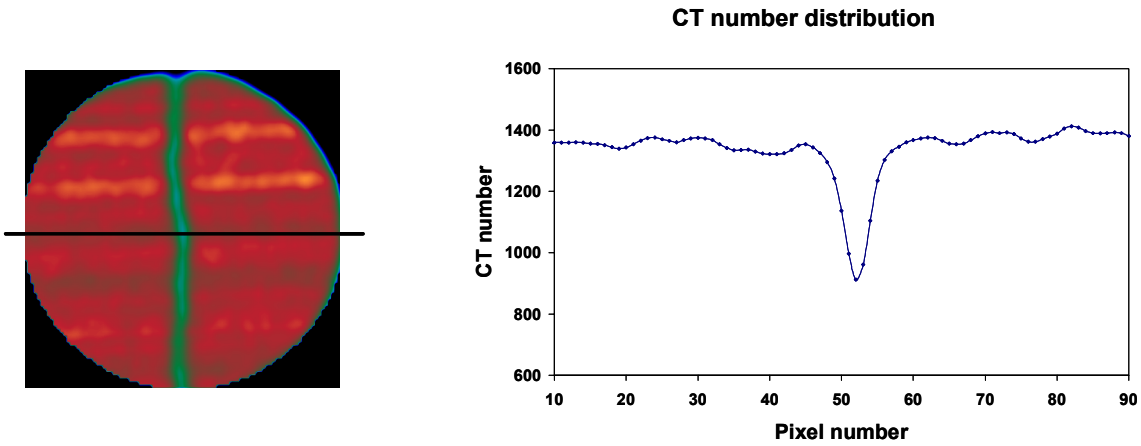

Fig. 4.2—Distribution of CT number along the row showing a dip for the fracture.

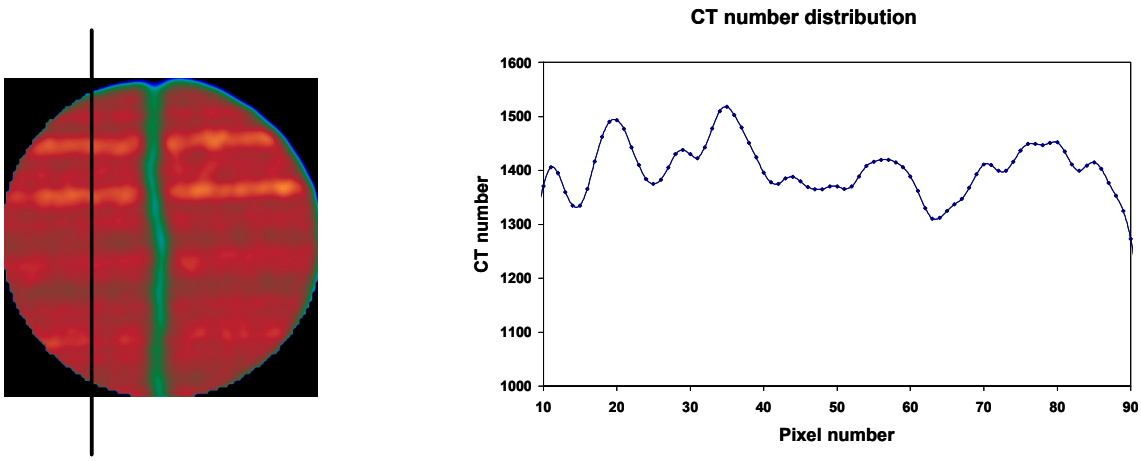

Fig. 4.3—Distribution of CT number along the column showing the heterogeneity.

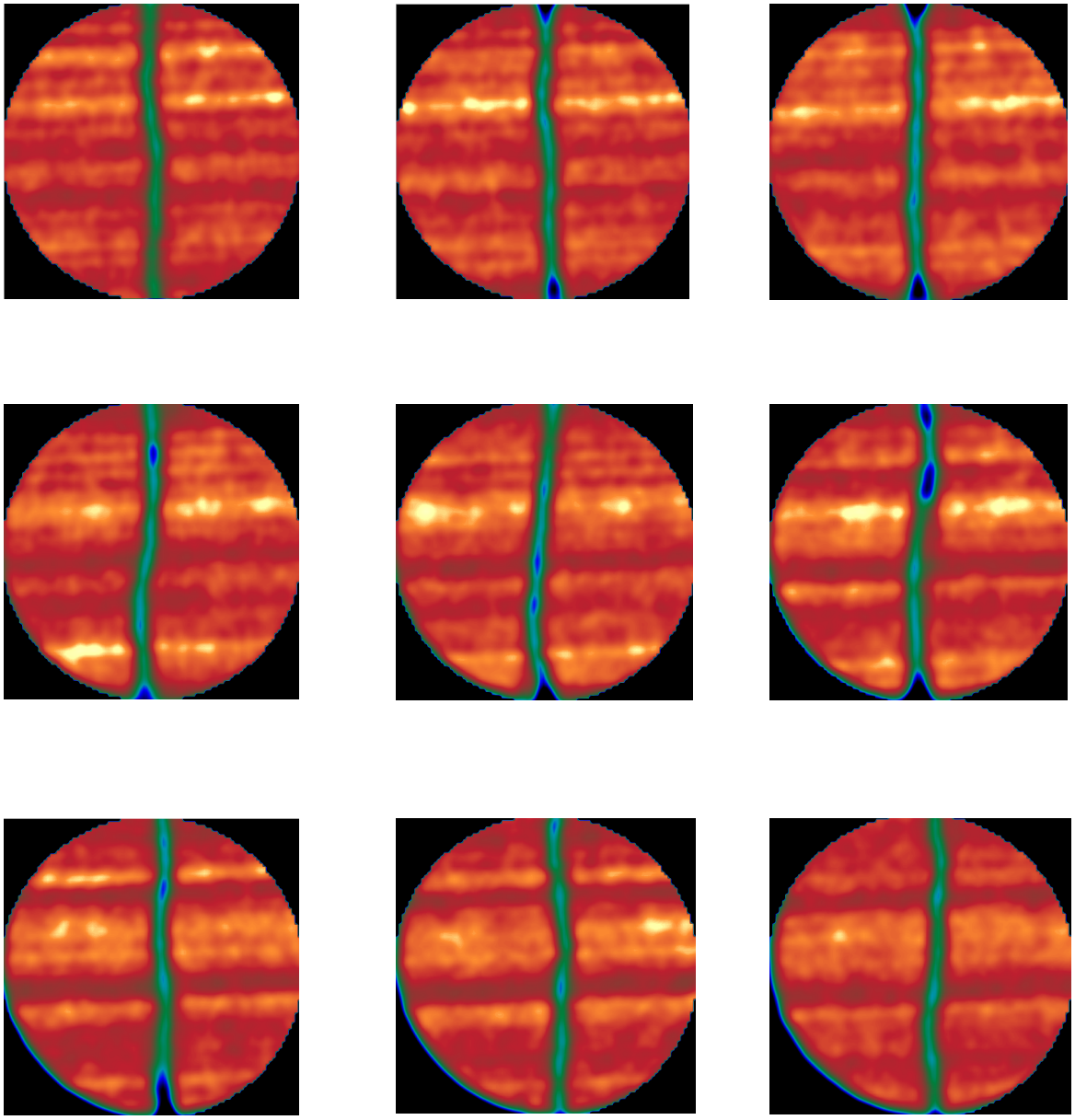

Fig. 4.4—Sample scans taken along the length of the core without overburden pressure.

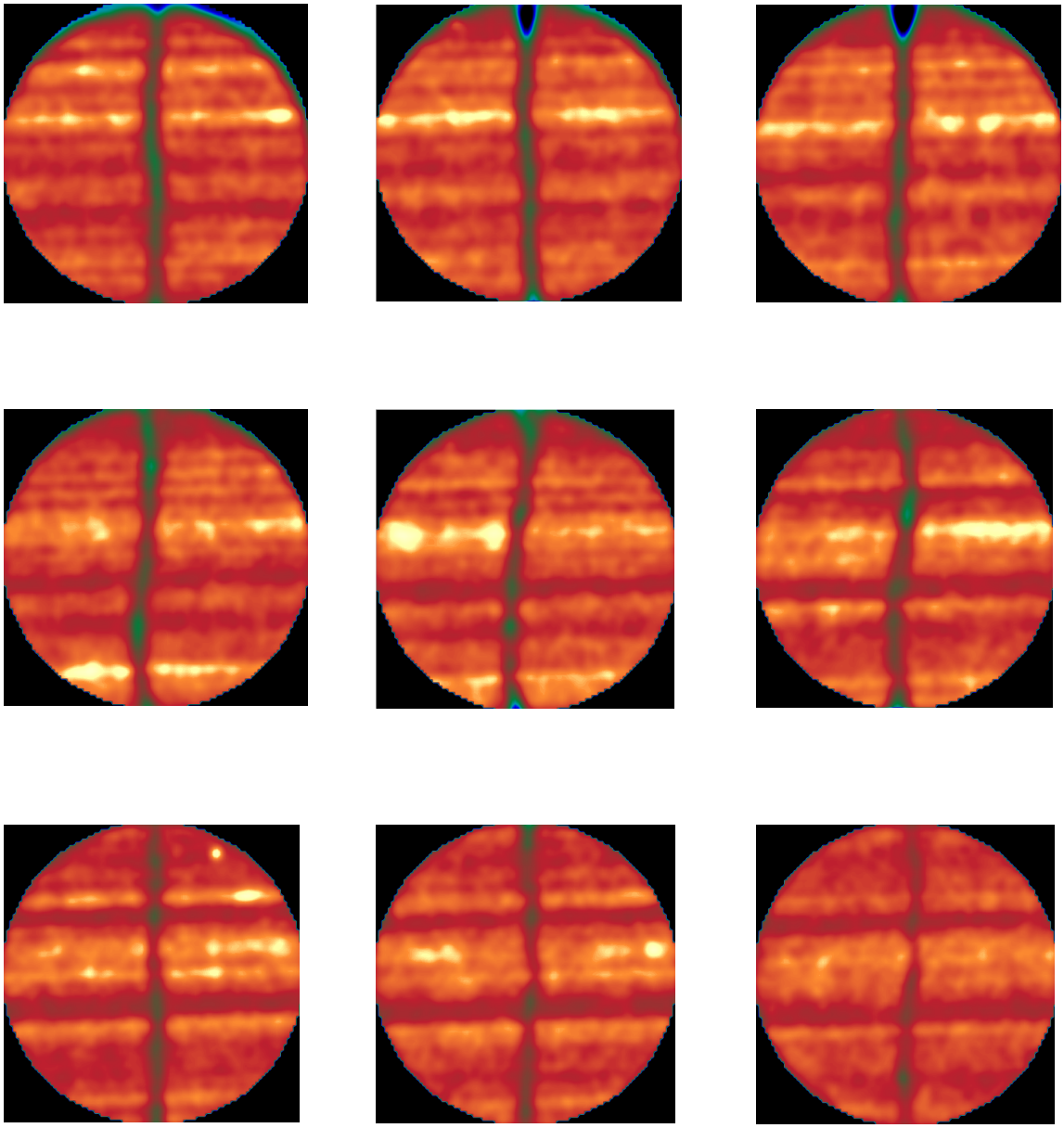

Fig. 4.5—Sample scans taken along the length of the core with 500 psi overburden pressure.

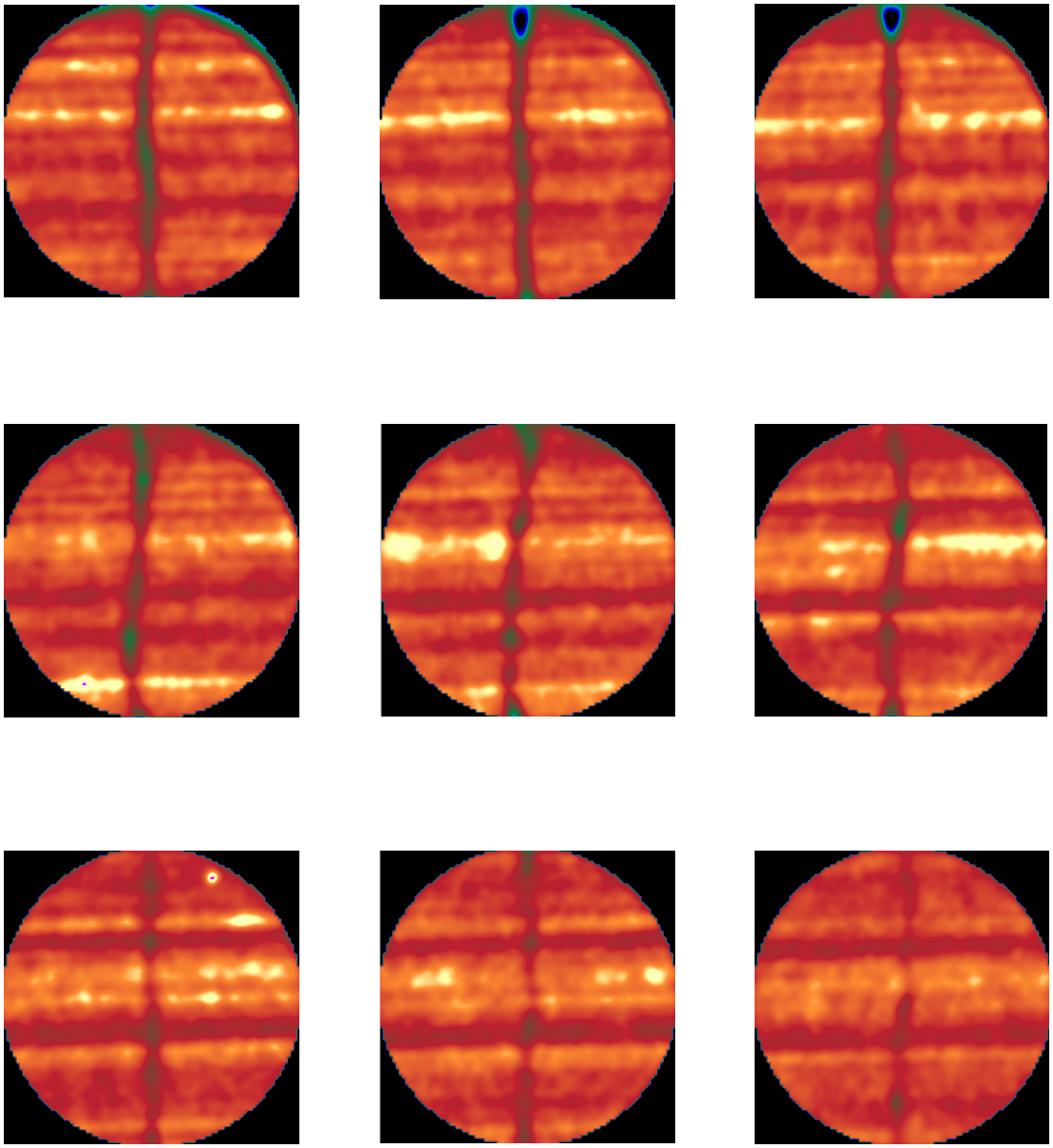

Fig. 4.6—Sample scans taken along the length of the core with 1000 psi overburden pressure.

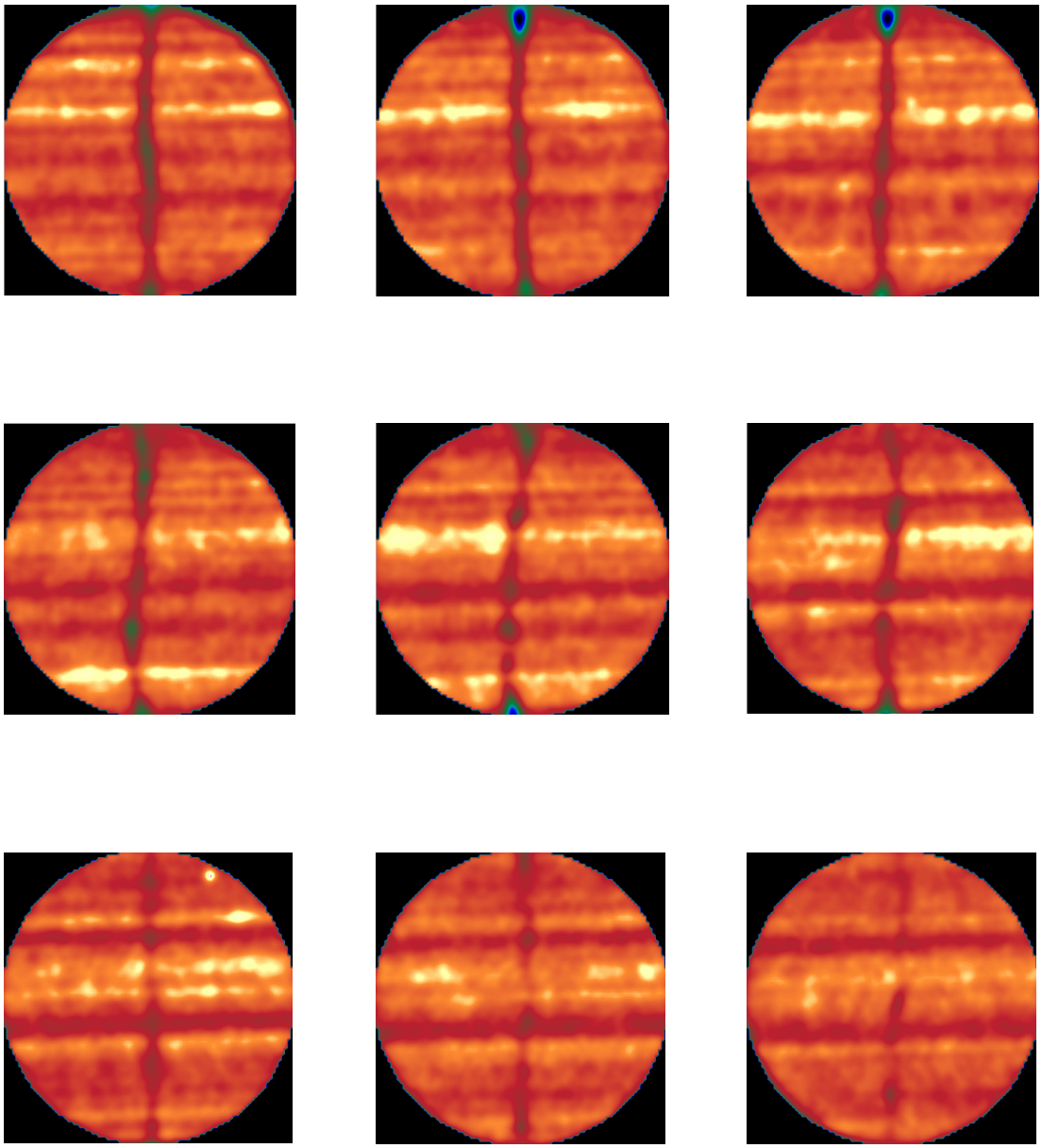

Fig. 4.7—Sample scans taken along the length of the core with 1500 psi overburden pressure.

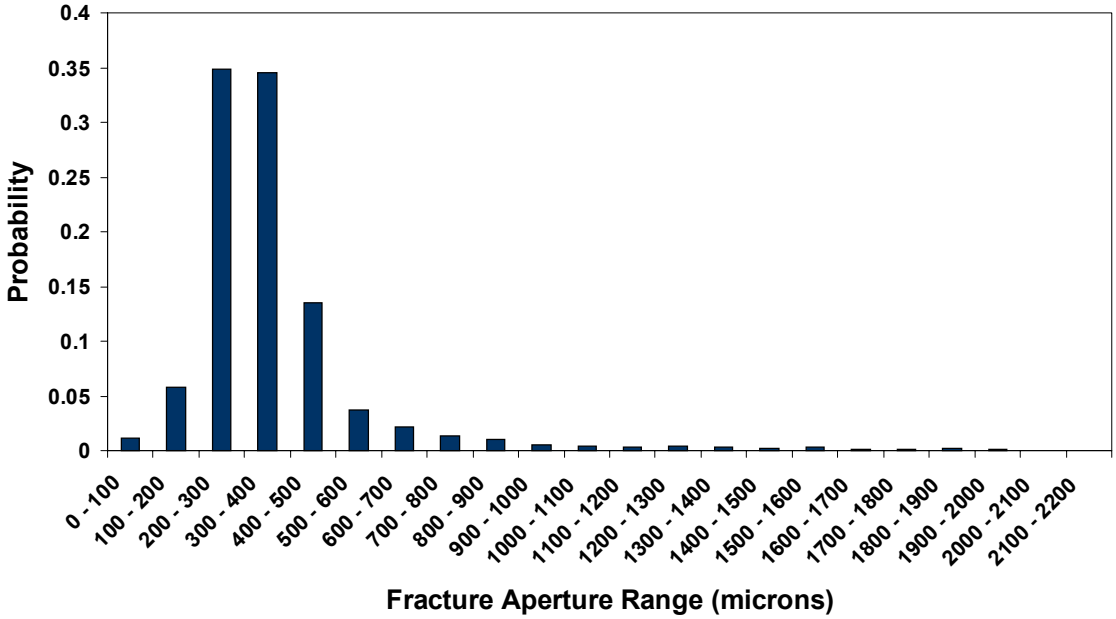

Fig. 4.8—Probability distribution of fracture apertures without overburden pressure.

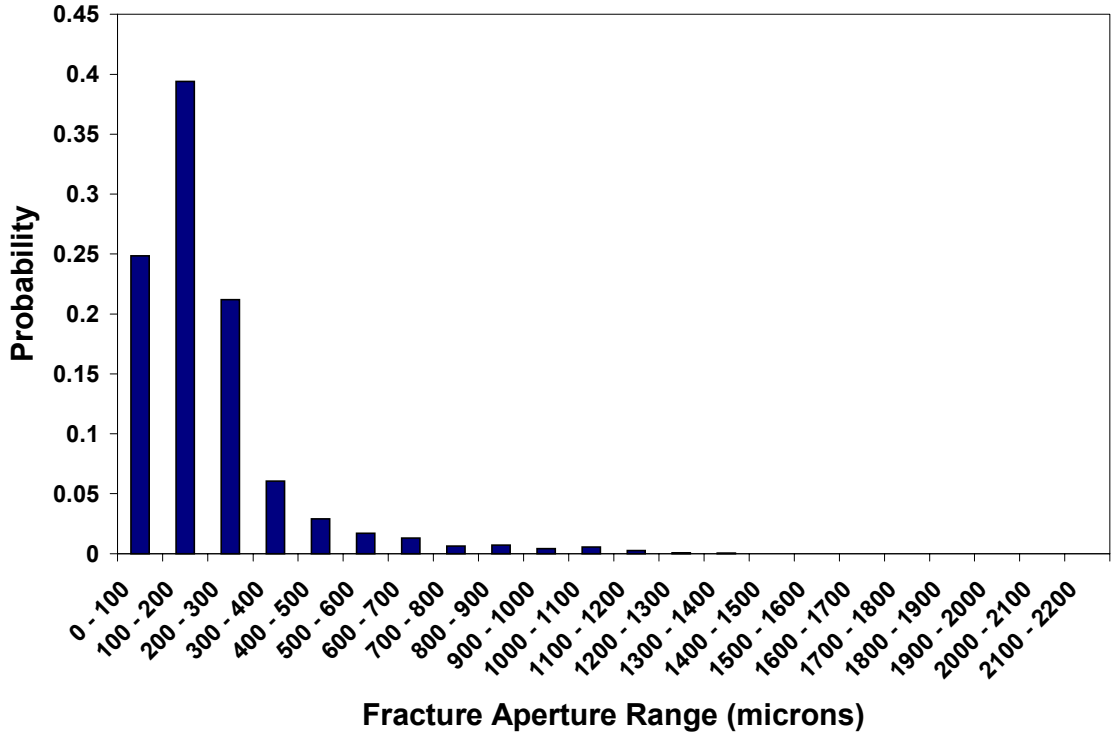

Fig. 4.9—Probability distribution of fracture apertures at 500 psi overburden pressure.

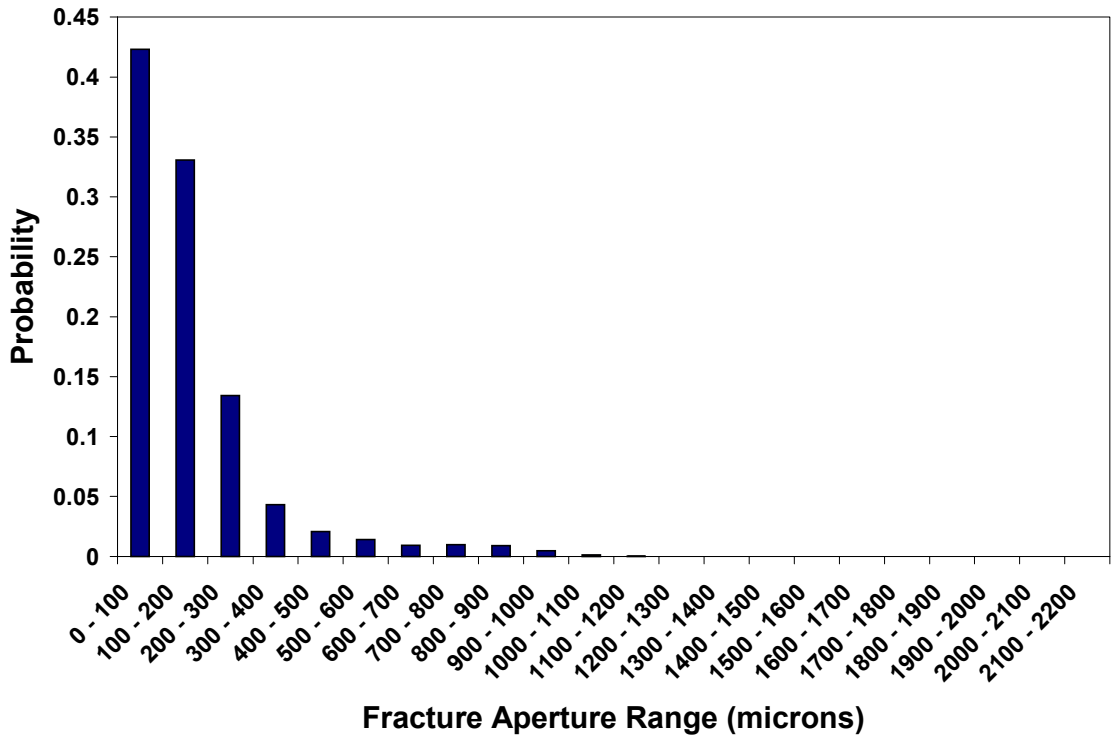

Fig. 4.10—Probability distribution of fracture apertures at 1000 psi overburden pressure.

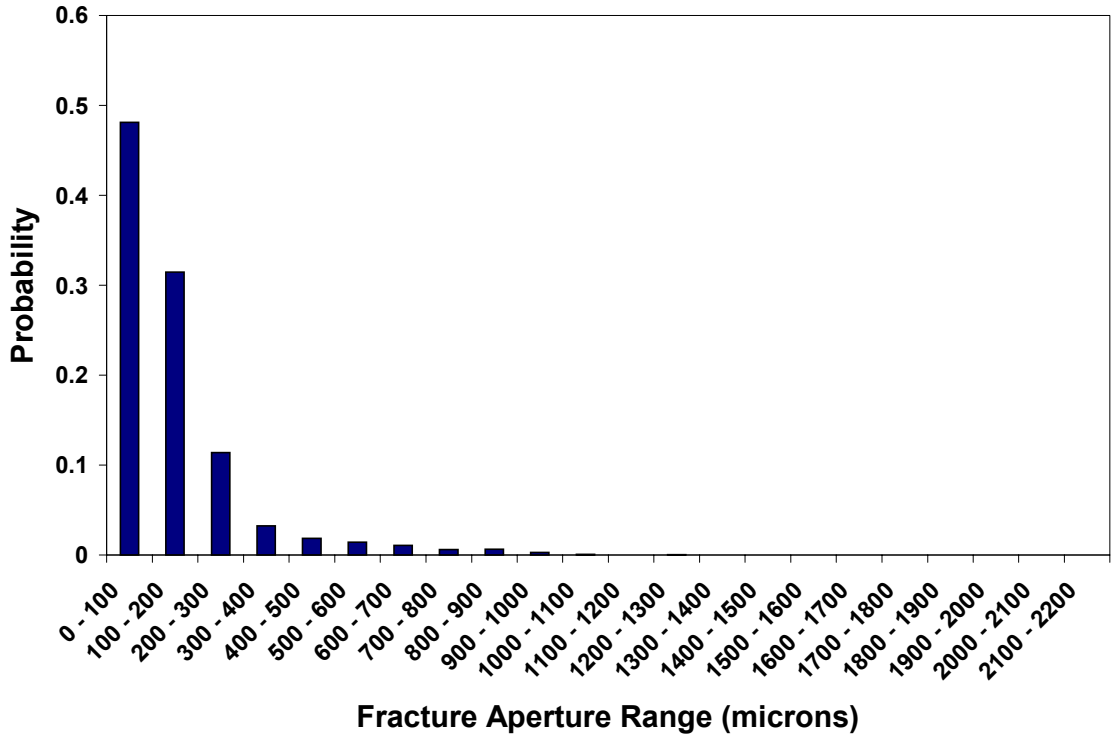

Fig. 4.11—Probability distribution of fracture apertures at 1500 psi overburden pressure.

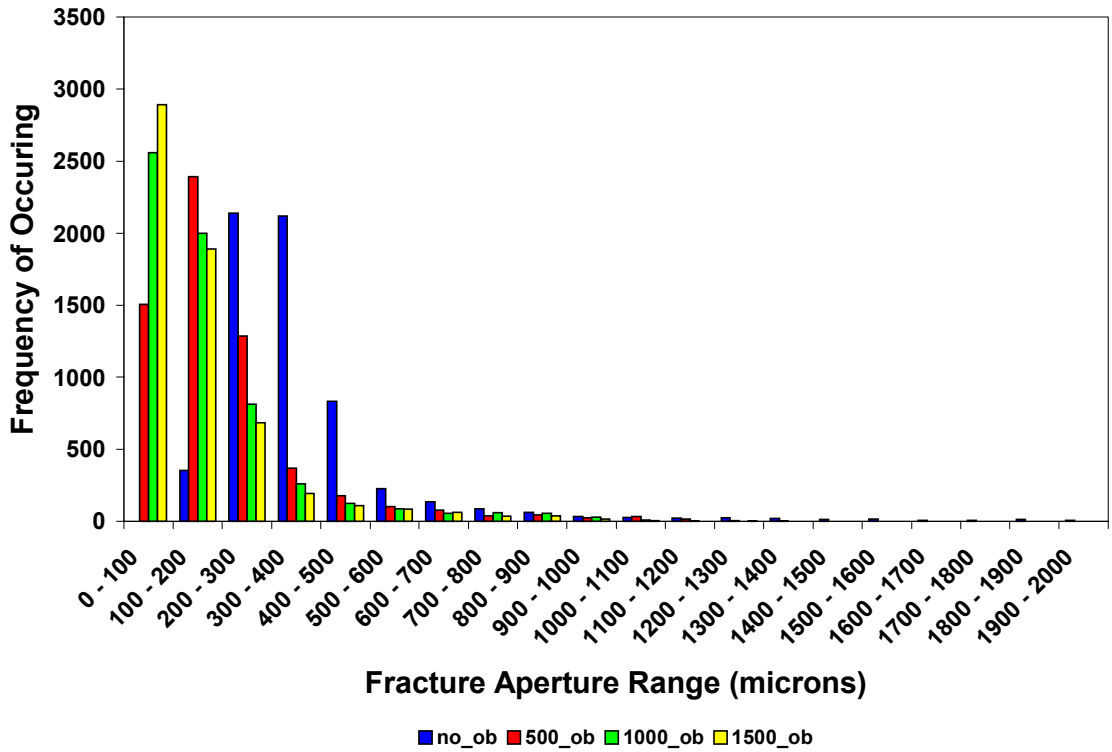

Fig. 4.12—Comparative study of fracture aperture distribution under various overburden pressures.

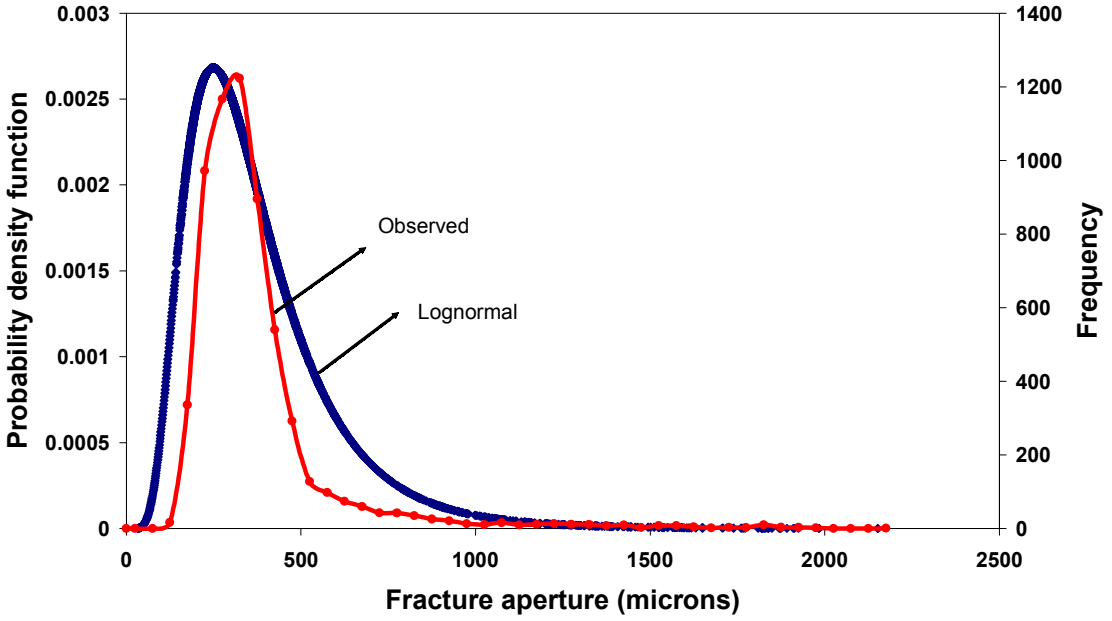

Fig. 4.13—Comparison of Observed and Lognormal distribution of fracture apertures without overburden pressure.

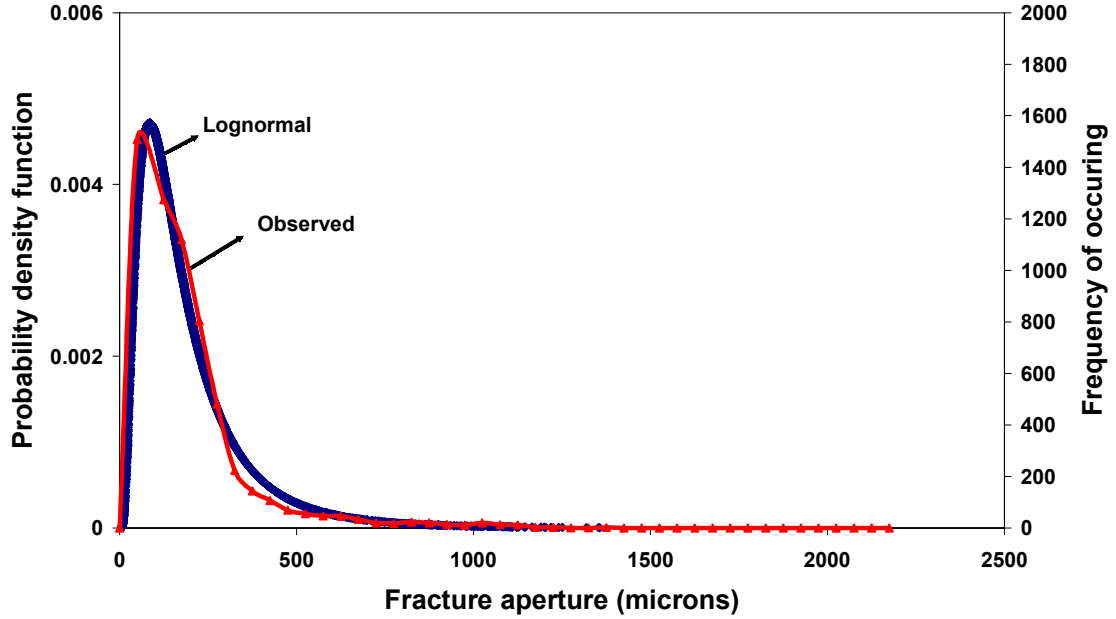

Fig. 4.14—Comparison of Observed and Lognormal distributions of fracture apertures at 500 psi overburden pressure.

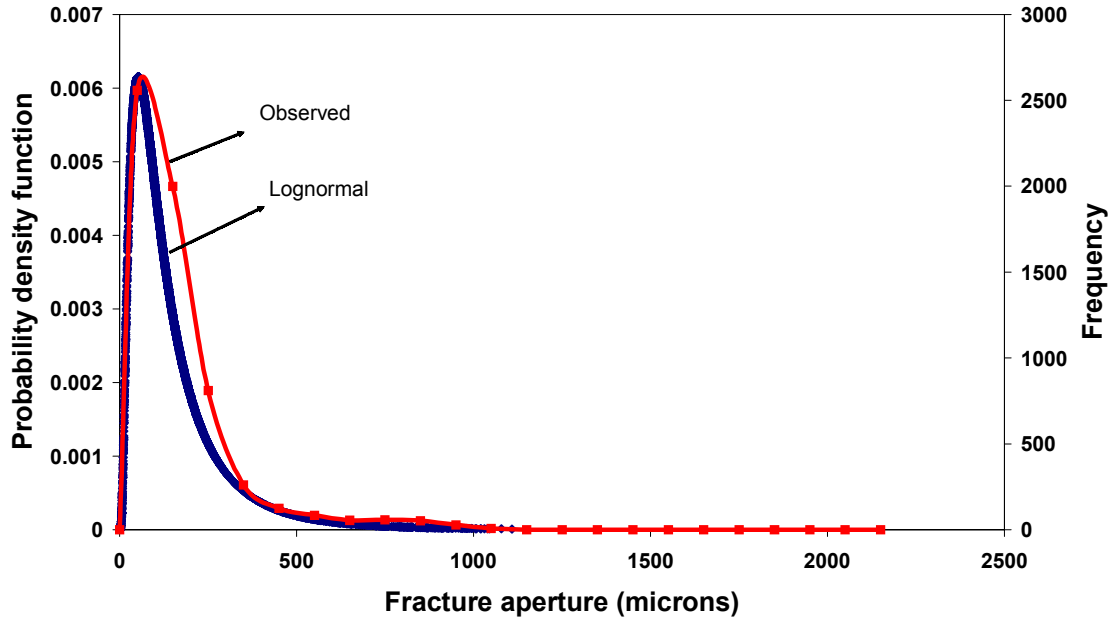

Fig. 4.15—Comparison of Observed and Lognormal distributions of fracture apertures at 1000 psi overburden pressure.

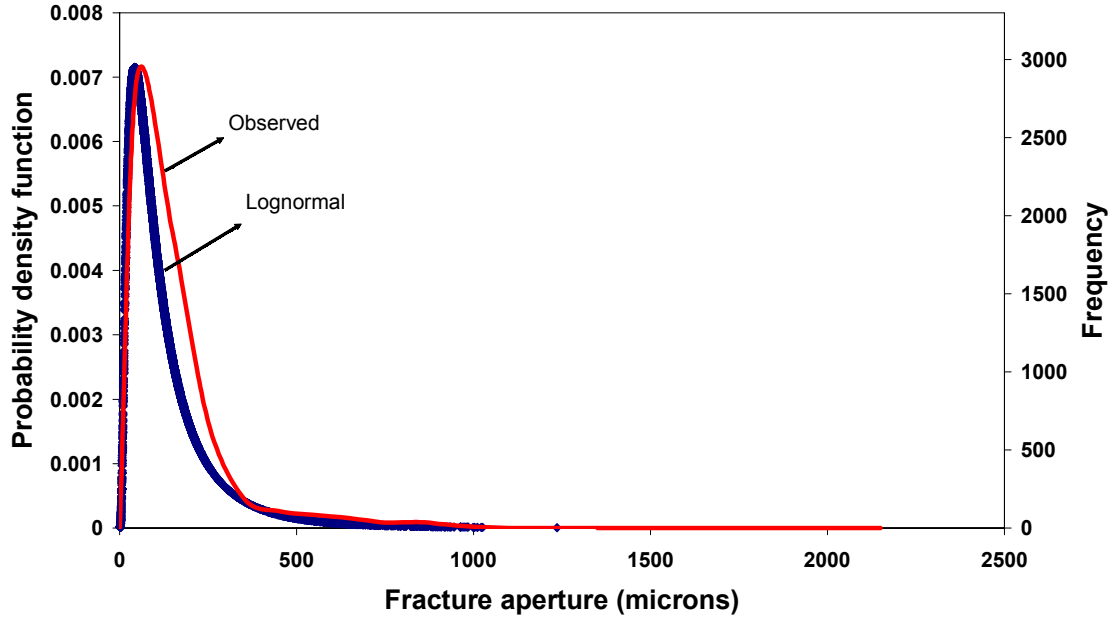

Fig. 4.16—Comparison of Observed and Lognormal distributions of fracture apertures at 1500 psi overburden pressure.

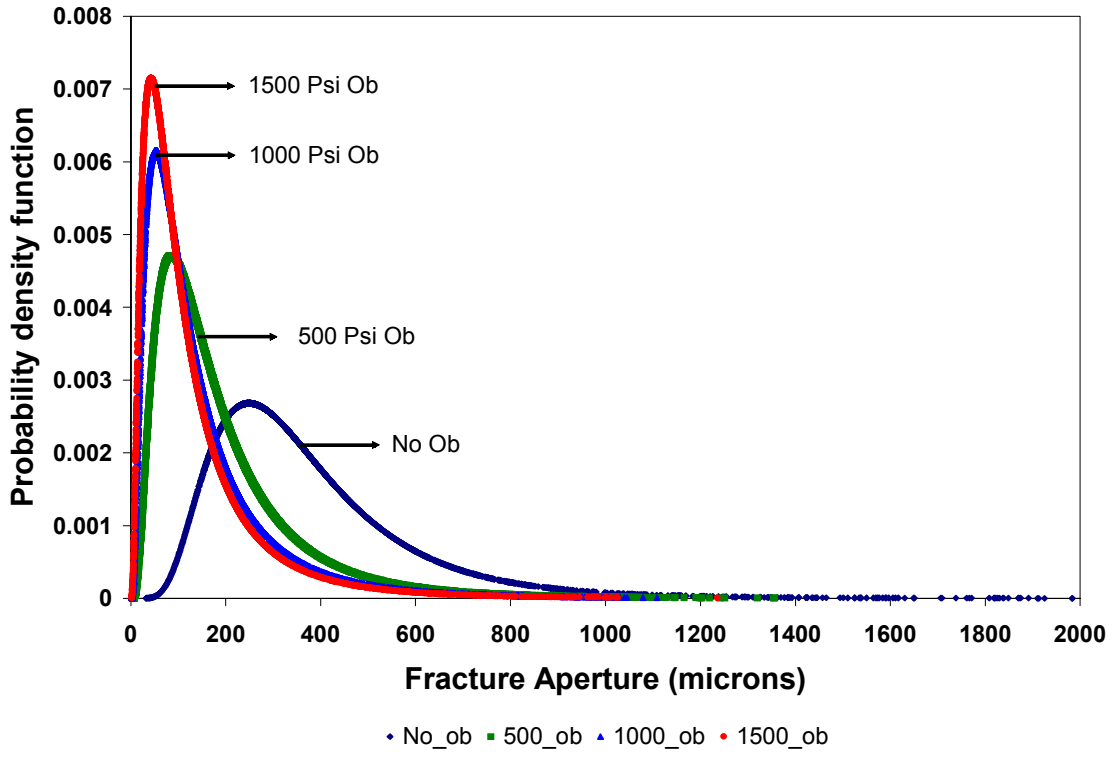

Fig. 4.17—Comparison of Lognormal distributions at different overburden pressures.

4.5 References

1. Bianchi, L. and Snow, D.: "Permeability Crystalline Rock Interpretated from Measured Orientations and Apertures of Fractures*," Annu. Arid Zone*, 8(2), 231-245, 1968.
2. Snow, D. T.: "Anisotropic Permeability of Fractured Media," *Water Resources Research*, 5(6), 1273-1289, 1969.
3. Wilson, C. R.: "An Investigation of Laminar Flow in Fractured Porous Rocks," Ph.D. thesis, Univ. of California, Berkeley, 1970.
4. Bear, J.: "*Dynamics of Fluids in Porous Media*," 764 pp, Elsevier, New York, 1972.
5. Witherspoon, P. A., Wang, J. S. Y., Iwai, K., and Gale, J. E.: "Validity of Cubic Law for Fluid Flow in a Deformable Rock Fracture," *Water Resources Research*, 16(6), 1016-1024, 1980.
6. Tsang, Y. W. and Witherspoon, P. A.: "The Dependence of Fracture Mechanical and Fluid Properties on Fracture Roughness and Sample Size," *J. Geophys. Res.*, 88(B3), 2359-2366, 1983.
7. Tsang, Y. W.: "The Effect of Tortuosity on Fluid Flow Through a Single Fracture," *Water Resources Research*, 20(9), 1209-1215, 1984.
8. Abelin, H., Neretnieks, I., Tunbrant, S., and Moreno, L.: "Final Report of the Migration in a Single Fracture: Experimental Results and Evaluation," *Stripa Proj. Sven. Karnbransleforsorjning Tech. Rep.* 85-03, Nucl. Fuel Safety Proj., Stockholm, Sweden, May 1985.
9. Bourke, P. J., Dunance, E. M., Heath, M. J., and Hodgkinson, D. D.: "Fracture Hydrology Relevant to Radionuclide Transport, AERE *Rep.* 11414, Atomic Energy Res. Estab., Harwell, United Kingdom, 1985.
10. Pyrak, L. R., Myer, L. R., and Cook, N. G. W.: "Determination of Fracture Void Geometry and Contact Area at Different Effective Stress," *Eos Trans.* AGU (abstract), 66(46), 903, 1985.
11. Gentier, S.: "Morphologie et comportement hydromécanique d'une fracture naturelle dans un granite sous contrainte normale," doctoral thesis, Univ. d'Orléans, France, 1986.

12. Tsang, Y. W. and Tsang, C. F.: "Channel Model of Flow Through Fractured Media," *Water Resources Research*, 23(3), 467-479, 1987.
13. Bourke, P. J.: "Channeling of Flow Through Fractures in Rock," in *Proceedings* of GEOVAL-87 International Symposium, Swed. Nucl. Power Inspectorate, Stockholm, Sweden, 1987.
14. Moreno, L., Tsang, Y. W., Tsang, C. F., Hale, F. V., and Neretnieks, I.: "Flow and Tracer Transport in a Single Fracture: A Stochastic Model and Its Relation to Some Field Observations," *Water Resources Research*, 24(12), 2033-2048, 1988.
15. Tsang, Y. W. and Tsang, C. F.: "Hydrological Characterization of Variable-Aperture Fractures," *Rock Joints*, Barton & Stephansson (eds), Balkema, Rotterdam, 1990.
16. Keller, A. A.: "Single and Multiphase Flow and Transport in Fractured Porous Media," doctoral thesis, Stanford University, 1996.
17. Alfred, D.: "Modeling Fluid Flow Through a Single Fracture Using Experimental, Stochastic and Simulation Approaches," master's thesis, Texas A&M University, 2003.
18. Jensen, L., Lake, L. W., Corbett, P. W. M., and Goggin, D. J.: "Statistics For Petroleum Engineers and Geoscientists," 2nd Edition, Handbook of Pertoleum Exploration and Production, 2, Elsevier, Netherlands, 2000.

APPENDIX A: PROJECT FACT SHEET

CONTRACT TITLE: Investigation of Efficiency Improvement During CO_2 Injection in Hydraulically and Naturally Fractured Reservoirs

ID NUMBER: DE-FC26-01BC15361 **B&R CODE:** AC1005000	**CONTRACTOR:** Texas Engineering Experiment Station **ADDR:** 322 Wisenbaker Engineering Research Center College Station, TX 77843
DOE PROJECT MANAGER: **NAME:** Daniel J. Ferguson **LOCATION:** NPTO **PHONE:** 918/ 699-2047 **E-MAIL:** dan.ferguson@npto.doe.gov	**CONTRACT PROJECT MANAGER:** **NAME:** David Schechter **PHONE:** 979/ 845-2275 **FAX:** 979/845-1307 **E-MAIL:** schech@spindletop.tamu.edu
PROJECT SITE **CITY:** College Station **STATE:** TX **CITY:** **STATE:** **CITY:** **STATE:**	**CONTRACT PERFORMANCE PERIOD:** 9/28/2001 to 9/27/2004 **PROGRAM:** Exploration & Production **RESEARCH AREA:** **PRODUCT LINE:** ADIS

CO-PARTICIPANTS:

PERFORMER:	**CITY:**	**STATE:**	**CD:**
PERFORMER:	**CITY:**	**STATE:**	**CD:**
PERFORMER:	**CITY:**	**STATE:**	**CD:**
PERFORMER:	**CITY:**	**STATE:**	**CD:**

FUNDING (1000'S)	DOE	CONTRACTOR	TOTAL
PRIOR FISCAL YRS	0	0	0
FY 2001 CURRENT OBLIGATIONS	309	78	387
FUTURE FUNDS	628	157	785
TOTAL EST'D FUNDS	937	235	1172

OBJECTIVE: The objective of this project is to perform unique laboratory experiments with Artificial fractured cores (AFCs) and X-ray CT to examine the physical mechanisms of bypassing in HFR and NFR that eventually result in less efficient CO_2 flooding in heterogeneous or fracture-dominated reservoirs. Core flooding experiments in artificially fractured and oil-saturated cores at reservoir conditions will be performed under different conditions of fracture configurations and fracture aperture distributions to investigate matrix-fracture transfer mechanisms. The fluid flow and fracture aperture distributions will be imaged in-situ and real time using X-ray CT. The benefit of WAG in highly heterogeneous reservoirs will be determined. Various CO_2 injection rates, above and below the MMP, will be performed to optimize the operating injection rate and minimize bypassed oil as a result of hydraulic or natural fractures. Numerical analysis will be conducted to model the physical mechanisms of bypassing oil. Results will be important in modeling actual physical mechanisms during CO_2 injection.

PROJECT SUMMARY

Background:

The primary goal of this research is to maximize the potential of CO_2 flooding in the domestic U.S. As more technical knowledge accumulates it becomes clear that natural and hydraulically induced fractures often dominate pattern reservoir or sweep efficiency. As the level of sophistication grows, low permeability reservoirs become more amenable to Enhanced Oil Recovery (EOR) via CO_2. Low permeability reservoirs are usually characterized by brittle matrix rock, which cracks under natural or induced conditions.

Many of the issues involved in saturation distribution during CO_2 injection have been tested in Berea cores above and below miscibility pressure. However, the level of heterogeneity rarely, if ever, includes the presence of natural fractures. This is not coincidental since the level of experimentation required is high in order to develop useful interpretations. The fact remains, however, that reservoir heterogeneity dominates the performance of gas injection. Hydraulic or natural fractures can exert a major influence on the economics of CO_2 injection projects. However, the fundamental mechanisms of transfer in fracture systems are virtually unexplored. The transfer of injected gas from HF or NF determines the ultimate displacement and sweep efficiency. It is the intent of this proposed work to advance the understanding of this dynamic process and determine the implications on the ultimate performance of bypassing reserves during CO_2 injection.

Work to be performed:

Task 1.0 Experimental Investigation of Transfer Mechanisms during CO_2 Flooding in NFR and HFR.

1. Laboratory results to demonstrate the effect of overburden pressure (stress-state) on fracture aperture distribution and also permeability of the rock (level of heterogeneity).
2. Effect of fracture aperture distribution on viscous and capillary forces.
3. Laboratory results to demonstrate the effect of hydraulic fracture on sweep efficiency and fracture-matrix interactions.

Task 2.0 Experimental Investigation of Bypassing Mechanisms during CO_2 Flooding in HFR and NFR.

1. Laboratory results showing optimum WAG injection ratio that maximizes the sweep efficiency.
2. Laboratory results showing optimum injection rate that mitigates bypassing oil reserve during CO_2 injection in HFR and NFR.
3. Possible strategies to mitigate bypassing mechanisms that will result in less bypassing and more efficient CO_2 flooding in fracture-dominated reservoirs.

Task 3.0 Imaging Experiments Using X-ray CT.

1. Imaging the saturation profile of non-fractured and fractured cores for investigating bypassing mechanisms and modeling purpose

Task 4.0 Analysis and Modeling Transfer and Bypassing Mechanisms.

1. Development of mathematical model and/or numerical modeling to examine the physical mechanisms of bypassing that occur in hydraulically and naturally fractured reservoirs, both above and below the MMP.
2. Identifying important parameters affecting bypassing mechanisms.
3. Providing more confident scaling of field performance from laboratory experiments.

ACCOMPLISMENTS:

Task 1.0 Literature Review

Task 2.0 Experimental Investigation of Transfer Mechanisms during CO_2 Flooding in NFR and HFR.

1. Laboratory results to demonstrate the effect of overburden pressure (stress-state) on unfractured and fractured cores. Quantification of flow path contributors (matrix or fracture) and determination of fracture aperture (width) and matrix and fracture permeability under variable overburden pressures and injection rates.
2. Laboratory results to demonstrate the effect of overburden pressure (stress-state) on unfractured and fractured cores in multiphase flow. The preliminary results of static imbibition experiments are presented as a precursor to image the saturation profiles of non-fractured and fractured cores using X-Ray CT scanner.

3. Establish the fracture aperture calibration.
4. Laboratory results to demonstrate the effect of overburden pressure (stress-state) on fracture aperture distribution and also permeability of the rock (level of heterogeneity).
5. Development dual porosity simulator using empirical transfer function.

Task 3.0 Imaging Experiments Using X-ray CT.
1. Imaging the saturation profile of non-fractured and fractured cores at spontaneous experiments for investigating fluid intake (capillary force) and for modeling spontaneous imbibition.
2. Imaging the movement of brine in oil saturated core.
3. Imaging the movement of brine in a fractured core horizontally and vertically for verifying the use of parallel plate model.
4. Imaging the fractured core for establishing fracture aperture calibration.
5. Imaging the fractured cores for examining fracture aperture distribution under different overburden pressure.

Task 5.0 Analysis and Modeling Transfer and Bypassing Mechanisms.
1. Modeling the laboratory experiment to investigate of the effect of fracture aperture at variable overburden pressures.
2. Modeling fluid flow through a single fracture using experimental, stochastic and simulation approaches to investigate the effect of different rock heterogeneity on flow path contributors.
3. Validation of cubic law equation.
4. Modeling study to investigate the effect of different rock heterogeneity on flow path contributors.
5. Modeling study to investigate the transfer mechanism during core flooding in fractured core.

PROJECT STATUS
Current Work:
Task 2.0 Experimental Investigation of Bypassing Mechanisms during CO_2 Flooding in HFR and NFR.
1. Perform laboratory experiments to demonstrate the movement of CO_2 in a fractured core.

Task 3.0 Imaging Experiments Using X-ray CT.
1. Image the CO_2 movement in oil saturated core

Task 5.0 Analysis and Modeling Transfer and Bypassing Mechanisms.
1. Modeling the water imbibition and gas drainage using a commercial simulator compared with our simulator.

SCHEDULED MILESTONES:

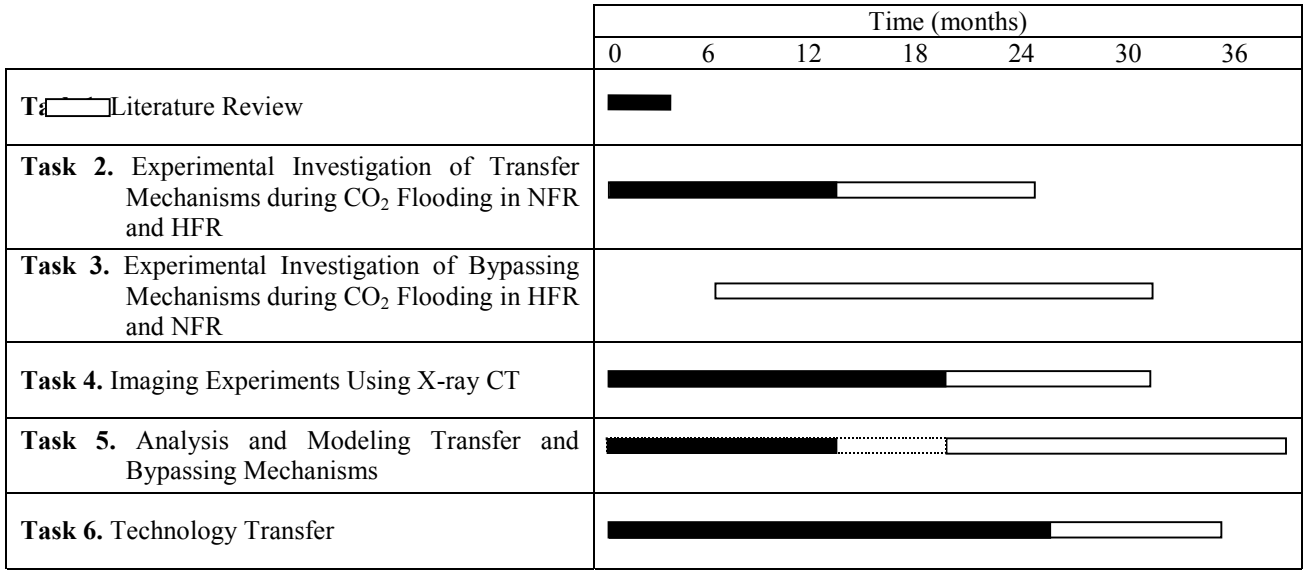

Accomplished Milestones
Proposed Milestones

REPORTS:

Putra, E., Schechter, D.S., and Vivek, M.: "Effect of Overburden Pressure on Unfractured and Fractured Permeability Cores," report included in "Investigation of Efficiency Improvement During CO2 Injection in Hydraulically and Naturally Fractured Reservoirs" First Semi-Annual Progress Report (DOE Contract No.: DE-FC26-01BC15361), Oct 2001-March 2002.

Alfred, D., Muralidharan, V., Putra, E., and Schechter, D.S.: "Modeling Fluid Flow Through Single Fracture Using Experimental, Stochastic and Simulation Approaches," report included in "Investigation of Efficiency Improvement During CO2 Injection in Hydraulically and Naturally Fractured Reservoirs" Second Semi-Annual Progress Report (DOE Contract No.: DE-FC26-01BC15361), April 2002-October 2002.

Muralidharan, V., Putra, E., and Schechter, D.S.: "Investigating the Changes in Matrix and Fracture Properties and Fluid Flow under Different Stress-state Conditions," report included in "Investigation of Efficiency Improvement During CO2 Injection in Hydraulically and Naturally Fractured Reservoirs" Second Semi-Annual Progress Report (DOE Contract No.: DE-FC26-01BC15361), April 2002-October 2002.

Muralidharan, V., Kaul S., Putra, E., and Schechter, D.S.: "Preliminary Results of Imaging Imbibition Process Using X-Ray CT Scanner," report included in "Investigation of Efficiency Improvement During CO2 Injection in Hydraulically and Naturally Fractured Reservoirs" Second Semi-Annual Progress Report (DOE Contract No.: DE-FC26-01BC15361), April 2002-October 2002.

Kaul, S., Putra, E., and Schechter, D.S.: "X-Ray Tomography Results Validate Numerical Modeling of Flow in Fractures," report included in "Investigation of Efficiency Improvement During CO2 Injection in Hydraulically and Naturally Fractured Reservoirs," Third Semi-Annual Progress Report (DOE Contract No.: DE-FC26-01BC15361), October 2002-March 2002.

Tellapaneni, P.K., Putra, E., and Schechter, D.S: "Simulation of Naturally Fractured Reservoirs Using Empirically Derived Transfer Function," report included in "Investigation of Efficiency Improvement During CO2 Injection in Hydraulically and Naturally Fractured Reservoirs," Fourth Semi-Annual Progress Report (DOE Contract No.: DE-FC26-01BC15361), April 2003-October 2003.

Muralidharan, V., Chakravarthy D., Putra, E., and Schechter, D.S.: "Fracture Aperture and Fracture Distribution," report included in "Investigation of Efficiency Improvement During CO2 Injection in Hydraulically and Naturally Fractured Reservoirs" Fourth Semi-Annual Progress Report (DOE Contract No.: DE-FC26-01BC15361), April 2003-October 2003.

TECHNOLOGY TRANSFER ACTIVITIES:

Presentations

On September 18, 2003, we presented the talk "Waterflood and CO_2 performance in the Naturally Fractured Spraberry Trend Area," at the Statoil Research Summit 2003, Trondheim, Norway.

On February 8, 2003, we (Dicman Alfred) presented the talk, "Modeling Flow through Fractures using Experimental, Stochastic and Simulation Approaches," for 2003 SPE Texas A&M contest and won 2nd place in first round and 1st place in final round MS division of Texas A&M. Dicman represented Texas A&M at Regional Region at Rice University and International Region at Calgary University, Canada and won 2nd place at both regions.

On February 8, 2003, we (Sandeep P. Kaul) presented the talk, "X-Ray Tomography Results Validate Numerical Model of Flow in Fractures," for 2003 SPE Texas A&M contest and won 2nd place in first round MS division of Texas A&M.

On February 8, 2003, we (Vivek Muralidharan) presented the talk, "overburden pressure affects fracture aperture and fracture permeability in a fractured reservoir," for 2003 SPE Texas A&M contest and won 2nd place in first round MS division of Texas A&M.

On June 2003, we presented the Short Course for Saudi Aramco in Al Khobar, Saudi Arabia – "Reservoir Characterization, Engineering and Enhanced Oil Recovery in Naturally Fractured Reservoirs."

On March 2003, we presented the Short Course for UNAM/PEMEX in Mexico City, Mexico – "Reservoir Characterization and Engineering in Naturally Fractured Gas and Oil Reservoirs – Part II."

On October 2001, we presented the Short Course for UNAM/PEMEX (National Petroleum Company of Mexico) in Mexico City, Mexico – "Reservoir Characterization and Engineering in Naturally Fractured Gas and Oil Reservoirs - Part I."

On February 2001, we presented the Short Course for for UNAM/PEMEX in Mexico City, Mexico – "Reservoir Characterization and Engineering in Naturally Fractured Gas and Oil Reservoirs – Part I."

On June 13, 2002, we presented the "Imbibition and its Relevance to Waterflood Performance in the Naturally Fractured Spraberry Trend Area," at the Rice University and University of Houston invited lecture for Society of Petroleum Engineering Chapter, Duncan Hall, Rice University.

Papers and Publications

Alfred, D., Putra, E., and Schechter, D.S., Modeling Fluid Flow Through a Single Fracture Using Experimental, Stochastic and Simulation Approaches, accepted for publication, Saudi Aramco Journal of Technology, Spring, 2004.

Putra, E., Muralidharan, V., and Schechter, D.S., Overburden Pressure Affects Fracture Aperture and Fracture Permeability in a Fractured Reservoir, accepted for publication, Saudi Aramco Journal of Technology, Fall 2003.

Kaul, S.P., Putra, E., and Schechter, D.S.: "X-Ray Tomography Results Validate Numerical Modeling of Flow in Fractures," Jurnal Teknologi Mineral, 2003

Internet Postings on the Project and Software to Download

A description of our research group can be found at the following Petroleum Engineering Texas A&M Website: http://pumpjack.tamu.edu/faculty/schechter/baervan/homepage.html. The site lists the publications of our group and allows downloads of several papers, reports, and presentations.

This website also allows downloading of software, i.e. spontaneous imbibition simulator, Delaunay Triangulation, reservoir management software (in progress) and reservoir modeling simulator (in progress).

CONTRACT INFORMATION:

NAME: David Schechter
PHONE: 979/ 845-2275
FAX: 979/845-1307
E-MAIL: schech@spindletop.tamu.edu

DIGITAL PICTURES:

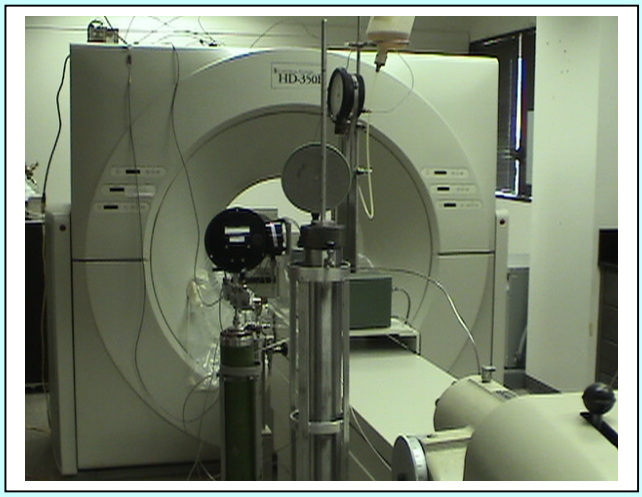

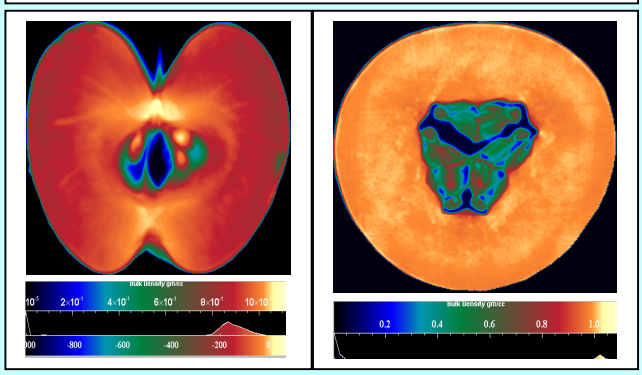

X-Ray CT Scanner Laboratory

The CT Scanner can be used to measure porosity and fluid saturations; to identify phase types and interfaces; and to determine the presence of mineral types and fractures in formation cores. The CT scanner uses the same principle as the basic x-ray. Inside the scanner is a round rotating frame which has x-ray tube mounted on one side and a curved detector on the opposite side. As the frame rotates 360 degrees around the object, a fan of x-rays go through the object to the detector on the opposite side producing a slice image on the digital computer. Measured values are stored as two-dimensional pixel images, which may be combined to create a three-dimensional image of the object scanned.

The CT Scanner uses the combination of the digital computer and rotating x-ray devices to create detailed cross sectional images. The CT Scanner was initially developed and predominantly used as a medical diagnostic tool. With the advent of high-resolution scanners and powerful imaging software has made the CT Scanner increasingly more important as a research and diagnostic tool in petroleum industry.

The HD 350 X-Ray CT Scanner (Fourth Generation) is a state-of-the-art CT scanner capable of scanning objects as large as 50 cm in diameter at scan speeds of 2 seconds per revolution. Acquired in October 2002, the scanner has a cross-sectional resolution of 0.3 mm by 0.3 mm and a fully programmable sample positioning table with a travel precision of 0.03 mm.
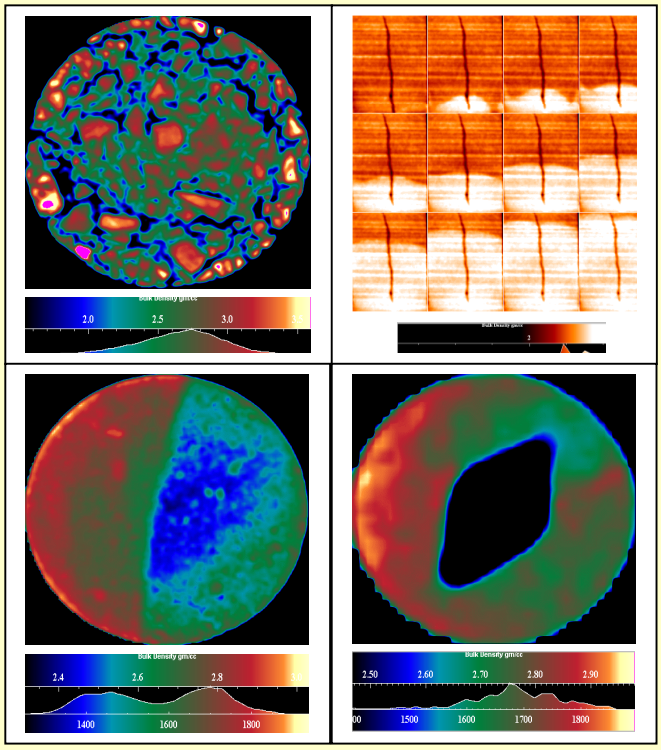
To date, the CT Scanner has been used in research projects supported by the U.S Department of Energy for identification fractures and vugs in formation cores, measurement of fracture apertures under different overburden pressure and fluid saturation in fractured cores during waterflood experiments. The CT scanner also is an invaluable research tool for research in other disciplines whenever high-resolution noninvasive diagnostics and measurements are required.